The Dissertation Committee for Huseyin Onur Balan Certifies that this is the approved version of the following dissertation:

Dynamics of Foam Mobility in Porous Media

Committee:

Quoc P. Nguyen, Supervisor

Matthew T. Balhoff, Co-Supervisor

Roger T. Bonnecaze

Steven L. Bryant

Chun Huh

Dynamics of Foam Mobility in Porous Media

by

Huseyin Onur Balan, B.S.; M.S.

Dissertation

Presented to the Faculty of the Graduate School of

The University of Texas at Austin

in Partial Fulfillment

of the Requirements

for the Degree of

Doctor of Philosophy

The University of Texas at Austin

May 2013

Dedication

To my beloved wife Selin; for her everlasting love and never-ending support. She is the reason of my peaceful and happy life.

To my mother Sule, my father Memduh Sener and my sister Hulya Belcim; for their valuable love and support.

To Mustafa Kemal Ataturk, the founder of the modern Republic of Turkey; for inspiring me with his quote “Our true mentor in life is science”.

Acknowledgements

I would like to express my deepest gratitude to my supervisor Dr. Quoc Nguyen for his never-ending support, patience, encouragement and guidance throughout my Ph.D. education. I have learnt a lot from his vast expertise in the area of foam flooding, his unique way of solving challenging reservoir engineering problems and the exciting scientific discussions that we have made. I feel very fortunate to be a member of his research group during my five years at UT-Austin. I also would like to show my sincere gratitude to my co-supervisor Dr. Matthew Balhoff for his never-ending support and guidance throughout this study. I am so glad that he introduced me the area of pore-network modeling, which fundamentally changed my way of understanding the complex fluid flow through porous media.

I would like to acknowledge my committee members Dr. Roger Bonnecaze, Dr. Steven Bryant, and Dr. Chun Huh for their valuable comments and suggestions. I am also thankful to Dr. Bryant for teaching me transport phenomena and pore-level petrophysics courses which were extremely helpful for me to deeply understand pore-network modeling.

I would like to acknowledge Dr. William Rossen from Delft University of Technology for his valuable comments and suggestions. I would also like to acknowledge my dear friend Dr. Guangwei Ren for providing me his experimental data for history matching purposes.

I would like to thank my dear friends Dr. Cigdem Metin, Naveed Arsalan, Nhut Nguyen, Oscar Llama, Dr. Mayank Srivastava, Dr. Sujeewa Palayangoda, Dr. Cesar Mantilla, Stephen Jong, Sayantan Bhowmik, Brandon Henke and Tolga Metin for making

this journey enjoyable with their friendship. I would also like to thank Frankie Hart for her excellent guidance and Roger Terzian for his superb technical assistance.

I am truly indebted and thankful to my family; my mother Sule, my father Memduh Sener, my sister Hulya Belcim, and my beloved wife Selin. Without their love and support, I would not increase my mental strength to complete this study. I would like to express my special thanks to my lovely wife Selin for her everlasting love and never-ending support. We started this journey together and passed all difficult life experiences by supporting each other. I feel fortunate to be the husband of such a wonderful woman.

Dynamics of Foam Mobility in Porous Media

Huseyin Onur Balan, Ph.D.

The University of Texas at Austin, 2013

Supervisor: Quoc P. Nguyen

Co-Supervisor: Matthew T. Balhoff

Foam reduces gas mobility in porous media by trapping substantial amount of gas and applying a viscous resistance of flowing lamellas to gas flow. In mechanistic foam modeling, gas relative permeability is significantly modified by gas trapping, while an effective gas viscosity, which is a function of flowing lamella density, is assigned to flowing gas. A complete understanding of foam mobility in porous media requires being able to predict the effects of pressure gradient, foam texture, rock and fluid properties on gas trapping, and therefore gas relative permeability, and effective gas viscosity. In the foam literature, separating the contributions of gas trapping and effective gas viscosity on foam mobility has not been achieved because the dynamics of gas trapping and its effects on the effective gas viscosity have been neglected.

In this study, dynamics of foam mobility in porous media is investigated with a special focus on gas trapping and its effects on gas relative permeability and effective gas viscosity. Three-dimensional pore-network models representative of real porous media coupled with fluid models characterizing a lamella flow through a pore throat are used to predict flow paths, threshold pressure gradient and Darcy velocity of foam. It is found that the threshold path and the pore volume open above the threshold pressure are independent of the fluid model used in this study. Furthermore, analytical correlations of

flowing gas fraction as functions of pressure gradient, lamella density, rock and fluid properties are obtained. At a constant pressure gradient, flowing gas fraction increases as overall lamella density decreases. In the discontinuous-gas foam flow regime, there exists a threshold pressure gradient, which increases with overall lamella density. One of the important findings of this study is that gas relative permeability is a strong non-linear function of flowing gas fraction, opposing most of the existing theoretical models. However, the shape of the relative gas permeability curve is poorly sensitive to overall lamella density. Flowing and trapped lamella densities change with pressure gradient. Moreover, analytical correlations of effective gas viscosity as functions of capillary number, lamella density and rock properties are obtained by up-scaling a commonly used pore-scale apparent gas (lamella) viscosity model. Effective gas viscosity increases nonlinearly with flowing lamella density, which opposes to the existing linear foam viscosity models. In addition, the individual contributions of gas trapping and effective gas viscosity on foam mobility are quantified for the first time. The functional relationship between effective gas viscosity and flowing lamella density in the presence of dynamic trapped gas is verified.

A mechanistic foam model is developed by using the analytical correlations of flowing gas fraction and effective gas viscosity generated from the pore-network study and a modified population balance model. The developed model is successful in simulating unsteady-state and steady state flow of foam through porous media. Moreover, the flow behaviors in high- and low-quality flow regimes are verified by the experimental studies in the literature. Finally, the simulation results are successfully history matched with two different core-flood data.

Table of Contents

List of Tables

List of Figures

Chapter 1: Introduction

1.1 OVERVIEW

Successful field applications of any enhanced oil recovery (EOR) technique require mobility control for displacing phase to maximize vertical and areal sweep efficiencies. Volumetric sweep efficiency of displacing phase can be low due to unfavorable mobility ratio and density contrast between displacing and displaced phases. Moreover, areal and vertical heterogeneity in permeability can lead to channeling during injection of the displacing phase (Turta and Singhal, 1998). These problems are more severe in miscible/immiscible gas flooding processes than in any other EOR technique because of the very high mobility of gas phase in porous media. Furthermore, low sweep efficiency in gas flooding leads to low oil recovery, high gas-to-oil ratio (GOR) and early breakthrough of injected gas at the production wells. Displacement mechanism of miscible gas processes bases on the dissolution of injected gas into oil phase, which reduces oil viscosity and swells oil. Therefore, gas-mobility control in porous media plays an important role in maximizing oil recovery by increasing the volume of oil-in-place contacted by the injected gas (Green and Willhite, 1998).

Aqueous foam flooding is an effective technique to control gas mobility in permeable porous media with successful applications to improving volumetric sweep efficiency in miscible/immiscible gas flooding and steam flooding (Schramm, 1994; Rossen, 1996; Patzek, 1996). Recently, foam has been proven to be the low-cost alternative to polymer in chemical flooding in difficult reservoir conditions such as very low permeability rocks and high temperature (Li et al., 2008; Srivastava and Nguyen, 2010; Srivastava et al., 2010). In addition to EOR applications, foam has been routinely

used to direct flow of cleaning fluids such as surfactant and acid solutions in aquifer remediation (Hirasaki et al., 2000) and well stimulation (Gdanski, 1993), respectively.

The physical principle of foam-induced fluid mobility control in the above applications is based on the resistance of aqueous foam films (or lamellas) to gas flow and the reduction of available flow area to gas and liquid phases due to gas trapping during multi-phase flow. Experimental studies show that the flowing gas fraction of foam in porous media ranges from 50% to less than 1% (Radke and Gillis, 1990; Friedmann et al., 1991; Tang and Kovscek, 2006; Nguyen et al., 2009; Kil et al., 2011). The flowing gas moves in discrete "bubble trains" through beds of trapped bubbles (Falls et al., 1989). The gas blocking in porous media results from the resistance of individual lamellas to stretching and the pressure difference across them. Lamellas move to the pore throats, if foam is at rest, due to the gas diffusion between bubbles (Rossen, 1996; Cohen et al., 1997). Resistance to the movement of a lamella is at its highest level at the pore throat as it scales with the inverse of the pore-throat radius. The capacity of foam-induced fluid blocking on a field scale in acid diversion, reduction of gas channeling, and reduced liquid injectivity in surfactant alternating gas (SAG) processes is thus strongly influenced by the level of gas trapping. Moreover, accurate prediction of flowing gas fraction under reservoir conditions plays a major role in designing mass exchange between injected gas and oil in place in miscible gas processes.

Modeling gas relative permeability with trapped foam requires the knowledge of the functional relationship between flowing gas fraction, defined as the ratio of flowing gas saturation to the overall gas saturation, and flow pressure gradient. Many foam models make no attempt to represent gas trapping or separate its effect on gas mobility from other factors (Fisher et al., 1990; Martinsen and Vassenden, 1999; Vassenden and Holt, 2000; Cheng et al., 2000; Kam et al., 2007). The population-balance models of Falls

et al. (1988, 1989), Friedmann et al. (1991), and Bertin (2000) assume a fixed flowing gas fraction. In the model of Kovscek and Radke (1994) it is a function of foam texture. More recently, Tang and Kovscek (2006) proposed a power-law model based on classical percolation theory for flowing gas fraction as a function of pressure gradient. Others (Cohen et al., 1997; Kharabaf and Yortsos, 1998) attempted to predict the trapped gas fraction under a given pressure gradient by using simple two-dimensional network models.

Gas trapping during foam flow in porous media is a dynamic process in which trapping and remobilization of lamellas separating gas is governed by the rheological behavior of flowing foam. Based on the Bretherton's model (Bretherton, 1961) for dynamic pressure drop across the front meniscus of a long bubble moving in a straight capillary tube and the Hagen-Poiseuille equation (Bird et al., 2007), Hirasaki and Lawson (1985) developed a rheological model for foam flow in smooth capillary tubes, taken into account the respective effects of lamella density and surface tension gradient due to the high surface mobility of surfactant. This model has been widely used without the latter effect in modeling of apparent foamed gas viscosity based on the concept of population balance (Falls et al., 1988, 1999; Friedmann et al., 1991; Kovscek and Radke, 1994; Kovscek et al., 1995, 1997; Bertin, 2000; Tang and Kovscek, 2006; Kam et al., 2007; Kam, 2008; Chen et al., 2010; Ashoori et al., 2011). It is important to note that the linear relationship between apparent gas viscosity and lamella density in a straight capillary tube has been assumed to be valid for foam flow in porous media in all existing foam models.

Complete understanding of foam, and fully-mechanistic foam modeling, requires being able to predict the effect of pressure gradient on gas trapping and flow, and effective gas viscosity. In a foam-flow experiment all one can measure is total mobility,

not the separate contributions of relative permeability and viscosity. Indeed, the very definition of relative permeability assumes a fixed value of phase viscosity. Still, the restriction in flow paths caused by gas trapping seems similar to the reduction in relative permeability caused by presence of another phase, which makes it appealing to split gas mobility with foam into effects of gas relative permeability and viscosity. Although there have been some attempts to predict the effect of gas trapping on gas relative permeability, there have been no comprehensive modeling studies in the literature exploring the dynamics of gas trapping and remobilization, which may enable to separate the contributions of gas trapping and effective gas viscosity on foam mobility.

1.2 RESEARCH OBJECTIVE

The main research objective of this study is to understand the dynamics of foam mobility in porous media by taking into account the two key rheological features of foam mobility, which are gas relative permeability with trapped gas and effective gas viscosity, and their influencing factors by using 3D pore-network models coupled with fluid models that represent a lamella flow through a pore throat. For this purpose, sub-objectives are given as:

- To understand the dynamics of foam trapping and remobilization mechanism and to investigate possible models for the relationships between pressure gradient and gas trapping and between gas trapping and gas mobility. Moreover, to determine whether these models are consistent with the physics of non-Newtonian flow in porous media and whether any universal relations can be developed for these properties.

- To develop a gas trapping model for predicting gas relative permeability with foam as functions of pressure gradient, lamella density, fluid and porous media properties.
- To upscale pore-level apparent gas (lamella) viscosity models to predict effective gas viscosity of flowing gas as functions of capillary number, lamella density and porous media properties.
- To separate the effects of gas relative permeability with trapped gas and effective gas viscosity on total foam mobility and to understand the dynamics between the flowing and trapped gas.
- To develop a comprehensive mechanistic foam flow model by combining the developed foam mobility model and a population balance model. This model is to be used to history match and to interpret the core flood experiments.

1.3 DISSERTATION OUTLINE

This dissertation is composed of seven chapters. In Chapter 2, the literature review of foam flow through porous media and previous modeling studies are given. In Chapter 3, network modeling of gas trapping and foam mobility in porous media is investigated by using different fluid models representing a lamella flow through a pore throat. In Chapter 4, dynamics of gas trapping and effective gas viscosity as a function of lamella density is studied. Moreover, the effects of gas trapping and effective gas viscosity on foam mobility are seperated. In Chapter 5, analytical correlations of flowing gas fraction and effective gas viscosity (which are independent of pore-network type) are developed. In Chapter 6, a mechanistic foam flow model is developed by using the results of the pore-network study. Furthermore, the simulation results are history matched with

core-flood data and discussed. Finally, in Chapter 7, the dissertation is concluded and the main findings of the research and suggested future work are presented.

Chapter 2: Literature Review

Foams are a promising means of redirecting gas flow in miscible, immiscible and steam enhanced oil recovery (EOR) (Schramm, 1994; Rossen, 1996), improving liquid mobility in low-tension gas flooding (Srivastava and Nguyen, 2010; Srivastava et al., 2010) and of directing flow of remediation fluids in aquifer remediation (Hirasaki et al., 2000). In addition, foam is used worldwide in acid diversion in matrix well-stimulation treatments (Gdanski, 1993). In these applications, the bubbles are as large as, or larger than, the individual pores. Individual soap films, or lamellae, separating bubbles stretch from one pore wall to the opposite wall. This sets these applications apart from other applications of foam in petroleum operations, such as drilling, cementing, fracturing and unloading water from gas wells: in those applications the bubbles are much smaller than the flow channel, and foam can be treated as a complex, but homogeneous, fluid.

2.1 Foam Flow Through Porous Media

Aqueous foam is a dispersion of gas phase within a continuous aqueous phase, which is stabilized by surfactant molecules at the gas-liquid interface. In porous media, gas bubbles are separated by liquid-filled films called lamellae. Each individual lamella has a certain capillary resistance to gas flow. Foam reduces gas mobility greatly, both by trapping a large fraction of the gas in place and by increasing the resistance to flow of the gas that does flow (Falls et al., 1988, 1989; Rossen and Wang, 1999). Gas trapping is the key to effective acid diversion and aquifer remediation and to liquid injection in SAG foam applications (Persoff et al., 1990; Zhou and Rossen, 1994). It plays a major role in reducing gas mobility in EOR. Measured values of flowing gas fraction of foam in porous media range from about 50% to less than 1% (Radke and Gillis, 1990; Friedmann et al., 1991; Tang and Kovscek, 2006; Nguyen et al., 2009; Kil et al., 2011). The gas that

does flow moves in discrete "bubble trains" through beds of trapped bubbles (Falls et al., 1989) (Figure 2.1). The blocking of most of the pathways to gas flow obviously has a large impact on gas mobility

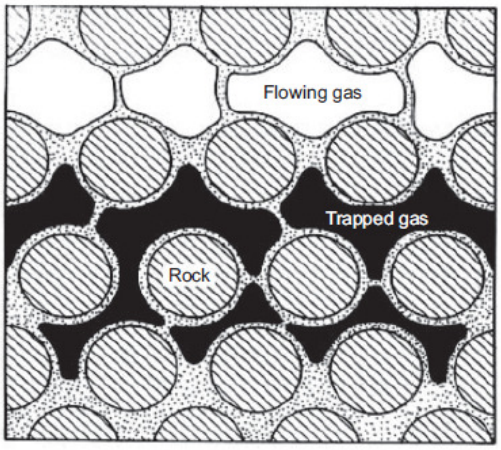

Figure 2.1 Schematic of foam flow in porous media (Kovscek and Radke, 1994).

The flow of foam through porous media is much different than two-phase flow of gas and water. In the latter one, mobility of each phase strongly depends on its own saturation. In the former one, however, foamed gas is a discontinuous phase and its mobility strongly depends on foam texture, which is the number of lamellas per unit gas volume (Holm, 1968; Falls et al., 1988). The finer the foam texture, the higher the flow resistance to gas flow (Ettinger and Radke, 1992). Aqueous phase in foam, however, flows through its continuous liquid network. Therefore, the relationship between the water relative permeability and water saturation is not affected by the presence of foam in porous media (Bernard et al., 1965; Huh and Handy, 1989). However, the high amount of trapped gas developed during foam flow decreases the aqueous phase mobility by blocking the available area to flow (Bernard et al., 1965).

Many experimental studies (Bernard and Holm, 1964; Lee and Heller, 1990; Lee et al., 1991) showed that foam reduces the gas mobility more in high permeability cores than that in low permeability cores. This leads to a cross-flow of gas from high- to low-permeability layers if the layers are in capillary equilibrium. Therefore, foam front moves through each layer at the same rate. If there is a no capillary equilibrium between layers, however, foam plugs the high-perm layer and diverts flow to low-perm layer (Bertin and Apaydin, 1999). Therefore, foam is relatively stronger in high-perm layers than that in low-perm layer, which is the driving mechanism for cross flow (Tanzil et al., 2002).

2.2 FOAM TEXTURE IN POROUS MEDIA

Lamella density in porous media, which is also called foam texture, is the most important parameter controlling the gas mobility in porous media (Falls et al. 1989). The foam texture is controlled by the two opposing mechanisms occurring in porous media: lamella generation and lamella coalescence.

2.2.1 Lamella Generation

Micromodel studies (Mast, 1972; Owete and Brigham, 1987; Ransohoff and Radke, 1988) identify that there are three different mechanisms of lamella generation in porous media: capillary snap-off, leave-behind, and lamella division.

2.2.1.1 Capillary Snap-off

Capillary snap-off was originally studied by Roof (1970) to explain the trapping mechanism of oil droplets in water-wet pores. Snap-off is a mechanical process which does not require the presence of surfactant. The same mechanism is also responsible for bubble generation when the gaseous phase invades into water-wet pores (Mast, 1972). Capillary pressure in a pore throat is higher than that in a pore, since the radius of curvature between gaseous and aqueous phases is smaller in a pore throat. If it is assumed

that the pressure gradient of gaseous phase is negligible during its invasion, then the aqueous phase pressure in a pore must be higher than that in a pore throat (Falls et al., 1988). Therefore, aqueous phase accumulates at pore throats by flowing from pores to pore-throats, which forms liquid films (lamellas) separating gas bubbles (Figure 2.2). Many investigators (Mast, 1972; Owete and Brigham, 1987; Ransohoff and Radke, 1988) reported that the capillary snap-off is the dominant mechanism for strong foam formation, since the generated lamellas resist to gas flow by being mainly perpendicular to the flow direction. Snap-off mechanism depends on the pore geometry, fluid properties, capillary and viscous forces (Ransohoff and Radke, 1988).

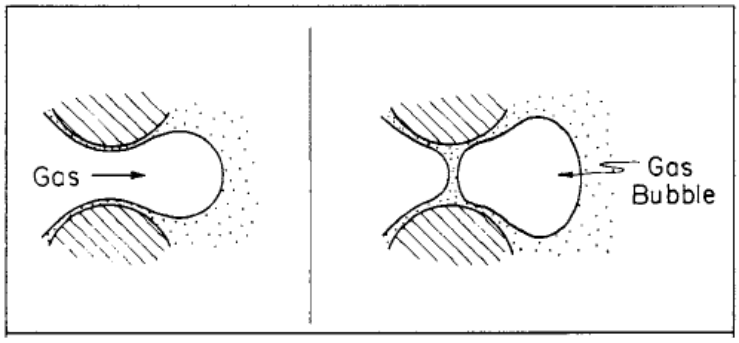

Figure 2.2 Schematic of capillary snap-off mechanism (Ransohoff and Radke, 1988).

2.2.1.2 Leave-Behind

In the leave-behind mechanism gaseous phase invades into two adjacent pores and a lamella forms between these pores (Figure 2.3) being generally parallel to the flow direction. These lamellas do not contribute to the reduction in gas mobility (Ransohoff and Radke, 1988).

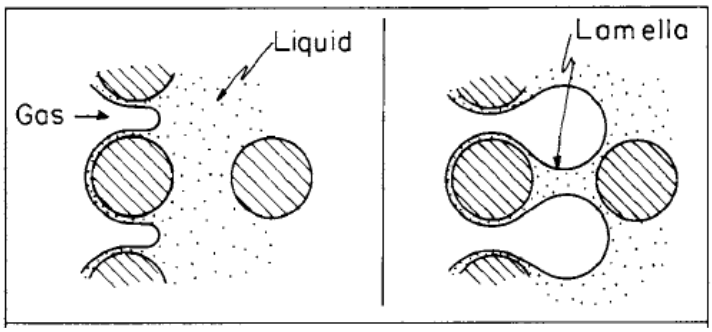

Figure 2.3 Schematic of the leave-behind mechanism (Ransohoff and Radke, 1988).

2.2.1.3 Lamella-Division

Lamella-division is a secondary lamella generation mechanism, since it requires a moving lamella, which was generated before by either snap-off or leave-behind mechanisms. When the moving lamella approaches a branch point, the lamella divides into two or more pore channels (Figure 2.4). The lamellas generated by this mechanism reduce the gas mobility, since they are perpendicular to flow direction like the lamellas generated by snap-off (Ransohoff and Radke, 1988).

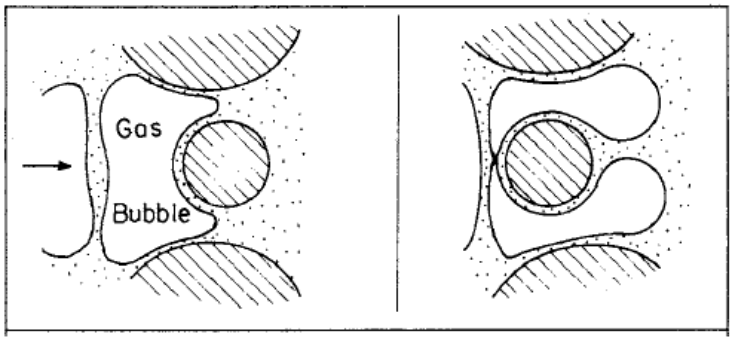

Figure 2.4 Schematic of lamella-division mechanism (Ransohoff and Radke, 1988).

2.2.2 Lamella Stability and Coalescence

The stability of foam in porous media is governed by the stability of individual foam lamellas, which depends on many factors such as capillary pressure, surfactant

concentration and adsorption, gas diffusion through a lamella, presence of oil phase, salt concentration, surface forces and mechanical fluctuations (Aronson et al., 1994).

There are three distinct forces acting on a foam lamella: repulsive positive electrostatic forces (Π_{EL}), attractive negative Van Der Waals forces (Π_{VW}) and capillary forces between gas and liquid phases (Exerowa and Kruglyakov, 1998). Surfactant molecules absorbed at gas-liquid interfaces create charged surfaces repulsing each other and stabilize lamella. Surfactant molecules consist of a polar portion called “head”, and a nonpolar portion called “tail”. In a common black film surfactant molecules accumulate at gas-liquid interfaces, since the head (polar) and tail (nonpolar) portions are attracted by water and gas molecules, respectively (Figure 2.5) (Green and Willhite, 1998). An increase in surfactant concentration in aqueous phase increases the stability of foam lamellas, therefore gas mobility decreases and gas trapping increases (Bernard and Holm, 1964; Bernard et al., 1965; Marsden and Khan, 1966; Lee and Heller, 1990; Lee et al., 1991; Simjoo et al., 2012). Moreover, repulsive forces increase with salt concentration in liquid phase, since surfactant concentration at gas-liquid interface increases with salt concentration (Nilsson, 1957).

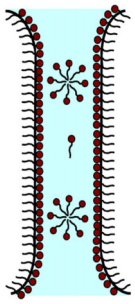

Figure 2.5 Schematic of a common black film. Surfactant molecules accumulate at gas-liquid interfaces (Farajzadeh et al., 2008).

Attractive Van der Waals forces make the charged surfaces closer and destabilize lamella. The criteria for lamella stability is that the difference between repulsive and attractive forces, which is called as disjoining pressure (Π) in DLVO theory (Derjaguin and Landau, 1941; Verwey and Overbeek, 1948), must be positive to balance capillary forces (P_c) (Eq. 2.1). Disjoining pressure strongly depends on the film thickness (h), which decreases with increasing capillary pressure. Figure 2.6 shows the relationship between disjoining pressure and film thickness for stable films, metastable films and unstable films.

$$\Pi(h) = P_c = \Pi_{EL} - \Pi_{VW} \tag{2.1}$$

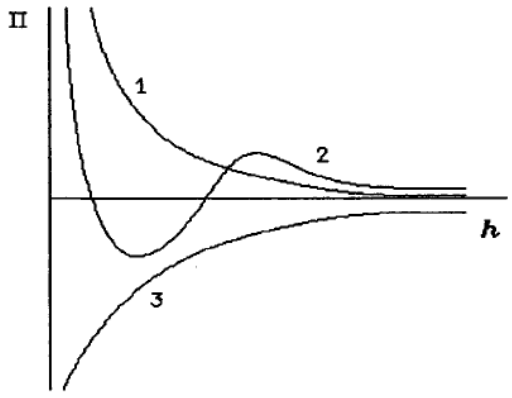

Figure 2.6 A schematic showing the relationship between disjoining pressure, Π and film thickness, h for (1) stable films; (2) metastable films; (3) unstable films (Kornev et al., 1999).

As the fraction of gas in foam (f_g) increases at a fixed gas velocity, capillary pressure increases and approaches a critical capillary pressure (P_c^*) (Figure 2.7). A further increase in the fraction of gas does not increase capillary pressure, however foam texture coarsens and capillary pressure drops (Khatib et al., 1988). Water saturation at P_c^*, which is called critical water saturation (S_w^*), remains constant. Therefore, the foam

mobility at P_c^* depends on the ratio of gas/liquid fractional flow and the liquid mobility at P_c^*. Based on this observation and the fractional flow theory, some investigators (Zhou and Rossen, 1994, 1995; Rossen and Zhou, 1995) attempted to model foam mobility in porous media at P_c^*. An increase in surfactant concentration makes foam lamellas more stable, which leads to higher P_c^*. Surfactant type and electrolyte concentration in liquid phase also controls the magnitude of P_c^* (Khatib et al, 1988).

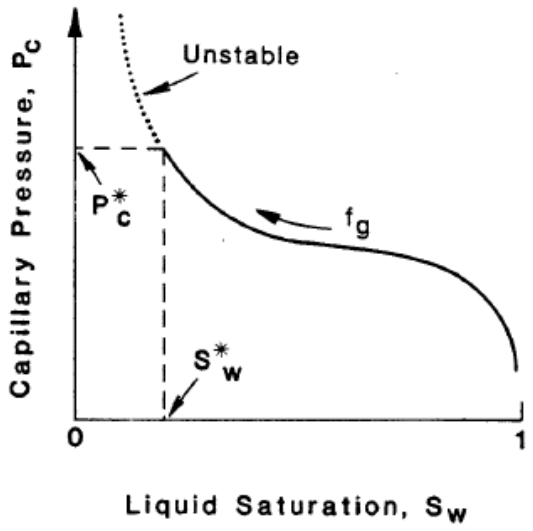

Figure 2.7 A capillary pressure curve during the displacement of aqueous phase by gas phase (Khatib et al., 1988).

The presence of light oil in porous media has a detrimental effect on foam lamella stability (Andrianov et al., 2011) and it decreases the effectiveness of foam for reducing gas and water mobility in porous media (Bernard and Holm, 1964; Bernard et al., 1965; Holm, 1968). When foam lamella contacts with oil, oil droplets enter into lamella and spreads on the gas-liquid interface. Therefore, gas-liquid interface becomes a gas-liquid-oil interface, which changes interfacial forces and makes lamella unstable (Kuhlman, 1990; Maniowe and Radke, 1990; Sanchez and Hazlett, 1992; Schramm et al., 1993).

Moreover, foam lamella generation requires a water-wet porous medium. Foam formation in oil-wet formations requires a surfactant which can change wettability from oil-wet to water-wet (Sanchez and Hazlett, 1992).

2.3 STEADY STATE FOAM FLOW THROUGH POROUS MEDIA

Steady-state flow of foam through porous media can exist either in high-quality or low-quality flow regimes (Osterloh and Jante, 1992). Foam quality is defined as the fraction of gas in the foam. In the low-quality flow regime, steady-state pressure gradient is dependent on gas velocity, but is independent of liquid velocity (Figure 2.8). Capillary resistance and gas trapping are the main mechanisms controlling the flow behavior in this regime. Furthermore, foam texture does not change much and shear-thinning behavior is observed in the low-quality regime (Alvarez et al., 2001).

In the high-quality regime, however, steady-state pressure gradient is dependent on liquid velocity, but is independent of gas velocity (Figure 2.8). At high foam qualities, capillary pressure and coalescence are the dominant mechanisms defining the foam behavior (Osterloh and Jante, 1992; Alvarez et al., 2001). Moreover, there exists a transition zone between high-quality and low-quality foam-flow regimes, which depends on critical capillary pressure at a specific permeability, gas velocity, surfactant formulation and concentration (Alvarez et al. 2001). Bubble size in high-quality foam regime is larger than that in low-quality foam regime (Holm, 1968; Alvarez et al., 2001).

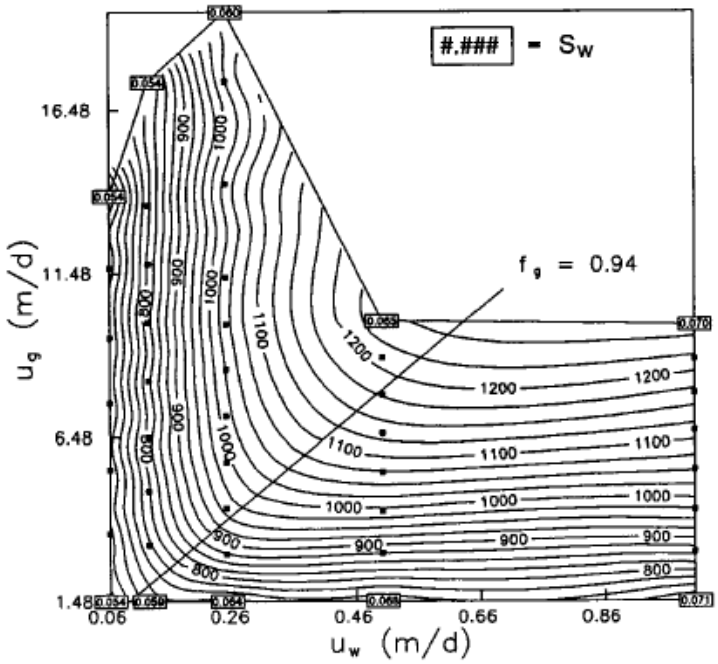

Figure 2.8 Steady-state pressure drops in a sand pack as a function of superficial phase velocities (Osterloh and Jante, 1992).

2.4 MECHANISTIC MODELING OF FOAM MOBILITY IN POROUS MEDIA

The origin of gas blocking is the resistance of individual lamellae to stretching, and the pressure difference across a curved lamella. If foam is at rest, inter-bubble diffusion (Rossen, 1996; Cohen et al., 1997) rapidly allows lamellae to move to pore throats, where resistance to movement out of the throat is greatest. One might argue that lamellae at any moment are as likely to be convex forward as backwards, but in fact most lamellae in a train are convex forward and resisting forward movement (Falls et al., 1989; Rossen, 1990a, 1990b, 1990c, 1990d; Xu and Rossen, 2003; Cox et al., 2004). There is thus a net resistance of the train to forward movement, a minimum pressure gradient, for flow of a train of bubbles of a particular size, even in the limit of zero velocity. This resistance scales with the inverse of pore-throat radius. It is difficult to fix bubble size in a flow experiment (Falls et al., 1989) and therefore one may miss this minimum pressure

gradient in experiments where bubble size changes (Rossen and Zhou, 1995). The drag on moving lamellae imparts an additional shear-thinning contribution to the effective viscosity of the gas, with a power-law exponent of (2/3) for bubbles in smooth tubes (Hirasaki and Lawson, 1985) but exponents much smaller in constricted tubes (Xu and Rossen, 2003).

2.4.1 The Population-Balance Framework

The population balance is a framework for understanding foam properties in porous media and has been the basis for most mechanistic studies of foam since the approach was introduced in the 1980s (Falls et al., 1988, 1989; Friedmann et al., 1991; Kovscek and Radke, 1994; Kovscek et al., 1995; Bertin, 2000; Tang and Kovscek, 2006; Kam et al., 2007; Kam, 2008; Chen et al., 2010; Ashoori et al., 2011). This approach splits the issue of gas mobility into two parts: the dynamic processes that create and destroy the lamellae that separate bubbles, and the mobility of foam at fixed bubble size. Lamella population balance in porous media can be formulated as:

$$\frac{\partial}{\partial t}\left[\phi\left(S_{fg}n_{fg}^{L}+S_{tg}n_{tg}^{L}\right)\right]+\frac{\partial}{\partial x}\left(u_{g}^{f}n_{fg}^{L}\right)=G_{L}+Q_{L} \tag{2.2}$$

where φ is porosity, S_{fg} is flowing gas saturation, S_{tg} is trapped gas saturation, $n_{\mathrm{fg}}{}^{\mathrm{L}}$ is number of flowing lamellae per unit volume of flowing gas, $n_{\mathrm{tg}}{}^{\mathrm{L}}$ is number of trapped lamellae per unit volume of trapped gas, $u_{\mathrm{g}}{}^{\mathrm{f}}$ is Darcy velocity of gas with foam, G_{L} is net lamella generation term, and Q_{L} is lamella source/sink term. The net lamella generation term is composed of lamella generation and coalescence terms (Kovscek et al., 1995, 1997; Kovscek and Bertin, 2003):

$$G_L = \phi S_g \left(R_g - R_c \right) \tag{2.3a}$$

$$S_g = S_{fg} + S_{tg} \tag{2.3b}$$

Where S_g is gas saturation, R_g is lamella generation rate per unit gas volume, and R_c is lamella coalescence rate per unit gas volume. Based on snap-off mechanism, R_g is provided below (Kovscek et al., 1994a, 1994b, 1995, 1997; Kovscek and Bertin, 2003):

$$R_g = c_1 v_w \left(v_g^f \right)^{1/3} \tag{2.4a}$$

$$v_g^f = \frac{u_g^f}{c_A \phi S_{fg}} \tag{2.4b}$$

Where c_1 is rate constant for lamella generation, v_w interstitial water velocity, v_g^f interstitial gas velocity with foam, and c_A is cross sectional area. Kam and Rossen (2003), Kam et al. (2007) and Kam (2008) also proposed a different lamella generation rate equation based on lamella division mechanism.

As the lamella generation occurs in porous media, the potential lamella germination sites for snap-off are occupied (Kovscek and Radke, 1996; Ransohoff et al., 1987), which decreases the rate constant for lamella generation, c_1. Chen et al. (2010) proposed the following equation to represent this relationship between c_1 and n_{fg}^L:

$$c_1 = c_1^o \left[1 - \left(\frac{n_{fg}^L}{n_{fg}^{L*}} \right)^w \right] \tag{2.5}$$

Where c_1^o is reference rate constant for lamella generation, w is a constant, and n_{fg}^{L*} is the maximum number of flowing lamellae per unit volume of flowing gas, which is equivalent to one lamella per pore throat.

Lamella coalescence rate (R_c) is directly related to capillary suction mechanism. Kovscek et al. (1993, 1994a, 1994b, 1995, 1997) and Kovscek and Bertin (2003) provided the following equations for R_c:

$$R_c = c_{-1} v_g^f n_{fg}^L \tag{2.6a}$$

$$c_{-1}(P_c) = c_{-1}^o \left(\frac{P_c}{P_c^* - P_c} \right)^2 \tag{2.6b}$$

Where c_{-1} is rate constant for lamella coalescence, c_{-1}^o is reference rate constant for lamella coalescence, P_c is capillary pressure, and P_c^* is critical capillary pressure.

Experimental studies (Ettinger and Radke, 1992; Chen et al., 2010) show that lamella generation and coalescence rates are in balance during foam flow through porous media and the steady-state flow of foam is reached rapidly after lamella generation and mobilization in porous media. Therefore, full version of the population balance model in Eq. 2.2 is approximated by equating the lamella generation rate to coalescence rate in Eq. 2.7a (Chen et al., 2010; Kovscek and Bertin, 2003). This approximation enables one to calculate the number of flowing lamellae per unit volume of flowing gas (n_{fg}^L) at local equilibrium (Eq 2.7b).

$$R_g = R_c \tag{2.7a}$$

$$\left(n_{fg}^L \right)^{eq} = \left(\frac{c_1}{c_{-1}^o} \right) \left(\frac{P_c^* - P_c}{P_c} \right)^2 \left(\frac{v_w}{\left(v_g^f \right)^{2/3}} \right) \tag{2.7b}$$

2.4.2 Foam Mobility at Fixed Bubble (Lamella) Density

In mechanistic modeling of foam in porous media, reduced gas mobility is attributed to viscous resistance of flowing foam lamellas to gas flow, while gas trapping significantly modifies relative permeability. Although foam is composed of lamellas

separating gas bubbles, foamed gas mobility in porous media can be expressed as if it is a continuous fluid:

$$\lambda_g^f = \frac{k \cdot k_{rg}^f}{\mu_g^f} \tag{2.8}$$

where k is absolute permeability of rock, k_{rg}^{f} is gas relative permeability with foam, μ_g^{f} is effective gas viscosity, and λ_g^{f} is foamed gas mobility. Therefore, foamed gas mobility is composed of the contributions of effective gas viscosity and gas relative permeability with foam.

When comparing models for gas mobility at fixed bubble size to experimental studies, it is important to realize that bubble size changes as a function of flow rates in most experimental studies. The only study of which we are aware where bubble size has been fixed and controlled is that of Falls et al. (1989), and that study showed unambiguously a minimum pressure gradient for flow at fixed bubble size (Rossen, 1990c). The variability of bubble size in other experiments complicates the inference of an effective yield stress for foam. This is especially true in the "high-quality" or "coalescence" foam regime (Alvarez et al., 2001), where changing bubble size can give an apparent Newtonian rheology (Rossen and Zhou, 1995).

2.4.2.1 Effective Gas Viscosity

Hirasaki and Lawson (1985) studied the motion of foam lamellas through smooth capillaries and measured the pore-scale apparent gas (lamella) viscosity. Moreover, they proposed a lamella flow model through capillary tubes by extending the theory described by Bretherton (1961). There are three major contributions to gas flow resistance: slugs of liquid between bubbles, deformation of interface of a bubble passing through a capillary, and surface tension gradient (Hirasaki and Lawson, 1985). The apparent gas viscosity

was found to be proportional to (-1/3) power of interstitial gas velocity suggesting a shear thinning behavior of lamella flow in a straight capillary tube. Moreover, apparent gas viscosity increases with lamella density per unit length (Hirasaki and Lawson, 1985). Falls et al. (1989) extended the work of Hirasaki and Lawson (1985) by adding the effect of pore constrictions into apparent gas viscosity.

Effective gas viscosity is a continuum-scale representation of pore-level apparent gas viscosity. Kovscek and Radke (1994) proposed the following equation for the effective gas viscosity:

$$\mu_g^f = \mu_g + \frac{\alpha \cdot n_{fg}^L}{\left(v_g^f\right)^{1/3}} \tag{2.9}$$

where n_{fg}^{L} is number of flowing lamella per unit volume of flowing gas, v_g^f is interstitial gas velocity with foam, μ_g^f is effective gas viscosity, μ_g is gas viscosity, and α is the parameter depending on surfactant type and concentration, absolute permeability and capillary pressure in porous media (Kovscek and Bertin, 2003).

2.4.2.2 The Effect of Gas Trapping on Gas Relative Permeability

Many foam simulation models make no attempt to represent gas trapping or separate its effect on gas mobility from other factors (Fisher et al., 1990; Martinsen and Vassenden, 1999; Vassenden and Holt, 2000; Cheng et al., 2000; Kam et al., 2007). Cheng et al. (2002) represented the effects of gas trapping with a residual-gas saturation that depends on pressure gradient, without quantifying the fraction of gas that flows. Rossen (1992) illustrated using a simple bundle-of-tubes model the essence of the effect of pressure gradient (∇P) on gas mobility: gas flowing fraction increases with ∇P, while the flowing gas flows more easily in the paths already opened.

The population-balance models of Falls et al. (1988, 1989), Friedmann et al. (1991), and Bertin (2000) assumed a fixed flowing gas fraction (X_{fg}). In the model of Kovscek and Radke (1994) it is a function of foam texture. The models differ substantially in how gas relative permeability depends on X_{fg}. All of them fit the form

$$k_{rg}^{f} = k_{rg}^{*}(S_w)(X_{fg})^{A} \tag{2.10}$$

where k_{rg}^{f} is gas relative permeability with foam, k_{rg}^{*} is gas relative permeability without foam, which (in the absence of oil) depends only on water saturation, and A is an exponent. Falls et al. (1988, 1989), Friedmann et al. (1991) and Bertin (2000) chose A = 1. Kovscek and Radke (1994) chose A = 3.

It remains to relate the flowing-gas fraction (X_{fg}) to macroscopic pressure gradient (∇P). By analogy to critical phenomena and percolation theory, it is appealing to fit the flowing fraction to a scaling law of the form

$$X_{fg} \sim (\nabla P - \nabla P_M)^{B} \tag{2.11}$$

Tang and Kovscek (2006) proposed a comprehensive model for flowing gas fraction and gas mobility as a function of pressure gradient based on an analogy to percolation theory (Kovscek and Bertin, 2003). There is no minimum pressure gradient to initiate foam flow in this model (∇P_M = 0). Flowing fraction is assumed to vary with pressure gradient to the 0.4 power (B = 0.4), by analogy to the dependence of the percolation (connected) fraction on open fraction in percolation theory (Sahimi, 1993). Gas relative permeability is the foam-free value, a function of total gas saturation, multiplied by the 3rd power of flowing fraction (A = 3 in Eq. 2.10). Gas effective viscosity is a function that varies with the 0.67 power of interstitial gas velocity, in agreement with Hirasaki and Lawson (1985) formula for bubbles in smooth tubes.

Cohen et al. (1997) predicted the trapped gas fraction under a given pressure gradient and a pore-size distribution by using the Young-Laplace relationship in a simple two-dimensional network model. Kharabaf and Yortsos (1998) developed a simple pore-network model for transient and steady-state foam flow in porous media and showed the plot of flowing gas fraction as a function of normalized pressure gradient. In their model, foam behaves like fluids with a yield stress. They found that the threshold pressure gradient required to initiate foam flow depends on the throat-size distribution.

2.5 PREVIOUS MODELS FOR YIELD-STRESS FLOW IN POROUS MEDIA

The threshold gradient required to induce flow of foam is analogous to flow in porous media of non-Newtonian fluids with a yield stress. Several authors have attempted to develop models for yield-stress fluids (Park, 1972; Pascal, 1981; Al-Fariss and Pinder, 1987; Vradis and Protopapas, 1993; Chase and Dachavijit, 2003) in porous media with limited success. Most of these models have assumed oversimplified media and are unable to account for the interconnectivity, heterogeneity, and nonlinear opening of pores for fluids with a yield stress in real porous media. Moreover, the models usually require an empirical tortuosity constant which is not related to first principles.

The Al-Farris and Pinder (1987) model assumes the flow a Herschel-Bulkley fluid in a porous medium approximated as a uniform, tortuous bundle-of-tubes. Their model for Darcy velocity is given as:

$$u = \left[\frac{k}{H} \left(\nabla P - \nabla P_M \right) \right]^{1/n} \tag{2.12}$$

Where

$$\nabla P_M = \nabla P_T \sqrt{\frac{\phi}{2k}} \tau_0 \tag{2.13a}$$

$$H = \mu_o \left(\frac{3n+1}{4n} \right)^n \left(\frac{\phi k}{\beta^2} \right)^{1-n/2} \tag{2.13b}$$

For a uniform bundle-of-tubes, $\nabla P_T = 1$ and $\beta = \sqrt{2}$, but they depend on the pore structure for complicated porous media (moreover the effective pore structure changes as fluid is mobilized with increasing pressure gradient). Several authors have debated the value of β (Bird et al., 2007; Christopher and Middleman, 1965; Teeuw and Hesselink, 1980), but most agree that for shear-thinning fluids without a yield stress, it is a constant for a specific porous medium. Balhoff and Thompson (2006) also showed using network modeling that β is unique to a specific medium/pore structure and approximately independent of fluid properties (i.e. n and μ_o). Note that for fluids with $n = 1$, β is inconsequential; $H = \mu_o$. There are several assumptions in the Al-Farris and Pinder (1987) model, as described by Balhoff and Thompson (2004), which can lead to inaccuracies. The model does not account for heterogeneity in throat size; this heterogeneity results in nonlinear opening of pores that is lacking in this model. A more rigorous model would be needed to correctly predict Darcy velocity near the threshold pressure gradient.

2.6 NETWORK MODELS FOR FOAM

Rossen and Gauglitz (1990) presented a percolation model for the onset of foam generation, but did not extend it to foam flow. Chou (1990) developed a network model for foam in which lamellae do not move, but break and reform with a given frequency in pore throats. At any given instant, the throats not blocked represent the open fraction from percolation theory, and the relative permeability is the conductivity of a network with that open fraction. The viscosity of gas is unaffected by foam in this model, and

there is no minimum pressure gradient for flow. No explanation has been offered for why lamellae would repeatedly break (requiring high capillary pressure) and then reform by snap-off (requiring low capillary pressure) at the same pore throats (Rossen, 2003), however, as assumed in this model.

A number of studies have attempted to estimate the threshold pressure gradient for foam flow on a pore network. Chen et al. (2005b) modeled lamellae at discrete positions in a 2D square network, including capillary mechanisms for trapping and generation of new lamellae by snap-off and lamella division. In the model, lamellae advance in discrete steps in which each moving lamella crosses one pore body and divides if appropriate, and new lamellae are created by snap-off. All resistance to flow derives from capillary resistance at the lamellae; there is no velocity dependence, and no means to infer effective rheology.

Others have approximated foam, with its resistance to flow originating at discrete lamellae, with continuum fluids with a yield stress. As noted, this approximation does reproduce a minimum pressure difference for flow across a given pore throat that varies inversely with pore-throat radius, and a shear-thinning rheology for gas that does flow.

Rossen and Mamun (1993) examined how the minimum ∇P for flow depends on pore-throat-diameter distribution in a Bethe (or Cayle) tree network. In the Bethe tree all paths lead directly from inlet (center) to outlet (edge), so the network does not reproduce the geometric tortuosity of real networks. For some distributions, the following approximation works well for the threshold pressure gradient: truncate the pore-throat distribution at the percolation-threshold fraction of widest pore throats (Sahimi, 1993). Take the average ΔP for flow across these throats, and divide by the length of a single pore. This ratio approximates threshold pressure gradient (∇P_{M}). The true value of ∇P_{M} is somewhat smaller than this, and much smaller for extremely broad distributions of

pore-throat sizes. The threshold-∇P path does not travel exclusively through wide bonds, but sometimes selects a narrow bond if through it the path can access a string of narrow bonds.

Chen et al. (2005a) examined the flow of a Bingham-like fluid in 2D square networks with either narrow or wide pore-size distributions. For relatively narrow distributions, flow is nearly a quadratic function of ∇P minus the threshold value, and they suggest a cubic relative-permeability function. For wide pore-size distributions, which they argued better represents geological formations, flow rate is nearly linear with ∇P minus the threshold value, and the threshold ∇P is predicted reasonably well by the approximation of Rossen and Mamun (1993).

Sahimi (1993) used square (2-D) and cubic (3-D) networks having uniform throat conductivities and randomly distributed thresholds to model general nonlinear flow behavior. The results were not predictive of real media, because the conductivities were uniform and regular lattices were employed. Shah et al. (1995) used 2-D networks having a specified throat radii distribution to model a Bingham fluid flow. For different values of dimensionless yield stress, the open-throat patterns in the network were provided. They showed that the throat-size distribution and interconnectivity mainly controls threshold gradient (Balhoff and Thompson, 2004).

Balhoff and Thompson (2004) modeled the flow of yield-stress (Bingham) fluids in packed beds of spheres. They used 3D, physically-representative network models of porous media and consequently were able to obtain predictive results. In order to be as predictive as possible, they developed relationships for flow (through Finite Element modeling) in pore throats that accounted for converging/diverging geometry. Flow paths at the threshold gradient for flow were obtained and they developed macroscopic relationships between Darcy velocity and pressure gradient. In some cases, they were

able to obtain a good match between the model and experimental data. They did not rigorously investigate patterns of pore opening, effects of different pore networks, or applications directly related to foam. Sochi and Blunt (2008) modeled Herschel-Bulkley fluids in networks based on real sandpacks and Berea sandstone. They compared algorithms, Invasion Percolation with Memory (IPM) (developed by Kharabaf and Yortsos (1997)) and their method of Path of Minimum Pressure (PMP), to determine the threshold gradient. They obtained very similar results for the threshold path but PMP was orders of magnitudes faster. Balhoff et al. (2012) developed a new algorithm (Variable Jacobian Method), which is faster than Newton-Raphson algorithm, to solve the system of nonlinear equations associated to the flow of shear-thinning fluids with a yield stress through a pore-network model. They showed that the threshold gradient calculated by IPM is the same with the one obtained numerically.

Chapter 3: Network Modeling of Gas Trapping and Foam Mobility in Porous Media

The mechanism of resistance to flow for foam, originating virtually entirely at the individual lamellae, differs from that of a continuum fluid with a yield stress (Bird et al., 2007), but the essence of the two effects are similar: there is a minimum pressure gradient required to maintain flow, which is roughly proportional to the inverse of pore-throat radius, and a shear-thinning additional drag on flow beyond the threshold.

In this chapter the minimum macroscopic pressure gradient for flow of non-Newtonian yield-stress fluids through pore networks is examined with special attention to flow of foam in enhanced oil recovery (EOR). The pore networks are based on pore-level descriptions of real porous media. The accuracy of current models for flowing fraction and for gas mobility in foam in application to EOR is examined. Furthermore, the feasibility of splitting the gas mobility in foam into a relative permeability, represented as a function of flowing fraction, and an effective viscosity is studied. Finally, a new macroscopic model including pressure gradient-dependent macroscopic properties is presented.

3.1 Model Development

3.1.1 Network Model Generation

In this work, network models mapped from two different types of porous media are used: computer-generated sphere packs and sandstones digitized from real media. The sphere packs are obtained using a collective rearrangement algorithm (Jodrey and Tory, 1985) and have the advantage of fast generation and the ability to easily vary grain-size distribution and porosity. Network models of sandstones are more difficult to extract and pore-level properties are fixed. A network model constructed from a real, naturally-

occurring sandstone (Thompson et al., 2008) that was imaged using X-ray computed microtomography is used here (Liang et al., 2000; Lindquist et al., 2000; Al-Raoush et al., 2003).

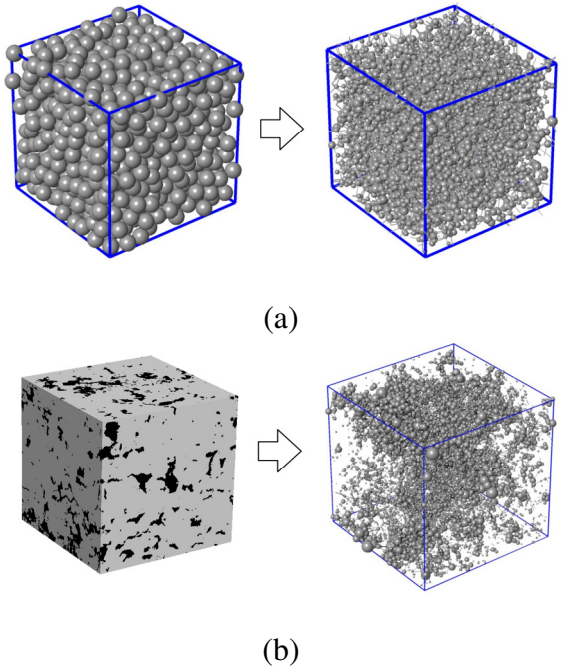

(a)

(b)

Figure 3.1 (a) Packed bed of 1000 uniform spheres with 38% porosity and the resulting network model and (b) Sample sandstone structure from the Frontier Formation in Wyoming, USA, with 17% porosity and the resulting network model (Gani and Bhattacharya, 2003; Thompson et al., 2008).

Regardless of the medium used, it is mapped to a 3D, physically-representative network model using a modified Delaunay tessellation (Al-Raoush et al., 2003). The resulting network captures the inherent heterogeneity and consists of pores (containing the pore volume) and connecting throats (accounting for resistance to flow). Figure 3.1 illustrates the two porous media and the resulting transformed network models. Dimensionless properties of the networks are described in Table 3.1. The permeability of each network can be varied through scaling (where the grain diameters are increased to increase permeability). Simulations are conducted using an average grain diameter, r_g, of

5.4×10^{-4} cm (k = 9.88×10^{-10} cm^2 (100 mD)) for the grain pack and, for the sandstone, 3.23×10^{-3} cm (k = 9.88×10^{-10} cm^2). However, all results presented are dimensionless.

Table 3.1 Statistics of sample porous media and corresponding network model.

Medium	**# Grains**	**# Pores**	ϕ	k_D*	$\bar{R}_D$*	$(\sigma_R)_D$*	$(L_c)_D$*
Grain Pack	1000	4070	0.38	3.38×10^{-3}	2.66×10^{-1}	9.32×10^{-2}	1.09
Sandstone	2487	4991	0.17	9.47×10^{-5}	3.06×10^{-1}	1.42×10^{-1}	1.44

$$* k_D = k/\bar{r}_g^2; \quad \bar{R}_D = \bar{R}/\bar{r}_g; \quad (\sigma_R)_D = \sigma_R/\bar{r}_g; \quad (L_c)_D = L_c/\bar{r}_g$$

3.1.2 Modeling of Flow Equations

Once generated, the network can be used to model many flow and transport problems. Modeling flow in the network requires solving a mass balance at every pore (i.e. flow into a pore from connecting throats must equal flow out). The connecting throats are usually modeled as capillary tubes that transmit flow to adjacent pores. Equations for flow rate as a function of pressure drop through these throats can be written that depend on the throat size (length and diameter) as well as the fluid rheology (viscosity). For a network of N pores, N equations can be written in terms of pressure at each pore. The resulting system of equations can be solved to determine the pore pressures in the network and the total flow rate (or velocity) for an applied pressure gradient in one direction.

For creeping flow of a Newtonian fluid, the relationship between flow rate and pressure drop in a throat is linear, and a linear system of equations results. The pore pressures can be determined using traditional methods for solving linear systems of equations. However, many fluids (e.g. polymers, drilling muds, foam, etc.) exhibit a

nonlinear relationship for flow and a nonlinear system of equations results. A multidimensional Newton-Raphson scheme is used to solve these equations.

Fluids that exhibit a yield stress require a minimum pressure gradient to initiate flow; the shear stress at the wall ($\tau_w = \Delta PR/2L$) must exceed the fluid yield stress (τ_o). Two constitutive equations often used to describe yield-stress fluids are the Bingham and Herschel-Bulkley model. Analytical expressions for flow rate as a function of pressure drop can be derived for a Bingham (Eq. 3.1) and Herschel-Bulkley (Eq. 3.2) fluid in a cylindrical tube starting from the constitutive equation for stress (Skelland, 1967).

$$q = \frac{\pi R^4}{8\mu_o L}\Delta P\left[1-\frac{4}{3}\left(\frac{2L\tau_0}{\Delta PR}\right)+\frac{1}{3}\left(\frac{2L\tau_0}{\Delta PR}\right)^4\right] \quad if\ \Delta P > \Delta P_m \equiv \frac{2L\tau_0}{R} \tag{3.1}$$

$$q = \frac{\pi R^3}{\mu_o^{1/n}\tau_w^{3}}\left(\tau_w-\tau_0\right)^{1/n+1}\left[\frac{\left(\tau_w-\tau_0\right)^2}{1/n+3}+\frac{2\tau_0\left(\tau_w-\tau_0\right)}{1/n+2}+\frac{\tau_0^{\,2}}{1/n+1}\right] \quad if\ \Delta P > \Delta P_m \equiv \frac{2L\tau_0}{R} \tag{3.2}$$

The Herschel-Bulkley model reduces to Bingham in the limiting case of $n = 1$. In these equations, flow is zero below a critical pressure drop and is finite above it. The no-flow region causes numerical difficulties in solution of the nonlinear system of equations. Here, the approach described by Balhoff and Thompson (2004) is used to solve the nonlinear system of equations.

3.1.3 Modeling of Foam Fluids

Foams exhibit similar behavior to yield-stress fluids in that a minimum pressure gradient is required to initiate flow. However, foam flow is governed by different physics than traditional yield-stress fluids. In the case of foam, the "yield stress" is not a fluid rheological property, but rather derives from the surface tension between surfactant solution and gas and is inversely related to pore-throat radius (Rossen, 1990a, 1990b, 1990c, 1990d; Cox et al., 2004). The functional relationship between threshold pressure

drop for flow across one pore and pore geometry is based on the Young–Laplace relation for static pressure drop over a curved lamella, which scales inversely with pore-throat radius (Falls et al., 1989; Rossen, 1990a, 1990b, 1990c, 1990d; Cox et al., 2004; Nguyen et al., 2004).

$$\Delta P_m \sim \frac{4\gamma}{R} \tag{3.3}$$

In the context of continuum fluid models like Eq. 3.1 and Eq. 3.2, where ΔP_m scales with $2L\tau_o/R$, this implies that the apparent yield stress τ_o is a constant. The magnitude of τ_o, when the models represent foams, reflects bubble size (number of lamellae per unit length along the flow path) and surface tension: the smaller the bubbles (more lamellae per unit length along the flow path), the larger the value of τ_o. For instance, the estimate of Rossen (1990b) for one simple case corresponds to an effective yield stress about 1/8 of the surface tension multiplied by the number of lamellae per unit length along the flow path for foam; but estimates depend on gas compressibility, drag on the lamellae, jumps made by the lamellae, and interactions with lamellae bounding trapped bubbles along the train (Rossen, 1990a, 1990b, 1990c, 1990d; Cox et al., 2004). Our approach includes the approximation of spreading the capillary resistance to flow along the entire gas phase rather than at discrete locations of lamellae. While not quantitatively correct, we contend that this approximation is adequate for examining the nature of the relation between pressure gradient and flowing fraction, and between flowing fraction and gas mobility. We neglect the influence of dynamic surface-tension effects such as the surface elasticity and surface viscosity during the motion of foam films in diverging–converging conical channels (Nguyen et al, 2004).

In addition to the Bingham (Eq. 3.1) and Herschel-Bulkley (Eq. 3.2) relationships, we test two simpler equations, which we call the constant viscosity foam model

(Equation 3.4) and power-law viscosity foam model (Equation 3.5). The model of Falls et al. (1989), fit to beadpack data, corresponds to Eq. 3.5 with $n = 2/3$.

$$q = \frac{\pi R^4}{8\mu_o L}\left[\Delta P - \Delta P_m\right] \quad if\ \Delta P > \Delta P_m \equiv \frac{2L\tau_0}{R} \tag{3.4}$$

$$q = \frac{\pi R^{3+1/n}}{4(2\mu_o L)^{1/n}}\left(\frac{4n}{3n+1}\right)\left[\Delta P - \Delta P_m\right]^{1/n} \quad if\ \Delta P > \Delta P_m \equiv \frac{2L\tau_0}{R} \tag{3.5}$$

As in the application of the other two models to foam, the apparent yield stress τ_o of the foam incorporates the capillary resistance to displacement of lamellae rather than a yield-stress condition at the pore-throat wall. The power-law viscosity foam model reduces to the constant viscosity model when $n = 1$. These equations have the advantage that scaling of flow rate with ∇P is simple above the threshold for flow in one tube, which makes it easier to distinguish viscosity effects (that control scaling of flow along one path with ∇P) and relative-permeability effects in our network model. They also allow one to test a range of shear-thinning and yield-stress behavior in a simple format.

Figure 3.2 compares the relationships of flow rate as a function of pressure drop for the foam models and traditional yield-stress fluids in a single dimensionless capillary tube or bundle of identical capillary tubes.

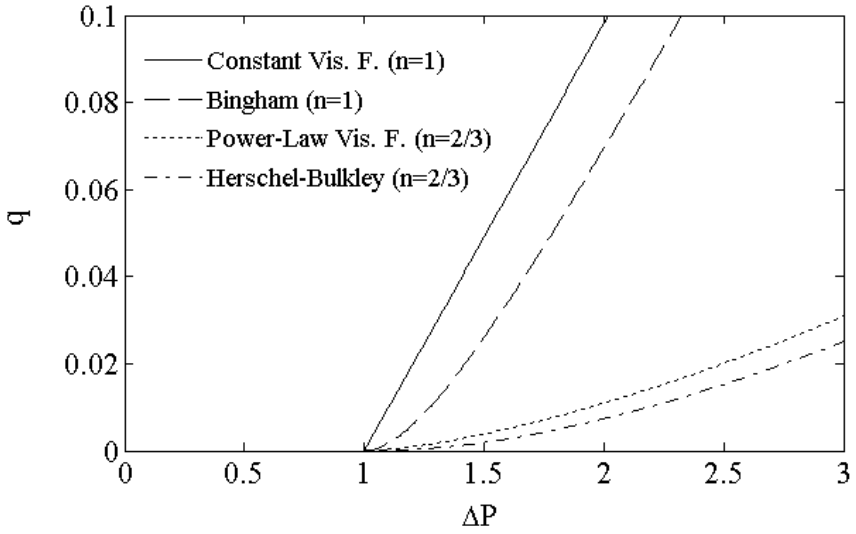

Figure 3.2 Flow rate (q) versus pressure drop (ΔP) in a dimensionless capillary tube (R = 0.5; L = 1) for constant viscosity foam, Bingham fluid, power-law viscosity foam (n = 2/3), and Herschel-Bulkley fluid (n = 2/3). All fluids have the same consistency index (μ_o = 1) and yield stress, τ_o = 0.25.

3.1.4 Converging/Diverging Geometry

Most network modeling studies assume throats are simple capillary tubes; however, porous media are converging/diverging and the pore throats should capture this behavior. Balhoff and Thompson (2004, 2006) conducted finite element simulations of yield-stress and other non-Newtonian fluids in converging/diverging throats. They used the results to develop new closed-form expressions for flow rate versus pressure drop valid in those geometries. They concluded the capillary-tube equation could be used for a Bingham fluid if the geometric parameters of the throat (R and L) are converted using results from the FEM simulation. They also showed (Balhoff and Thompson, 2006) that, to be rigorous, the capillary-tube equation cannot be used exactly for a Herschel-Bulkley fluid, but a good approximation can still be obtained. Therefore, the approach used in those works to convert converging/diverging throats to capillary tubes is used here for all

four models (Bingham, Herschel-Bulkley, constant viscosity foam, and power-law viscosity foam). Additional detail regarding the throat-size distributions can be found in the Appendix A.

3.1.5 Threshold Paths in the Network

Below a threshold pressure gradient, no flow occurs because there is no connecting path of throats that have pressure drops in excess of the local, throat mobilization pressure drop ΔP_{m}. In fact, below the threshold gradient, no throats are open because this would violate mass conservation. At the threshold gradient, a single flow path exists which connects one end of the network to the other. This threshold pressure gradient is exactly equal to the sum of the local mobilization pressure drops in the threshold path across the network.

$$L_{pn} \cdot \nabla P_M = \sum_i \Delta P_{m,i} \tag{3.6}$$

There are two ways to determine the threshold flow path and threshold gradient. The first involves a search algorithm to determine the minimum sum of mobilization pressure drops across the network. Sochi and Blunt (2008) compared two algorithms, Invasion Percolation with Memory (IPM) (Chou, 1990) and their algorithm, Path of Minimum Pressure (PMP), to determine the threshold path and obtained similar results. A second method simply involves solving the nonlinear system of flow equations at various applied pressure gradients and identifying the first pathway that forms. This approach can be numerically challenging, but successful techniques for solution are discussed by Balhoff and Thompson (2004). Regardless of the technique used, the same threshold gradient and path should be obtained.

In this study the opening of pores above the threshold pressure gradient also needs to be calculated and, therefore, the nonlinear flow equations are solved for an applied pressure gradient. Solution of the nonlinear system of equations results in flow rates in each throat and the pathway of pores that are open to flow can be easily determined. Convergence of the numerical solution occurs when the mass balance reaches a pre-defined tolerance. The Balhoff and Thompson (2004) approach involves imposing a large, but finite, viscosity in throats that are closed to find a solution for the pressure field, which may otherwise be indeterminate. The algorithm iterates, opening and closing bonds as the pressure field varies from iteration to iteration, until it converges. However, the solution may occasionally lead to isolated clusters of pores that appear to be open (material balance at each pore is below the tolerance) but do not form a connecting path in the network. The flow rates in throats connecting these pores are so small that they do not significantly affect numerical results for flow rate (i.e. Darcy velocity), but they can give inaccurate results for open pore volume. Therefore, once the numerical solution is complete, a "breadth-first search" is used to determine the open pores that form a connecting path(s) in the network and any isolated clusters are discarded. The algorithm also ensures that the pressure drop across each throat in the connecting path(s) exceeds the local throat threshold.

3.2 RESULTS AND DISCUSSION

The flow model (Bingham, Herschel-Bulkley, and the two foam models) is varied to investigate yield behavior. One goal of this work is to determine if universal relationships can be developed to describe the velocity and trapping of foam fluids. In order to develop these universal models, dimensionless parameters which are consistent with a bundle-of-uniform-tubes derivation of flow of shear-thinning fluids with a yield

stress in porous media (Al-Fariss and Pinder, 1987) are introduced here for pressure gradient and velocity.

$$\nabla P_D = \frac{\nabla P}{\tau_0}\sqrt{\frac{2k}{\phi}} \tag{3.7}$$

$$u_D = \frac{u^n}{\left(\frac{k}{H}\sqrt{\frac{\phi}{2k}}\,\tau_0\right)} \tag{3.8}$$

All results presented are for $\mu_o = 0.01$ Pa-s^n and τ_o = 0.7 dynes/cm^2. The results are presented in dimensionless form and are therefore independent of the medium permeability, porosity and the yield stress of fluid. Recall that H was defined in Eq. 2.13b in Chapter 2. The model is saturated with foam and flow is steady-state at constant pressure gradient.

3.2.1 Flow Paths

Flow simulations are conducted by imposing various pressure differences across the network model and investigating the resulting open flow paths. At low pressure gradients, fluid does not yield and no pores are open to flow. The threshold pressure gradient is the minimum pressure gradient required to induce flow.

Figure 3.3a shows the path at the threshold gradient ($\nabla P_D = \nabla P_T = 0.35$) in the uniform sphere packing for the four fluids: constant viscosity foam, power-law viscosity foam ($n = 2/3$ and $n = 1/3$), Bingham, and Herschel-Bulkley ($n = 2/3$ and $n = 1/3$). All simulations are performed in 3D, but the figure is collapsed into 2D for clarity. At the threshold gradient, 16 connected pores (out of 4070 total) open simultaneously. The threshold path is identical for all four fluids despite the flow equations being very different (Figure 3.2). For all fluids, the local mobilization pressure drop in a throat is

equal to ΔP_m. The disparities in flow behavior (Figure 3.2) above the mobilization pressure drop in a pore throat are irrelevant; at this threshold gradient q = 0 in all throats except those on the flow path, where the flow rates are infinitesimally small.

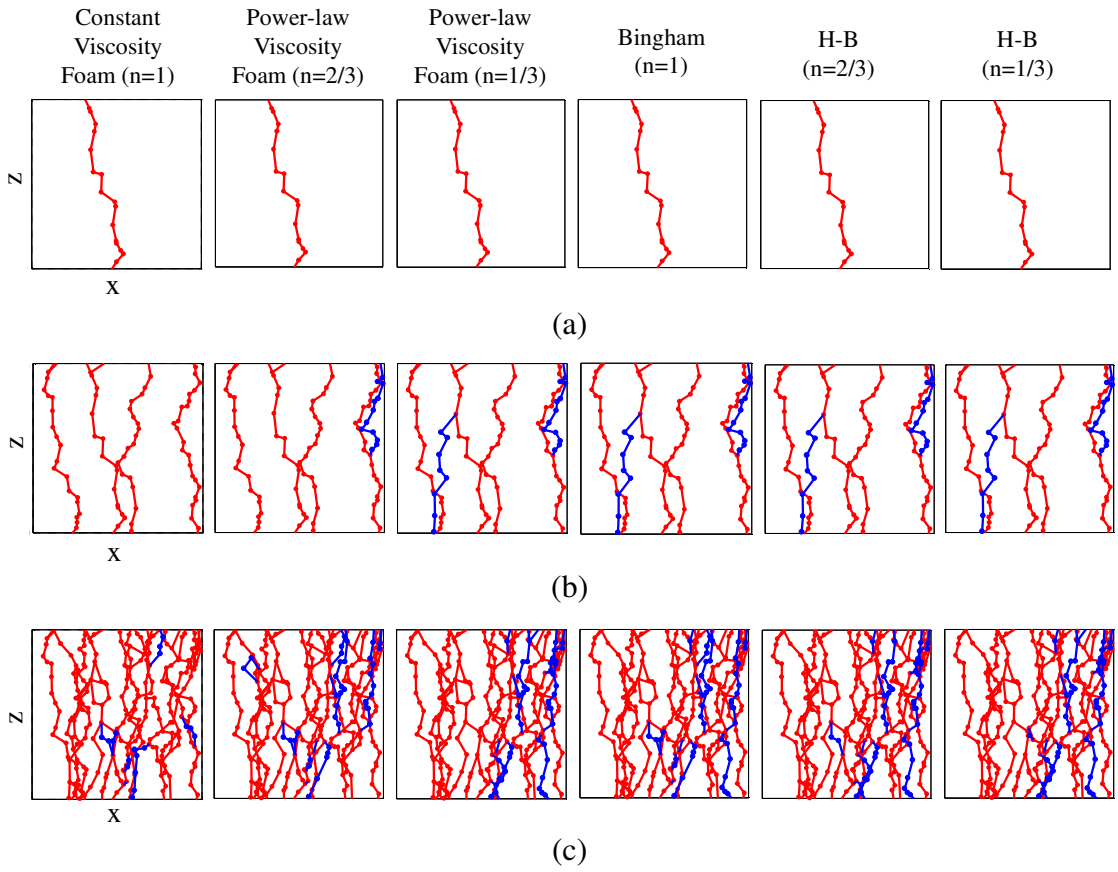

Figure 3.3 Flow paths in the grain pack for Bingham, Herschel-Bulkley (H-B), and Foam fluids (a) at the threshold ($\nabla P_D = \nabla P_T = 0.35$), (b) just above the threshold ($\nabla P_D = 0.41$), and (c) at higher pressure gradients ($\nabla P_D = 0.49$). Pathways in red are shared by all fluid models, and pathways in blue are specific to a particular model. All simulations are conducted by imposing a pressure gradient in the Z-direction.

One would expect the flowing fraction of foam to best approximate the backbone (conducting), not the percolation (connected) fraction, of a percolation cluster (Sahimi,

1993). In conventional percolation theory, however, even the backbone is a tortuous, inefficient pathway. For flowing foam, as in other "breakdown" problems, the path minimizes both its length and the number of expensive (narrow) bonds through which it travels. The structure would be expected to be very different from that of either the percolation or backbone fractions from percolation theory. In fact, the threshold path shown in Figure 3.4a is different from what would be obtained in classical percolation theory in Figure 3.4b. In classical theory, the percolation cluster corresponds to the set of connected pores/throats that are all wider than some critical radius. It does not allow for narrow pores/throats in the connected cluster, there is no penalty for tortuosity in the path, and the cluster includes dangling ends that do not conduct flow. Figure 3.4 compares the initial flow path at the threshold pressure gradient to the percolation cluster from classical percolation theory for the same grain pack. The initial pathway for flow in this case is not even part of the percolation cluster from classical percolation theory; it contains some throats narrower than the percolation-threshold radius (Rossen and Mamun, 1993).

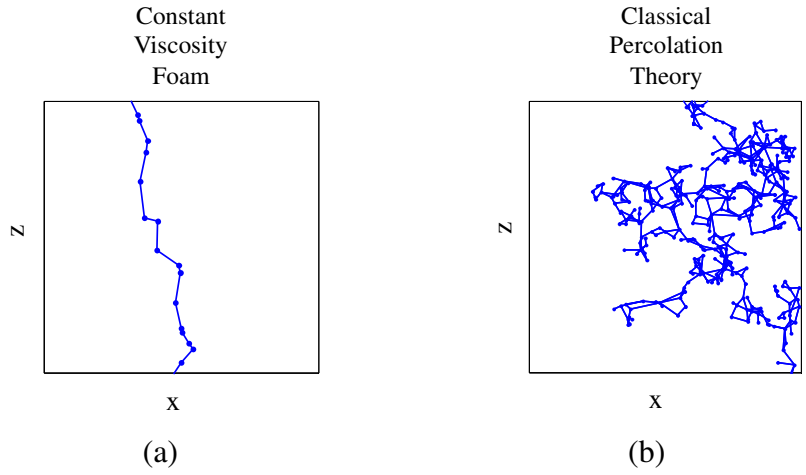

Figure 3.4 Flow path (a) at the threshold pressure gradient obtained from flow modeling and (b) percolation cluster at the percolation threshold obtained from classical percolation theory, both for the grain pack.

Figure 3.3b shows the flow paths at a pressure gradient just above the threshold ($\nabla P_D = 0.41$) where 77 - 97 pores are open. More than one pathway has formed but these individual paths are in general not connected to each other. Once again, these paths are nearly identical for the four fluid models despite the fact that the overall Darcy velocity and pressure distributions are (slightly) different. Evidently flow is dominated by yield-stress effects and not viscous effects at this pressure gradient. The pressure field in the open pores is different in the four simulations, but not enough to cause significant differences in trapping.

Figure 3.3c shows the open pores at a higher pressure gradient ($\nabla P_D = 0.49$): 282-313 pores are open. Individual flow pathways have merged and formed branches. The pore pressures reflect both yield-stress and viscous effects. As a result, pores/throats open in different sequences for the different fluid models (i.e. the pressure drop across a particular throat may be large enough to open for a simulation with one fluid model, but not another). The threshold path is independent of the fluid model, but the flow path at higher pressure gradients is dependent on the fluid model.

Figure 3.5 shows the flowing pathways for the sandstone for the four fluid models. Again, the pathway at the threshold gradient is independent of the fluid model; the same 40 pores open for each model. Above the threshold gradient pore opening is slightly dependent on the fluid model. An interesting observation for the sandstone is that the pattern for opening is different than the sphere pack. In the sphere pack, entirely new pathways form at low pressure gradients (Figure 3.3b). In the sandstone, pores open that are attached to the main backbone. This is partially due to the wider throat-size distribution in the sandstone (other paths require a significantly larger ∇P for flow than the threshold path); it may also represent autocorrelation in pore-throat radii or layering in the sandstone.

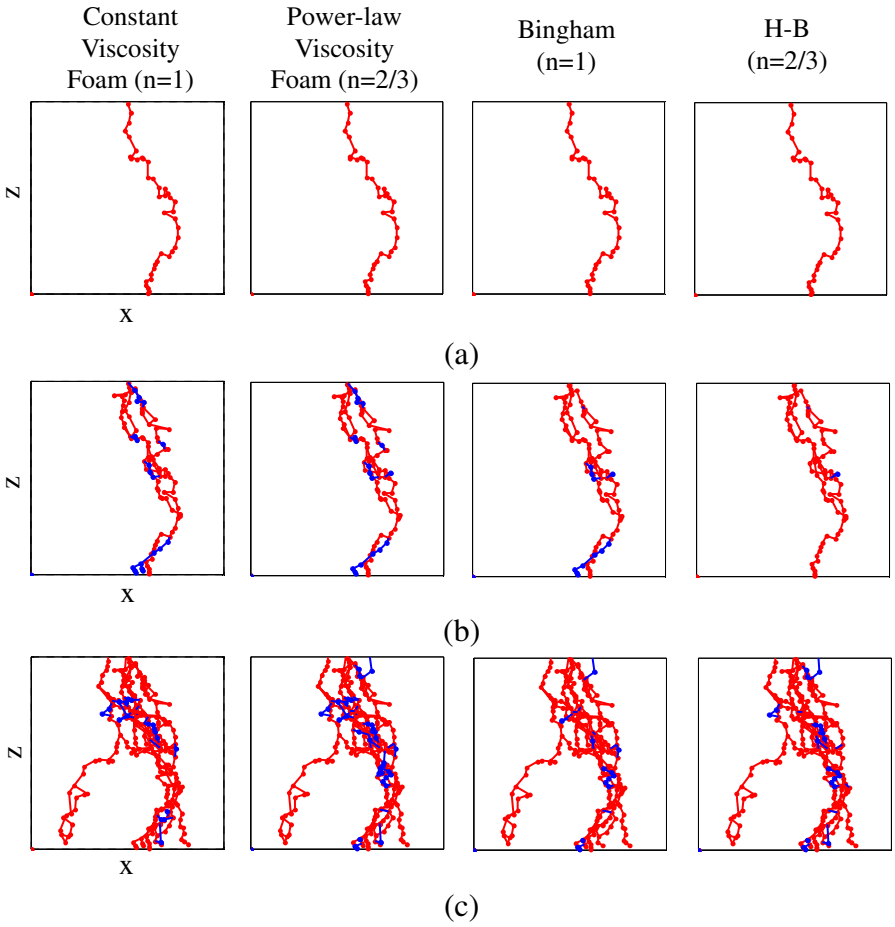

Figure 3.5 Flow paths in the sandstone for Bingham, Herschel-Bulkley (H-B), and Foam fluids (a) at the threshold ($\nabla P_D = \nabla P_T = 0.079$), (b) just above the threshold ($\nabla P_D = 0.085$), and (c) at higher pressure gradients ($\nabla P_D = 0.119$). Pathways in red are shared by all fluid models and pathways in blue are specific to a particular model. All simulations are conducted by imposing a pressure gradient in the Z-direction.

3.2.2 Pore Opening

Figure 3.6 is a plot of number of pores open versus dimensionless pressure gradient (∇P_D) for (a) the grain pack and (b) the sandstone. This corresponds to flowing fraction of foam, except that number of pores rather than cumulative volume is shown here. At the dimensionless threshold pressure gradient, a discrete number (16) of interconnected pores open simultaneously in the grain pack and in the sandstone (40). As

the pressure gradient increases, flow rate is increased through that flow path, but no additional pores open until a second path opens in the grain pack (Figure 3.3) with several additional pores. Figure 3.6a demonstrates a series of step changes in pore opening above the threshold gradient. Figure 3.6b shows less-dramatic steps. This is a result of a different pattern of pore opening (Figure 3.5); new pores tend to open in the sandstone that are already attached to the main backbone.

Figure 3.7a is a plot of percent pore volume flowing versus dimensionless pressure gradient, ∇P_D over a large range of pressure gradients on a linear scale. Figure 3.7b shows open volume fraction versus (∇P_D-∇P_T) (cf. Eq. 2.11 in Chapter 2) on a log-log scale. Pore volume is calculated through summation of volumes of all pore bodies along the flow paths. For flowing volume fraction below about 15% the slope of the trend line in Figure 3.7b is approximately 1.6 in the grain pack and 0.7 in the sandstone for the foam models.

The plots in Figure 3.7 are dimensionless and therefore independent of permeability, k. The flow path pore pressures, pore opening, and flow patterns are also independent of the fluid property, μ_o. The velocity is of course a function of "μ_o", but dimensionless velocity is independent of the fluid property by the definition in Eq. 3.8 and Eq. 2.12 in Chapter 2. Flow patterns and pore-opening are functions of the power-law index (n) as shown in Figure 3.6, because a different pressure field is computed. However, the effect of power-law index on open pore volume is relatively weak as shown in Figure 3.7.

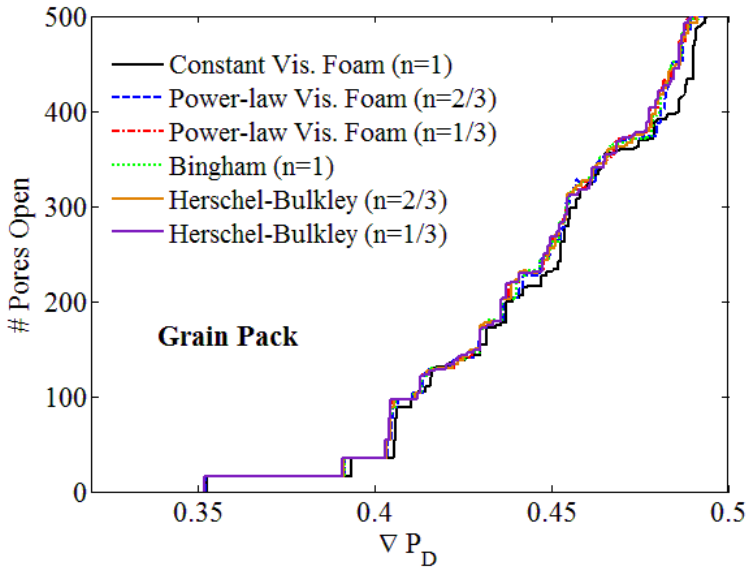

(a)

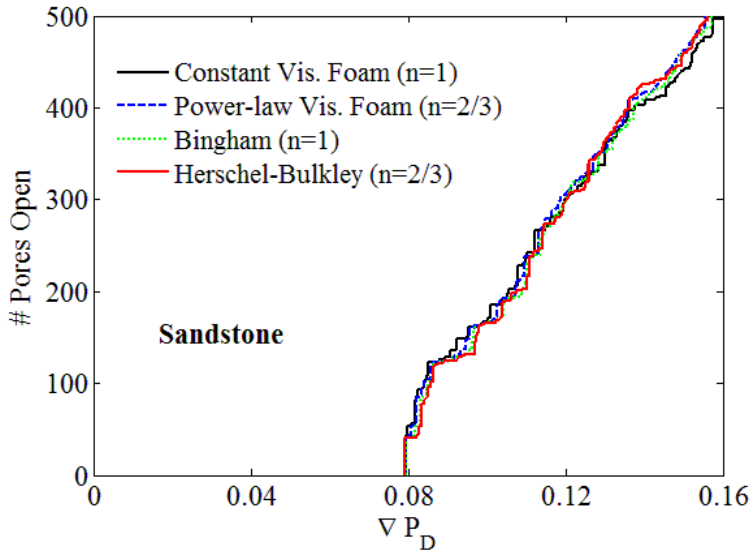

(b)

Figure 3.6 # Pores open versus dimensionless pressure gradient (∇P_D) for all fluid models near the threshold gradient in (a) a packing of uniform spheres with 4070 total pores and (b) sandstone with 4991 pores.

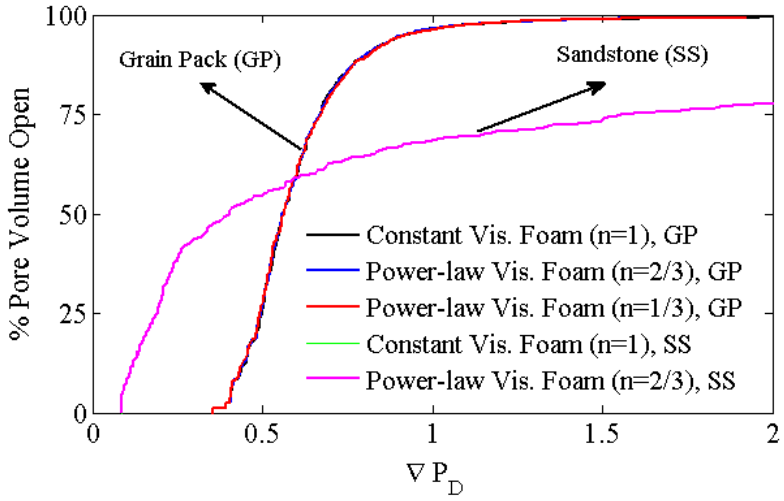

(a)

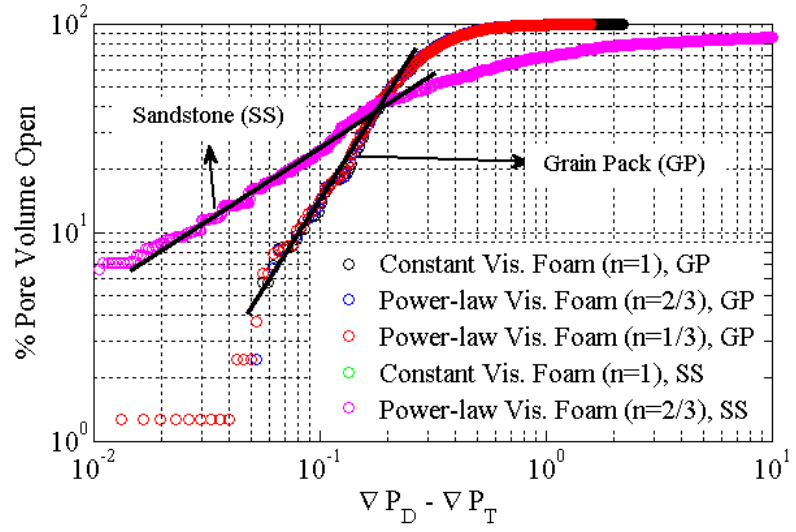

(b)

Figure 3.7 (a) Percent pore volume open (flowing) vs. dimensionless pressure gradient (∇P_D) and (b) percent pore volume open vs. (∇P_D-∇P_T) on a log-log scale for foam fluids in the grain pack (GP) and in the sandstone (SS). Straight lines are merely trends lines through the results.

A few key differences between the curves are observed for the grain pack and the sandstone:

1. The dimensionless threshold gradient for the sandstone ($\nabla P_T = 0.079$) is lower than the sphere pack ($\nabla P_T = 0.35$). The sandstone has a broader pore-throat size distribution (Table 3.1). It is more likely that the threshold path is formed with connected wide pores. Also, there can be spatial correlation in pore and throat size in the sandstone, since it is imaged from a real, natural medium; wide throats may tend to be connected to wide throats and narrow throats to narrow throats.
2. Scaling of open volume fraction with pressure gradient for sandstone is distinctly different from that for the sphere pack. Given the magnitude of this difference, it seems unlikely that any model like Eq. 2.11 in Chapter 2 could work for the range of porous media encountered in foam EOR in the field with a single scaling exponent.
3. Despite the smaller dimensionless threshold pressure gradient for flow, a larger dimensionless pressure gradient is needed to mobilize gas in all pores in the sandstone than in the sphere pack (Figure 3.7b). The wide throat radius distribution means that there is a wide difference between the pressure gradient required to open the first path for flow and to open the narrowest throats in the network.
4. The path at the threshold gradient represents a larger pore volume for the sandstone than for the sphere pack. The large fraction of pore volume in the initial path is largely due to the large number of pores in the connecting path for the sandstone (40 pores out of 4991) which contain 2.4% pore volume at the threshold. In the sphere pack, fewer pores open at the threshold (16 out of

4070) which contain only 1.3% of the pore volume. Moreover, the more heterogeneous and lower-porosity medium requires a more tortuous path to connect at the edges (cf. Figure 3.3 and Figure 3.5).

3.2.3 Dimensionless Velocity/Relative Permeability

One goal of this chapter is to develop a macroscopic, closed-form model for Darcy velocity of foam. Two approaches are taken to develop such a model. The first involves adapting existing models for yield-stress flow in porous media which are valid at large pressure gradients (but fail near the threshold). The second approach builds on existing scaling theories for foam flow that are based on modeling the threshold as a critical point (but are not expected to work far from the threshold).

3.2.3.1 Yield-stress Model

The Al-Farris and Pinder (1987) model for flow of Herschel-Bulkley fluids in porous media (represented as a bundle of uniform tubes) can be written in dimensionless form as

$$u_D = \nabla P_D - \nabla P_T \tag{3.9}$$

The model was derived under several limiting assumptions (Balhoff and Thompson, 2004). In fact, the model is invalid for Bingham and Herschel-Bulkley fluids near the threshold gradient even in a uniform bundle of tubes because it ignores additional nonlinearities in the flow equations (Eq. 3.1 and Eq. 3.2). The model is better suited for the foam models presented in Eq. 3.4 and Eq. 3.5 that do not have these nonlinearities.

For the foam models a linear relationship analogous to Eq. 3.9 is correct for $\nabla P_D >> \nabla P_T$ because all pores are open at large pressure gradients. Figure 3.8 shows the

dimensionless velocity versus dimensionless pressure gradient for foam fluid models (Eq. 3.4 and Eq. 3.5) in both the grain pack and sandstone. At large pressure gradients, the curve is straight with a slope of one. (Recall that the power-law exponent n is incorporated into the definition of the dimensionless velocity in Eq. 3.8.) However, the intercept of this straight line is greater than the threshold pressure gradient, ∇P_T.

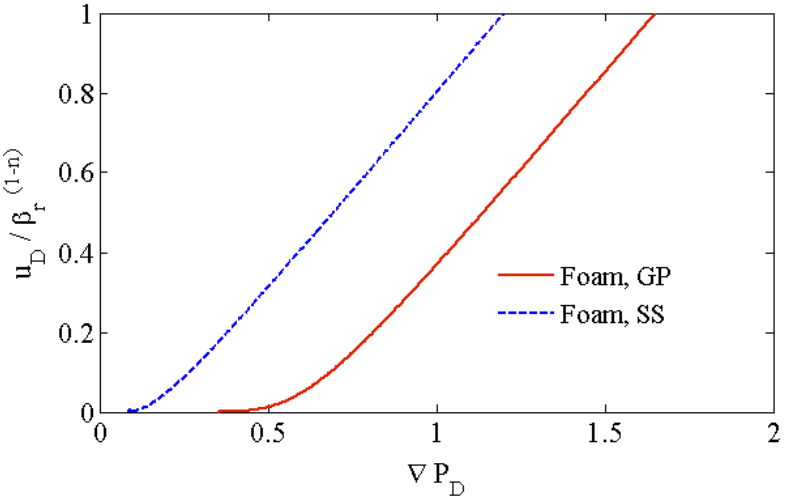

Figure 3.8 Dimensionless superficial velocity ($u_D/\beta_r^{(1-n)}$) versus dimensionless pressure gradient (∇P_D) for foam models in the grain pack (GP) and in the sandstone (SS). The curves are for all values of n investigated.

The superficial velocity is nonlinear near the threshold pressure gradient, however, as pores open and approaches the straight line (with slope one) at higher pressure gradients. For foam fluids, characterization of this nonlinear region is very important. The linear relationship between dimensionless velocity and pressure gradient would be correct only if the open fraction of pores were to remain constant (e.g. at large pressure gradients). However, pores open in a very nonlinear fashion as pressure gradient is increased and this effectively changes the porous medium at each pressure gradient. If one envisions the open pore volume at a particular pressure gradient as a "snapshot" of

the porous medium, the relationship between dimensionless velocity and dimensionless pressure gradient is linear in *that* porous medium. So the equation proposed in (3.9) is correct, except that the porous medium macroscopic properties (k, ∇P_T, and β for fluids with a shear-thinning index) are not constant. Recall that β is usually taken to be a constant for a specific porous medium (independent of fluid properties) for shear-thinning fluids (Eq. 2.12 and Eq. 2.13 in Chapter 2). For fluids with $n = 1$, β is inconsequential. For foam flow, each of these medium properties change with applied pressure gradient as pores open and the medium is effectively changed. A correction to the model is proposed here as:

$$u_D = k_r \beta_r^{1-n} \left(\nabla P_D - \nabla P_T^* \right) \tag{3.10}$$

In Eq. 3.10, the variables k_r, ∇P_T^*, and β_r change with open-pore volume and therefore must be determined as a function of pressure gradient for a specific porous medium. Network modeling simulations are conducted to determine these relationships for the grain pack and the sandstone.

1. k_r represents an effective relative permeability which changes with pressure gradient as pores open. At low pressure gradients, few pores are open and k_r is zero. At high pressure gradients, all pores are open and k_r approaches one. The nonlinear relationship can be found from the slope (numerical differentiation) of the curves shown in Figure 3.8 along with Eq. 3.10 using data for $n = 1$. When $n = 1$, the term β_r^{n-1} reduces to unity, so knowledge of β_r is not necessary.
2. ∇P_T^* represents the x-intercept of a linear plot of dimensionless Darcy velocity, u_D versus dimensionless pressure gradient, ∇P_D. As pores open, this value evolves from the true threshold gradient (∇P_T) to the intercept at large

pressure gradients (as shown in Figure 3.8). Using network model data for $n = 1$ and the k_r relationship found in step 1 along with Eq. 3.10, ∇P_T^* as a function of ∇P_D can be back-calculated at all pressure gradients.

3. β_r represents the change in the property β as pores open. It is only relevant for n < 1, because the term (β_r^{n-1}) reduces to one for $n = 1$. Using network model data for n<1, the calculated relationships for k_r and ∇P_T^* found in steps 1 and 2, and Eq. 3.10, β_r as a function of ∇P_D can be determined. β_r can be determined for any value of n, however, several authors (Christopher and Middleman, 1965; Teeuw and Hesselink, 1980; Balhoff and Thompson, 2006; Bird et al., 2007) have suggested it is independent (or nearly independent) of the shear-thinning index.

Figure 3.9 illustrates k_r, ∇P_T^*, and β_r as a function of dimensionless pressure gradient, ∇P_D in the grain pack and sandstone. The curves approach an asymptote at large pressure gradients where all pores are open. Eq. 3.10 in conjunction with the curves in Figure 3.9 may represent a model for all fluids for a given medium (different porous media may have different heterogeneities that result in different pore opening patterns). The model is independent of foam fluid properties, n, μ_o, and τ_o, at least in the sphere pack. Since the model is based on calibration using flow of a constant viscosity foam, however, application for real foams may be difficult.

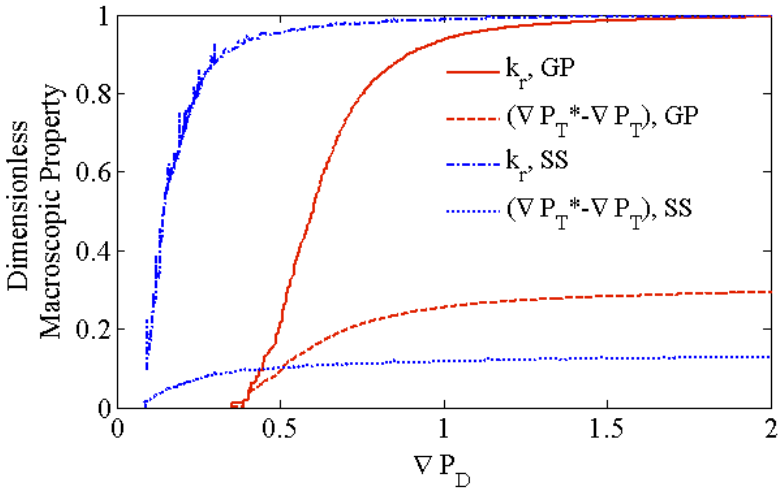

(a)

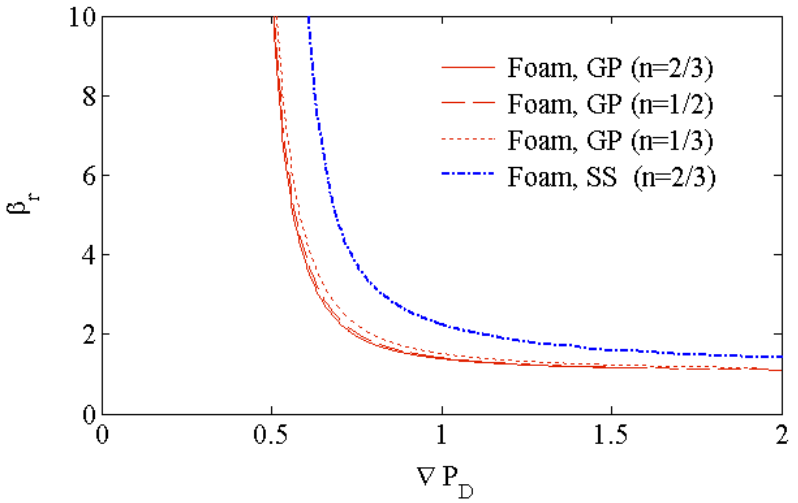

(b)

Figure 3.9 (a) Macroscopic properties k_r and ∇P_T^* for foam in the grain pack (GP) and in the sandstone (SS) plotted as a function of dimensionless pressure gradient (∇P_D) and (b) β_r as a function of dimensionless pressure gradient (∇P_D).

3.2.3.2 Foam Scaling Model

A plot of u_D versus (∇P_D-∇P_T) (Figure 3.10) for the foam models in the sphere pack and the sandstone illustrates the challenges in developing a universal scaling model

for foam flow. For the sandstone there is no single linear trend through the data, but an increase, and then a decrease, in slope.

For the grain pack, behavior is markedly different. For all the fluids, there is a distinct change in trend at a dimensionless pressure gradient (∇P_D-∇P_T) between about 0.05 and 0.1. At this ∇P, less than 10% of the foam is flowing (Figure 3.7b). For smaller pressure gradient, the dimensionless superficial velocity scales with about the 1.1 power of (∇P_D-∇P_T). Above this transition, dimensionless superficial velocity rises with different scaling for the two foam models.

An additional complication for real foams is that the relation between flow rate and ∇P along one pathway may be much more complex, and harder to unravel, than for the simple model fluids considered here (Rossen, 1990b).

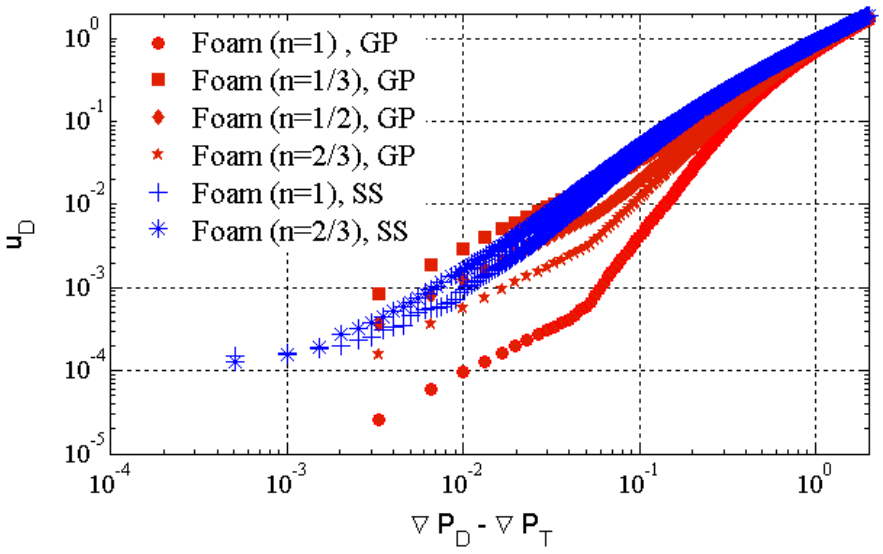

Figure 3.10 Log-log plot of dimensionless velocity (u_D) versus (∇P_D-∇P_T) for the two foam models in the grain pack (GP) and in the sandstone (SS) for different values of shear thinning index n. (n = 1)corresponds to constant viscosity foam model.

3.3 CONCLUSIONS

A physically-representative network model has been used to simulate flow through a porous medium of foams that require a minimum pressure gradient to yield. Mathematically, the process is similar to the flow of non-Newtonian fluids that exhibit a yield stress. As a result, we approximate flow using the popular Bingham and Herschel-Bulkley equations for flow in a tube, but also introduce two additional models that we call constant viscosity foam and power-law viscosity foam.

The network model is used to predict flow paths, the threshold pressure gradient, and Darcy velocity of foam in random packed beds of spheres and a sandstone imaged from real media. As expected, the initial flow path at the pressure threshold gradient is independent of the fluid model or fluid properties (μ_o and n). For packed beds of uniform spheres, the dimensionless threshold gradient is ~0.35. The path is radically different from either the percolation cluster or backbone cluster from classical percolation theory. Thus analogies between the two percolation-type problems are problematic. Above the threshold gradient, pore opening is a weak function of the fluid model and fluid rheological properties for the fluids studied; the pressure field in the porous medium is fluid-dependent and therefore the throat pressure drops may or may not exceed the local threshold depending on the fluid.

A network model of a sandstone sample yields at a lower dimensionless pressure gradient than a sphere packing and does not become completely open to flow until a much larger dimensionless pressure gradient. This is due to the greater heterogeneity of throat sizes and possibly autocorrelation in throat radii in the sandstone.

The scaling of flowing fraction with pressure gradient above the threshold pressure gradient for flow is markedly different for the sandstone and the grain pack. The dependence of superficial velocity on pressure gradient is likewise markedly different for

the sandstone and the grain pack. In the grain pack, there is a distinct change in the relation between superficial velocity and pressure gradient at a flowing fraction of about 6%.

A new dimensionless macroscopic model for foam flow in porous media is introduced. The model includes macroscopic properties that are dependent on the pressure gradient, since the open fraction increases with pressure gradient. The model works for all the nonlinear foam fluids which are tested for the sphere pack. However for different media, the pore-scale heterogeneities may be different and these pressure gradient dependent properties would need to be determined for that porous medium. In addition, the model requires calibration with a constant viscosity foam model, which may make application to real foams difficult.

Chapter 4: The Effect of Lamella Density on the Dynamics of Gas Trapping and Effective Gas Viscosity

In mechanistic modeling of foam in porous media, reduced gas mobility is attributed to viscous resistance of flowing foam lamellas to gas flow, while gas trapping significantly modifies relative permeability. By using pore-network models representative of real porous media, a relationship between flowing gas fraction and pressure gradient for strong foam (high lamella density) were developed in the previous chapter (Balan et al, 2011a, 2011b).

In this chapter, our model is expanded to describe the effects of foam strength and pore-scale apparent gas viscosity models on both gas relative permeability and effective gas viscosity. Dimensional analysis in scaling of these two rheological quantities with pressure gradient and lamella density is discussed. Furthermore, the dynamics of foam mobilization and mobility in a pore-network model where the respective effects of lamella density and rheological behavior of flowing foam on gas trapping and relative gas permeability are quantified for the first time. This enables the verification of the functional relationship between effective gas viscosity and flowing lamella density in the presence of dynamic trapped gas. The following section gives a detailed description of our modeling approaches for capturing these two rheological aspects of foam mobility in porous media.

4.1 Model Development

4.1.1 Pore-Network Model

Simulations are performed using the 3D pore-network model mapped from a computer-generated sphere pack which was introduced in Chapter 3 (Figure 3.1a). Dimensionless properties of the network were provided in Table 3.1 in Chapter 3. The

mean grain radius used in the simulations is 5.4×10^{-4} cm ($k = 9.88\times10^{-10}$ cm^2 (100 mD)). However, all results presented are dimensionless. Moreover, the porous medium has a porosity of 38%. If necessary, the permeability of the pore network can be adjusted by changing the grain (and therefore domain) size.

4.1.2 Lamella Flow Equations

Three different apparent gas (lamella) viscosity models are tested in this chapter: constant, power-law, and Hirasaki-Lawson (1985). These viscosity models in Table 4.1 are substituted into a continuum capillary flow equation with a mobilization pressure difference in Eq. 4.1 to represent a lamella flow through a pore throat (Table 4.2)

$$q = \frac{g}{\mu_{app}}\left[\Delta P - \Delta P_m\right] \quad ; \quad \Delta P \geq \Delta P_m \tag{4.1a}$$

$$g = \frac{\pi R^4}{8L} \tag{4.1b}$$

where q is flow rate in a pore throat, g is hydraulic conductivity of a pore throat, μ_{app} is pore-scale apparent gas viscosity, ΔP is pressure drop in a pore throat, and ΔP_m is mobilization pressure difference across a pore throat.

Table 4.1 Apparent gas (lamella) viscosity models.

Constant	$\mu_{app} = \mu$
Power-Law	$\mu_{app} = \mu_o \left(\frac{3n+1}{4n}\right)^n \left(\frac{R}{4v_g^f}\right)^{(1-n)}$
Hirasaki-Lawson (1985)	$\mu_{app} = 0.85 \frac{\mu_w (R/L)}{(r_c/R)} \left(\frac{\gamma}{3\mu_w v_g^f}\right)^{1/3} \left[\left(\frac{r_c}{R}\right)^2 + 1\right]$

Table 4.2 Fluid models representing a lamella flow through a pore throat.

Apparent Gas (Lamella) Viscosity Models	**Lamella Flow Equations**
Constant	$q = \frac{g}{\mu}\left[\Delta P - \Delta P_m\right]$
Power-Law	$q = \frac{g}{\mu_o^{1/n}}\left(\frac{4n}{3n+1}\right)\left(\frac{R}{2L}\right)^{(1/n)-1}\left(\Delta P - \Delta P_m\right)^{1/n}$
Hirasaki-Lawson (1985)	$q = \frac{g}{\frac{3\mu_w R^2}{8\gamma L}\left(2.26\frac{\gamma}{r_c}\left[\left(\frac{r_c}{R}\right)^2 + 1\right]\right)^{3/2}}\left[\Delta P - \Delta P_m\right]^{3/2}$

Since no mass transfer is taken into account, the constant lamella viscosity model relies on an assumption that the viscous drag force exerted by the wetting layer on the moving Plateau border is proportional to the shear rate at the wetting film-Plateau border contact (film velocity) for a given wetting layer thickness (Nguyen et al., 2004) (Figure 4.1). Due to the continuity of the liquid within the Plateau border and the wetting film, the viscous stress is of the order of ($\mu_w v_g^f/\delta$), where δ is the wetting layer thickness, μ_w is the water viscosity, and v_g^f interstitial gas velocity with foam lamella.

However, the above approximation is not very accurate when the effect of the viscous drag force on the shape of the surface region tangential to the wetting film becomes significant. This effect was first theoretically described by Bretherton (1961) and then extended by Hirasaki and Lawson (1985) to the motion of lamellas separated gas. In the latter study, the apparent gas viscosity was found to be proportional to $(v_g^f)^{-1/3}$ suggesting a shear thinning behavior of lamella flow in a straight capillary tube. In this study, the mechanistic Hirasaki-Lawson apparent gas viscosity model is compared with the empirical power-law viscosity model. Since the lamella flow equation with the power-law viscosity model reduces to the constant viscosity model when $n = 1$, these two

simple models have the advantage that scaling of flow rate with pressure gradient is much simpler above the threshold for flow in one tube, which makes it easier to distinguish viscosity effects and relative-permeability effects in our network model. They also allow one to test a range of shear-thinning and yield-stress behavior in a simple format. Therefore, the constant viscosity model is used here to determine flowing gas fraction as a function of overall lamella density and pressure gradient, and then evaluate the effect of different viscosity models (i.e. Power-Law and Hirasaki-Lawson models) on this functional relationship.

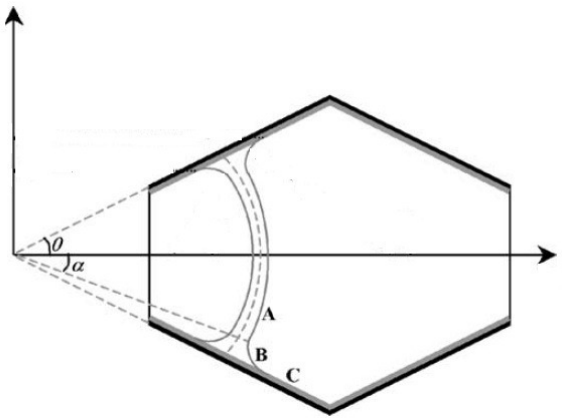

Figure 4.1 Schematic of a foam lamella in a hypothetical converging-diverging pore. Main sections of a lamella: (A) central thin film, (B) the plateau border, and (C) liquid wetting film on pore surface (modified from Nguyen et al. (2004)).

Gas trapping is mainly governed by either entry capillary pressure or resilience of lamellae. The former even occurs in a non-dispersed two-phase system during drainage, where gas cannot invade some liquid-filled pore throats of high entry capillary pressure (sometime called dead-ends to the invading fluid). The latter, that is most important in steady-state foam flow or imbibition following steady-state foam, relates to the inherent

yield property of lamellas in divergent flow channels. Like bulk foam – where Bingham plastic behavior is expressed through deformation of a foam interface before either its rupture or mobilization (Prud'homme, 1981; Princen, 1983; Heller and Kuntamukkula, 1987), the yield stress of a curved lamella in a divergent pore is nothing but the imposed pressure gradient that is counterbalanced by the equilibrium lamella tension (γ). Therefore, it may scale as

$$\Delta P_m \sim \frac{\gamma}{R} \tag{4.2}$$

where R is pore-throat radius and ΔP_{m} is mobilization pressure difference across a pore throat.

Note that this static yield stress can significantly be modified during a stretching-contracting motion of the lamella because of surface elasticity and viscosity (Schramm, 1994; Schramm and Green, 1995). As a result, besides pore radius (frequently taken as pore throat radius), the dynamic lamella tension also determines the magnitude of the yield pressure gradient (Xu and Rossen, 2000; Falls et al., 1989) under dynamic conditions. However, this effect is not considered in this study.

In general, the flow equations in Table 4.2 are only applicable for flow in a straight capillary tube and need some modifications to capture the effect of converging and diverging structure of real porous media on fluid flow. Balhoff and Thompson (2004, 2006) developed a function to convert the geometric parameters of a real pore throat to an equivalent capillary by performing finite element simulations of power-law and yield stress fluids. This conversion helps to make better predictions of threshold pressure gradient at the macro scale and it is employed here due to the similarity between the flow of yield-stress fluids and the flow of a foam lamella through a pore throat.

4.1.3 Definition of Lamella Density

Lamella density is a good measure of foam strength. It is believed that stronger foam in a porous medium exhibits finer bubbles whose sizes are limited by pore sizes (Falls et al., 1988). Weak foam has coarse texture with lamella spacing of several pore lengths. In this sense, the effect of lamella density in the pore network is investigated by specifying the number of lamellas and then distributing them over the pore throats. It is assumed that lamellas are randomly distributed in the pore network without autocorrelation, and that this simplification does not represent the dynamics of lamellae generation and destruction by, for example, lamella division or snap-off during foam flow. Different realizations of spatial lamella distribution are used in favor of the fact that exact location of each lamella during flow in porous media is unknown. Therefore, our model does not explicitly simulate the movement of one lamella from one pore to another. Instead, it captures the lamella moving process by performing simulations for different lamella distributions in the network at constant overall lamella density and constant pressure gradient. Each realization represents a snapshot of the lamella flowing process (Figure 4.2).

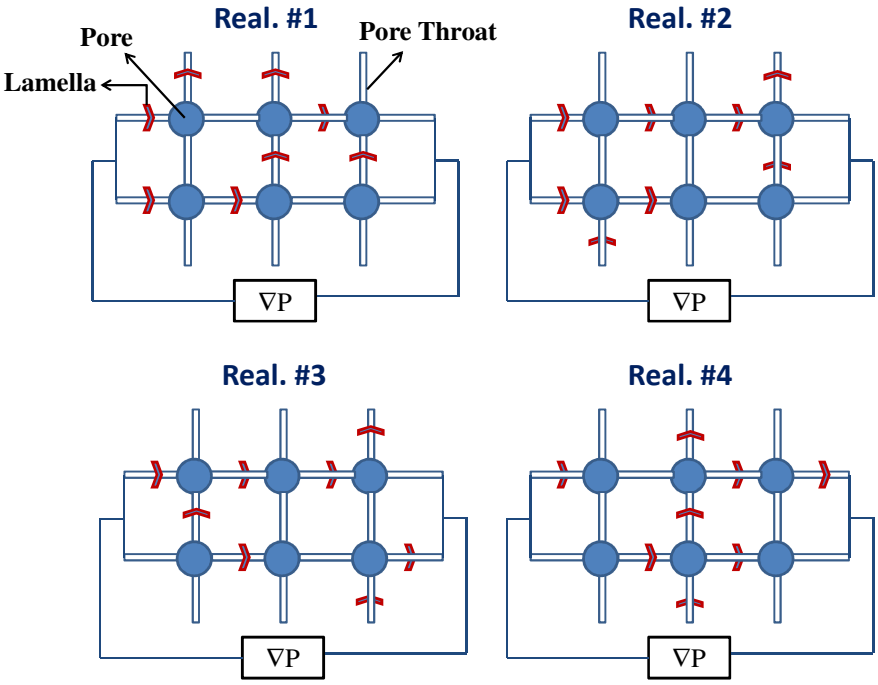

Figure 4.2 Schematic of four different realizations of lamella distribution in a hypothetical network at constant overall lamella density and constant pressure gradient across the network.

A sketch of the proposed model is shown in Figure 4.3a. Consider a pore with four throats; two (pore throats #1 and #4) have one lamella, while the other two (#2 and #3) do not have lamella. If the constant lamella viscosity model (Table 4.1) is employed to represent gas flow with lamella through the pore throats (Table 4.2), the respective plots of the flow equations for each throat are as depicted in Figure 4.3b. Gas flow through a pore throat without a lamella (throats #2 and #3) is represented by the Newtonian flow equation with an assumption that gas compressibility is negligible. This assumption is valid for small pressure gradient as compared to the system pressure. Modeling flow in the network requires ensuring mass balance at every pore; this leads to a system of N equations (N being the number of pores), where pore pressures are the unknowns. The resulting system of equations can be solved to determine the pore

pressures in the network and the total flow rate (or velocity) for an applied pressure gradient in one direction. A detailed description of the matrix equation of the pore-network model is provided in the Appendix B. The fluid flow equations representing a lamella flow through a capillary tube in Table 4.2 are nonlinear and therefore a multidimensional Newton-Raphson scheme is used to solve a system of these equations.

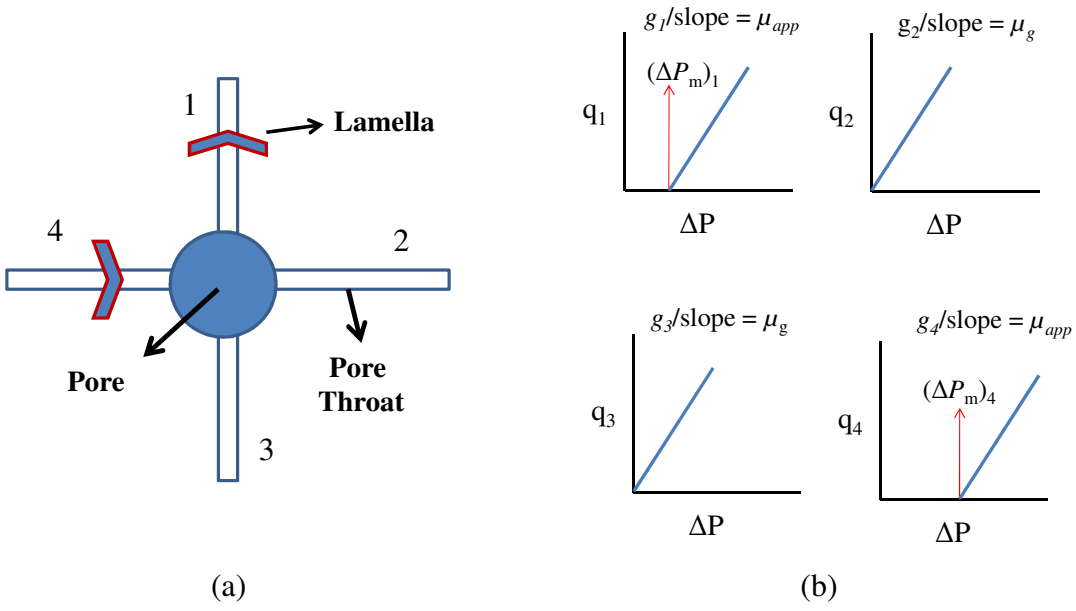

Figure 4.3 (a) A sketch of the proposed model for a representative pore and its throats and (b) the respective plots of flow equations at each pore throat.

Two different lamella density definitions are used in this study (Table 4.3) to make comparisons between our results and the theoretical studies in literature. In the first definition, flowing lamella density (ρ_{fg}^{L}) is defined as the number of flowing lamellas (N_{fg}^{L}) divided by the number of pore throats in the flowing gas domain (N_{fg}^{T}), while overall lamella density (ρ_{t}^{L}) is defined as the total number of lamellas in the pore-network (N^{L}) divided by the total number of pore throats (N^{T}). In the second definition, the number of flowing lamellas (N_{fg}^{L}) is normalized to the flowing gas volume (V_{fg}) and the

number of total lamellas (N^L) to the total gas volume (pore volume in our case) (V_g). The first definition of lamella density is used throughout the paper unless otherwise specified.

Table 4.3 Different definitions of lamella density

	Flowing Lamella Density	**Trapped Lamella Density**	**Overall Lamella Density**
Def. 1	$\rho_{fg}^{L} = N_{fg}^{L} / N_{fg}^{T}$	$\rho_{tg}^{L} = N_{tg}^{L} / N_{tg}^{T}$	$\rho_{t}^{L} = N^{L} / N^{T}$
Def. 2	$n_{fg}^{L} = N_{fg}^{L} / V_{fg}$	$n_{tg}^{L} = N_{tg}^{L} / V_{tg}$	$n_{t}^{L} = N^{L} / V_{g}$

4.1.4 Scaling Trapped Gas

Gas trapping is driven by the pore-scale differential pressure relative to the mobilization pressure drop (ΔP_m) across each pore throat occupied by a lamella. The latter depends on the lamella interfacial tension and pore geometry. The local pressure field in a pore network with N pores could be obtained from the solution of Eq. B.4 in the Appendix B**.** Therefore, once the numerical solution is complete, a "breadth-first search" is used to determine the open pores that form a connecting path(s) in the network and any isolated clusters are discarded. Eq. B.4 shows that the local differential pressure distribution is determined by overall lamella density, spatial lamella distribution in the network, the contrast between the apparent and ordinary gas viscosities, and the shear thinning effect of moving lamellas.

For the purpose of scaling trapped gas fraction with the characteristics of permeable medium, fluids, and flow, the following dimensionless macroscopic pressure gradient is used (Balan et al., 2012):

$$\nabla P_D = \frac{\nabla P}{(2\gamma / L_c)} \sqrt{\frac{2k}{\phi}} \tag{4.3}$$

where γ is interfacial tension between surfactant solution and gas, L_c is characteristic pore-throat length of the pore network, k is absolute permeability, ϕ is porosity, ∇P is pressure gradient, and ∇P_D is dimensionless pressure gradient.

Unless otherwise specified, permeability, characteristic pore-throat length of the pore network, interfacial tension between water and gas are 9.88×10^{-10} cm^2 (100 mD), 5.88×10^{-4} cm, and 30×10^{-3} N/m, respectively. Moreover, the shear-thinning index for the power-law viscosity model (n) is (2/3). However, all results presented are dimensionless. Since there are only gas and lamellae in the network, total gas saturation is equal to 1.0 and thus the flowing gas fraction is defined as flowing gas saturation, S_{fg} in Eq. 4.4.

$$X_{fg} \equiv S_{fg} \quad \text{with} \quad S_g = 1.0 \tag{4.4}$$

4.2 Results and Discussion

4.2.1 Gas Trapping

Figure 4.4a shows the relationship between flowing gas fraction (X_{fg}) and dimensionless pressure gradient (∇P_D) for different overall lamella densities (ρ_t^L). The lamella flow equation with the constant viscosity model is used and apparent gas (lamella) viscosity is equal to regular gas viscosity in this case. X_{fg} increases with decreasing overall lamella density in the pore network at fixed pressure gradient. Therefore, it is easier to open flow paths at lower overall lamella density. It is also found that there exists a threshold pressure gradient (∇P_T) as overall lamella density increases above 0.65 and that the threshold pressure gradient nonlinearly increases with overall lamella density.

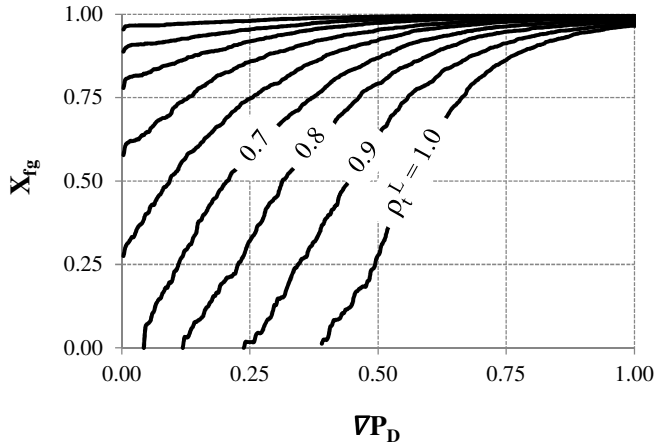

(a)

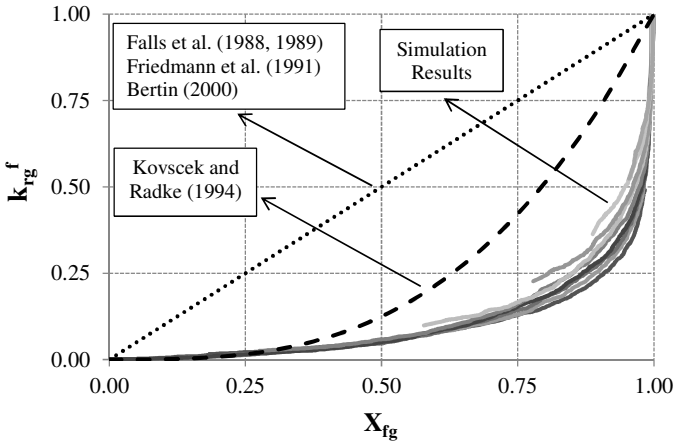

(b)

Figure 4.4 (a) Flowing gas fraction (X_{fg}) vs. dimensionless pressure gradient (∇P_D) for different overall lamella densities in the pore network (ρ_t^L) and (b) gas relative permeability with foam (k_{rg}^f) vs. flowing gas fraction (X_{fg}). The lamella flow equation with the constant viscosity model is used for our results. No viscosity contrast between lamella and gas.

Figure 4.4b shows the gas relative permeability with foam (k_{rg}^f) as a function of flowing gas fraction for different overall lamella densities, compared with the theoretical correlations proposed by Falls et al. (1988, 1989), Friedmann et al. (1991), Kovscek and Radke (1994). It could be concluded from this figure that the effect of overall lamella density on the shape of the gas relative permeability with foam curve is not very

significant. Therefore, flowing gas fraction, which is a function of overall lamella density, mainly determines the relative permeability of the flowing gas. In addition, the results indicate that the gas relative permeability increases nonlinearly with the flowing gas fraction, which is qualitatively consistent with Kovscek and Radke (1994). Note that the gas relative permeability curves in Figure 4.4b have different end points because of the difference in overall lamella density used in these cases.

Figure 4.5a shows that flowing lamella density (ρ_{fg}^{L}) is zero at low pressure gradient when overall lamella density, ρ_t^{L} is lower than 0.7, consistent with zero threshold pressure gradient observed in Figure 4.4a. Flowing phase prefers the least resistant pathways at a specific pressure gradient. Overall lamella densities, ρ_t^{L} lower than 0.65 enables gas to flow through lamella unoccupied paths at low pressure gradient and to mobilize lamella at elevated pressure gradient, resulting in an increase in flowing lamella density, ρ_{fg}^{L} within the flowing gas domain. This foam flow regime is first defined by Falls (1988) as continuous-gas foam flow to contrast with discontinuous-gas foam flow regime (Figure 4.6) in which the pressure gradient must exceed a threshold value to set flow (X_{fg} curves for $\rho_t^{L} > 0.65$ in Fig. 4.4a). Moreover, combining Figs. 4.4a and Fig. 4.5a clearly reveals that the threshold pressure gradient, ∇P_T decreases with the overall lamella density for $\rho_t^{L} > 0.65$ (Fig. 4.4a) while the pressure gradient required to mobilize lamella for $\rho_t^{L} < 0.65$ increases with decreasing overall lamella density (Fig. 4.5a). In other words, the pressure gradient for mobilizing at least one lamella varies with the overall lamella density and reaches a minimum at ρ_t^{L} around 0.65.

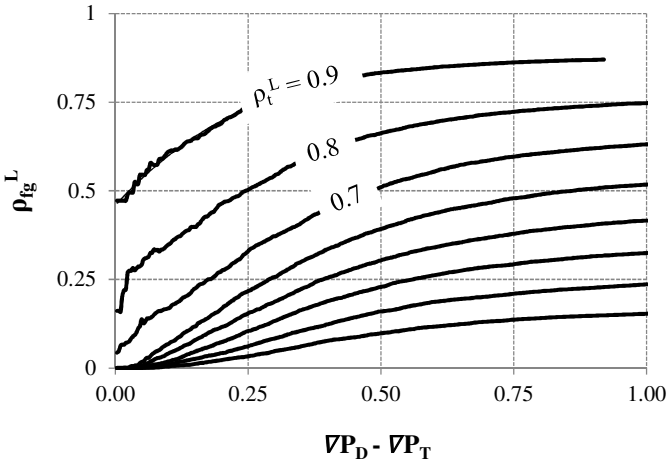

(a)

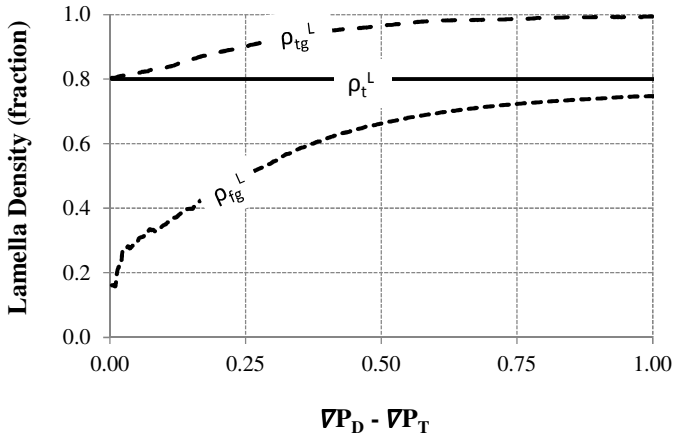

(b)

Figure 4.5 (a) Flowing lamella density (ρ_{fg}^L) vs. normalized dimensionless pressure gradient (∇P_D-∇P_T) for different overall lamella densities in the pore network (ρ_t^L), and (b) flowing (ρ_{fg}^L) and trapped (ρ_{tg}^L) lamella density vs. normalized dimensionless pressure gradient (∇P_D-∇P_T) at a constant overall lamella density (ρ_t^L) of 0.8. The lamella flow equation with the constant viscosity model is used in these simulations. No viscosity contrast between lamella and gas.

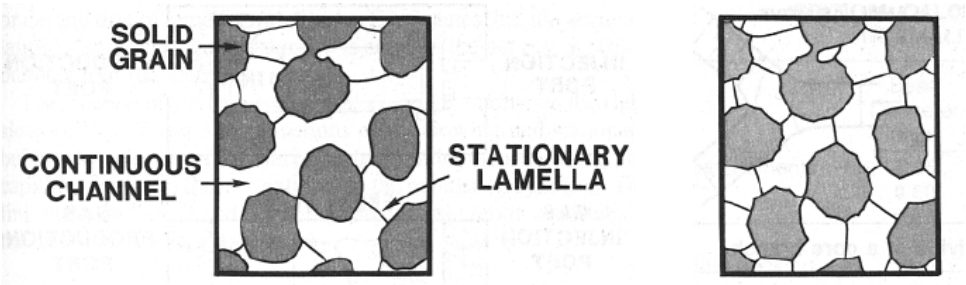

Figure 4.6 Schematic of (a) continuous-gas foam, and (b) discontinuous-gas foam (Falls et al., 1988).

The flowing lamella density converges to the overall lamella density as pressure gradient is high enough to open all pores in the network to flow. As demonstrated in Figure 4.5b flowing lamella density, ρ_{fg}^{L} converges to the overall lamella density, ρ_{t}^{L} of 0.8 while trapped lamella density (ρ_{tg}^{L}) converges to 1.0 when pressure gradient increases. This important result does not help us validate one of the main assumptions underlying the population balance based foam modeling approaches (Kovscek et al., 1995, 1997) that is flowing lamella density is equal to trapped lamella density.

Note that the above results are based on one realization of spatial lamella distribution in the network. Different patterns of lamella distribution may modify the functional relationships between the gas relative permeability, trapped gas fraction, and pressure gradient. This hypothesis could be tested by evaluating the variation of these relationships for multiple realizations. More than 50 different realizations for each overall lamella density have been tested and the test results for two different overall lamella densities, ρ_{t}^{L} (0.4 and 0.8) and 6 distributions of lamellas in the pore network are shown in Figure 4.7. These six realizations represent both “heterogeneous” and “homogeneous” type distribution of lamella in the network. The former means that the lamellas are mixed

well with all the pore throats in the network. In the heterogeneous cases, the difference between maximum and minimum values of local lamella densities in the pore network is very high while the overall lamella density is kept constant. A detailed description of the heterogeneous lamella distribution cases is provided in the Appendix C. For low overall lamella density ($\rho_t^L = 0.4$) (Figure 4.7a), the heterogeneity of lamella distribution does have an obvious influence on flowing gas fraction. However, this influence is significantly reduced for high overall lamella density ($\rho_t^L = 0.8$) as shown in Figure 4.7b. It is also found that the relationship between gas relative permeability and flowing gas fraction (Figure 4.4b) is not modified by the variation of lamella distribution over a wide range of lamella density. This suggests that modeling of the movement of lamellae from one pore to another may be unnecessary to obtain macroscopic rheological foam properties at a constant overall lamella density.

Due to significant lamella resistance to flow, one may suspect that the viscosity contrast between gas and lamella would influence trapped gas fraction through modifying the local pressure field at fixed pressure gradient across the pore network. To quantify this effect, four different hypothetical viscosity contrasts are investigated for two different overall lamella densities and the results are shown in Figure 4.8. It is interesting to observe from this figure that pore-scale viscosity contrast is not an important factor controlling flowing gas fraction and thus gas relative permeability with foam on a macroscopic scale over a wide range of overall lamella density. Since the viscosity contrast is both affecting the matrix A and vector B in Eq. B.4 in the Appendix B, its effect on the pressure field, and thus gas trapping is reduced.

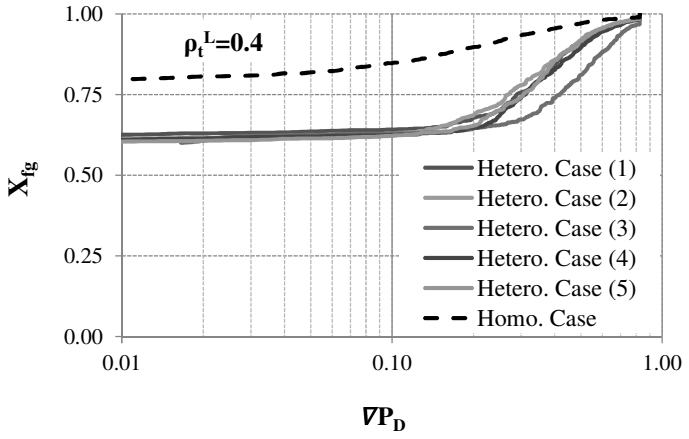

(a)

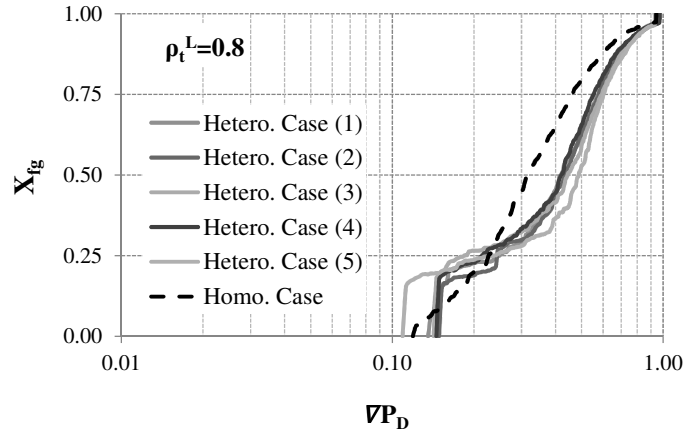

(b)

Figure 4.7 Comparison of the effect of different spatial lamella distributions on flowing gas fraction (X_{fg}) as function of dimensionless pressure gradient (∇P_D) at constant overall lamella densities: (a) $\rho_t^L = 0.4$ and (b) 0.8. The lamella flow equation with the constant viscosity model is used in these simulations. No viscosity contrast between lamella and gas.

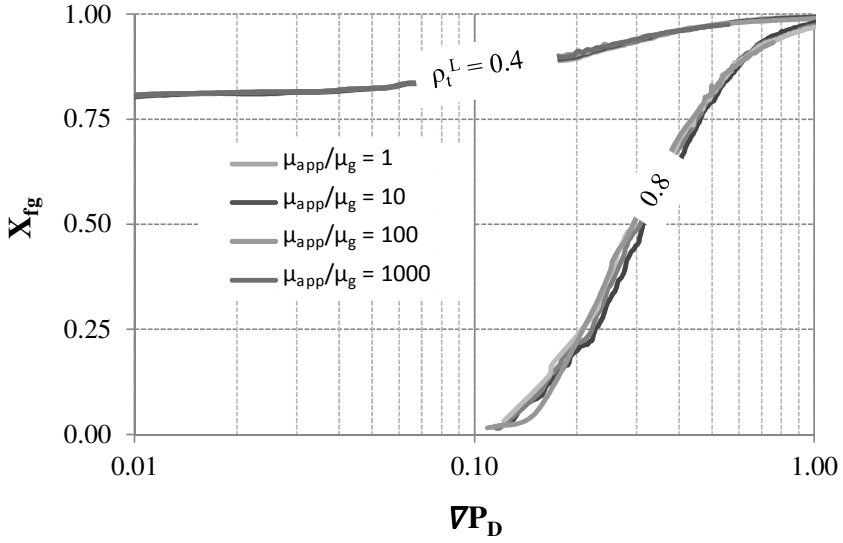

Figure 4.8 Flowing gas fraction (X_{fg}) vs. dimensionless pressure gradient (∇P_D) for different viscosity contrasts between lamella and gas and two overall lamella densities, $\rho_t^L = 0.4$ and 0.8. The legend shows the ratio of pore-scale apparent gas viscosity (μ_{app}) to ordinary gas viscosity (μ_g) at standard conditions. The lamella flow equation with the constant viscosity model is used in these simulations.

The non-Newtonian effect of lamella flow on gas trapping is evaluated through the power-law and Hirasaki-Lawson viscosity models and the results are shown in Figure 4.9. It is obvious from this figure that the variation of rheological behavior from Newtonian to shear thinning does not influence the flowing gas fraction over a wide range of overall lamella density.

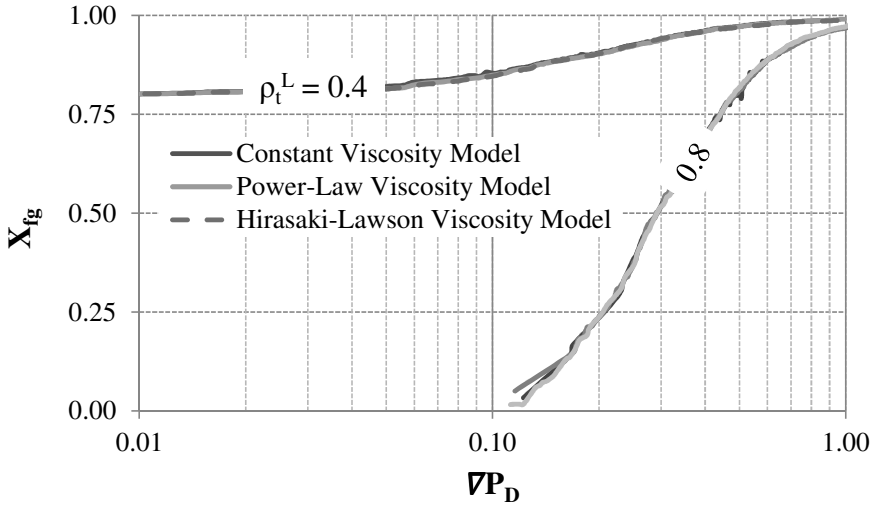

Figure 4.9 Flowing gas fraction (X_{fg}) vs. dimensionless pressure gradient (∇P_D) for the lamella flow equation with the constant, power-law, and Hirasaki-Lawson viscosity models for two different overall lamella densities, $\rho_t^L = 0.4$ and 0.8.

4.2.2 Effective Gas Viscosity

To distinguish the contribution of effective gas viscosity (μ_g^f) from that of gas relative permeability to foam mobility, the effective viscosity is evaluated at sufficiently high pressure gradient such that all lamellas in the network are mobilized. For simplicity, the lamella flow equation with the constant viscosity model is chosen to perform this evaluation whose result is shown in Figure 4.10. In this simulation, the ratio μ_{app}/μ_g is set to 100. The effective gas viscosity normalized to the ordinary gas viscosity increases exponentially with flowing lamella density (ρ_{fg}^L). A sharp increase in the effective gas viscosity as ρ_{fg}^L approaches 0.65 is due to the change of foam regime from continuous-gas to discontinuous-gas foam when ρ_{fg}^L is around 0.65. This finding is striking as it indicates much higher sensitivity of effective gas viscosity to flowing lamella density in porous media than the Hirasaki-Lawson based foam viscosity model commonly used in all population balance based approaches where effective gas viscosity is proportional to

flowing lamella density (Eq. 2.9 in Chapter 2). This implies that volume averaging of the pore-scale apparent gas viscosity should reflect the characteristics that could not be captured by a bundle of capillary tubes model. Another important implication of this result is that the kinetics of gas trapping and remobilization is more influenced by the lamella density contrast between the flowing and trapped gas domains. Our result above shows that this contrast could be significant (Figure 4.5b), making the assumption that flowing and trapped lamella densities are equal, which was employed in several population balance models (Kovscek et al., 1995, 1997), problematic.

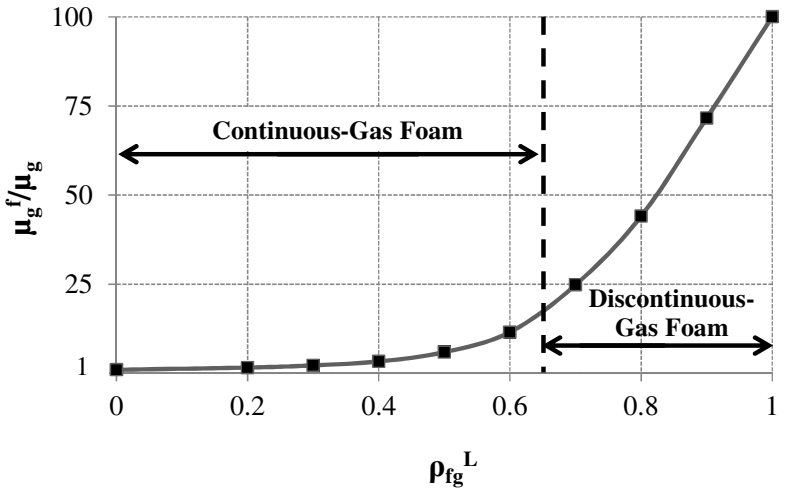

Figure 4.10 Normalized effective gas viscosity (μ_g^f/μ_g) as a function of flowing lamella density (ρ_{fg}^L) for a high pressure gradient (all pores are open). The lamella flow equation with the constant viscosity model is used in these simulations with $\mu_{app}/\mu_g = 100$.

Furthermore, when the exchange of lamella between the trapped and flowing gas domains occurs, spatial redistribution of lamella may modify the effective gas viscosity. To verify this effect, several simulations with different realizations of lamella distribution are performed. The results shown in Figure 4.11 confirm that the effective gas viscosity is

poorly sensitive to the spatial distribution of lamella for a wide range of flowing lamella density in the pore network.

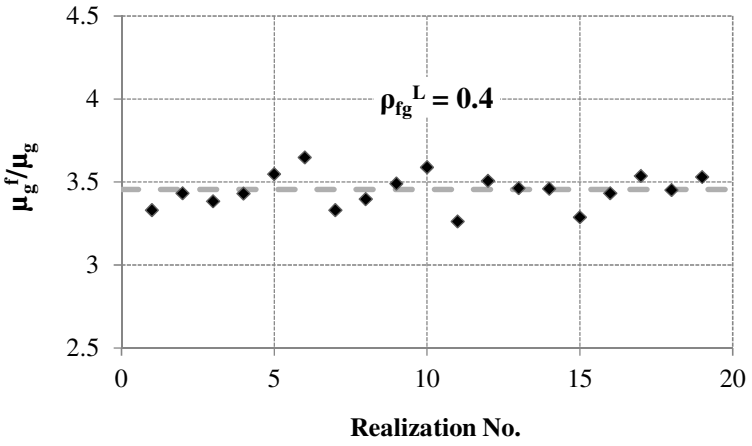

(a)

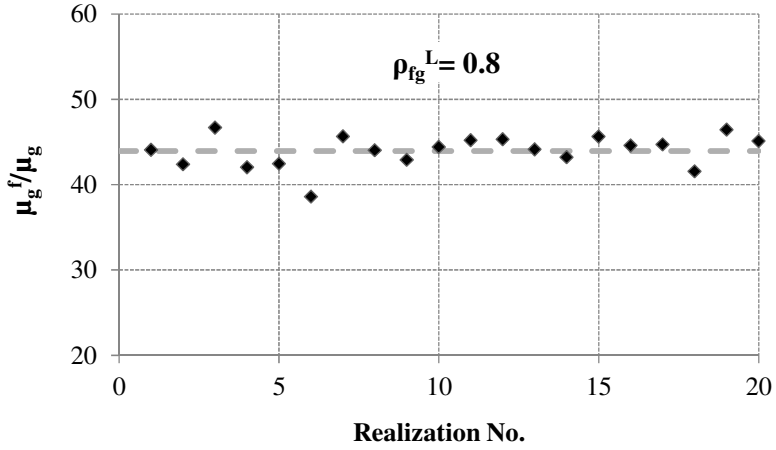

(b)

Figure 4.11 Influence of different spatial lamella distribution on normalized effective gas viscosity (μ_g^f/μ_g) for two flowing lamella densities (a) ρ_{fg}^{L} = 0.4 and (b) 0.8. All pores are open to flow. The lamella flow equation with the constant viscosity model is used in these simulations with μ_{app}/μ_g = 100.

The effect of pore-scale shear thinning behavior of flowing lamellas on the effective gas viscosity could be quantified using the Hirasaki-Lawson viscosity model. In this model (Table 4.1), pore-scale apparent gas viscosity, μ_{app} scales with $(N_c)^{-1/3}$, where N_c is the capillary number defined by Eq. 4.5.

$$N_c = \frac{\mu_w v_g^f}{\gamma} \tag{4.5}$$

The resulting normalized effective gas viscosity as a function of N_c are given for different flowing lamella densities, ρ_{fg}^{L} in Figure 4.12a. Effective gas viscosity decreases with increasing capillary number, which is the characteristic flow behavior of shear-thinning fluids. Moreover, effective gas viscosity increases non-linearly with flowing lamella density at a constant N_c (Figure 4.12b). Comparing Figures 4.10 and 4.12b reveals that the fluid types do not modify the nonlinear relationship between flowing lamella density and effective gas viscosity. Furthermore, the normalized effective gas viscosity increases with permeability at a constant capillary number (Figure 4.13) , which is consistent with the relationship between Hirasaki-Lawson pore-scale apparent gas viscosity, μ_{app} and pore-throat radius R in Table 4.1.

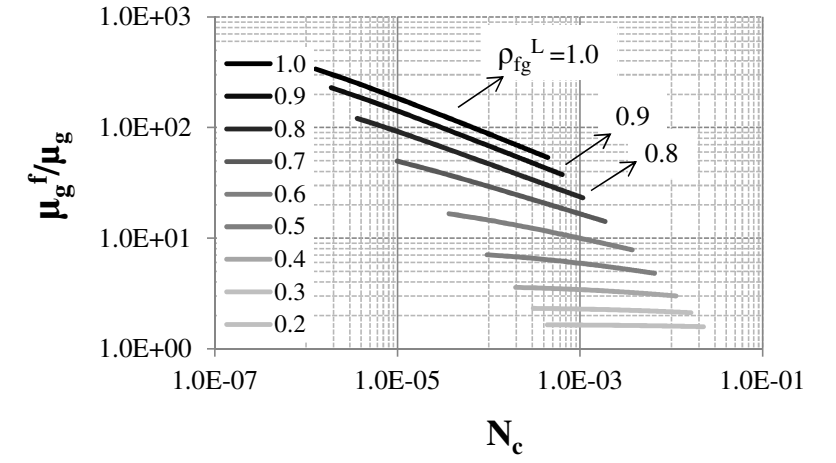

(a)

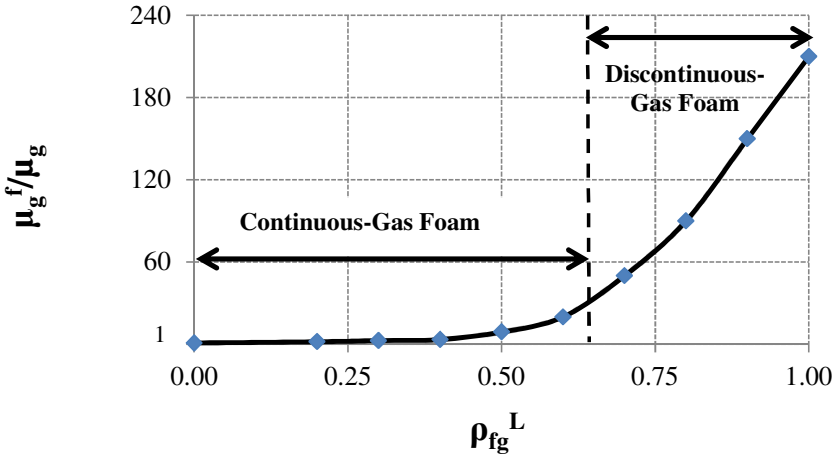

(b)

Figure 4.12 (a) Normalized effective gas viscosity (μ_g^f/μ_g) as a function of capillary number (N_c) for different flowing lamella densities (ρ_{fg}^L). (b) Normalized effective gas viscosity (μ_g^f/μ_g) as a function of flowing lamella density (ρ_{fg}^L) at a constant capillary number (N_c) of 1.0×10^{-5} based on the Hirasaki-Lawson viscosity model. All the pores are open to flow

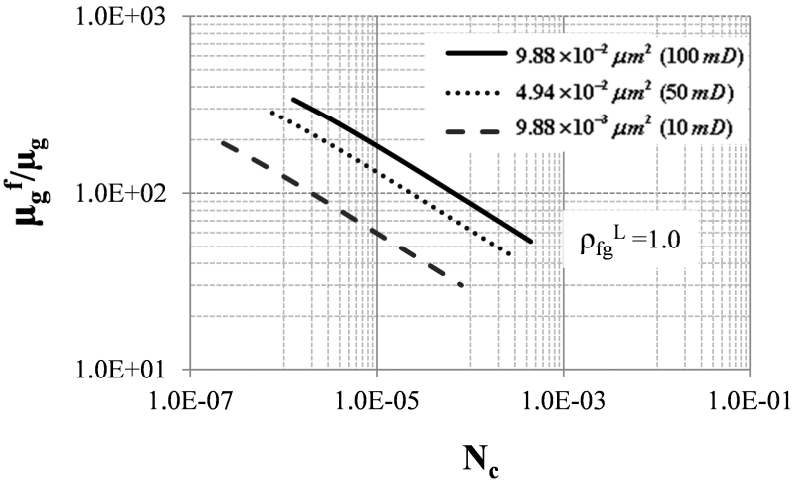

Figure 4.13 Normalized effective gas viscosity (μ_g^f/μ_g) as a function of capillary number (N_c) for different permeabilities at a flowing lamella density (ρ_{fg}^L) of 1.0 based on the lamella flow equation with the Hirasaki-Lawson viscosity model. All the pores are open to flow.

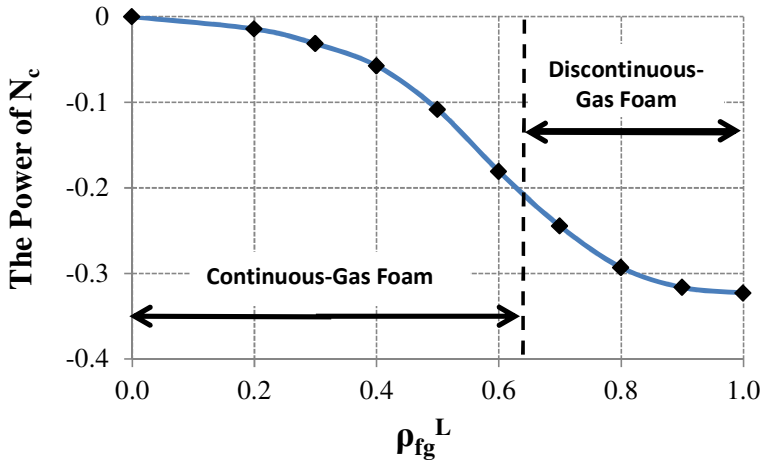

Figure 4.14 The power of capillary number as a function of flowing lamella density (ρ_{fg}^L) based on the lamella flow equation with the Hirasaki-Lawson viscosity model. All the pores are open to flow.

The power of capillary number decreases nonlinearly with increasing flowing lamella density and approaches a constant value of -1/3 for $\rho_{fg}^L > 0.8$ (Figure 4.14),

which is consistent with the scaling of pore-scale apparent gas viscosity, μ_{app} with capillary number. When flowing lamella density is below 0.4, effective gas viscosity is a very weak function of capillary number, so the Newtonian flow behavior becomes more obvious. However, shear thinning of foam flow in straight capillary tubes is expected to be dominant at high flowing lamella density.

4.2.3 Effective Gas Viscosity with Trapped Gas

The nonlinear functional relationship between effective gas viscosity and flowing lamella density (Figure 4.10 and Figure 4.12b) is based on high pressure gradient at which all the pores are open to flow. Since the effect of spatial lamella distribution on effective gas viscosity is almost negligible (Figure 4.11), this relationship is expected to be also valid for foam flow at low pressure gradient. Indeed, Figure 4.15 shows a single trend for effective gas viscosity at both low and high pressure gradients regardless of the presence of trapped gas at low pressure gradient. This is particularly true if flowing lamella density is defined as the number of flowing lamellas divided by the number of pore throats in the flowing gas domain (ρ_{fg}^{L}), while overall lamella density is defined as the total number of lamellas in the pore network divided by the total number of pore throats (ρ_{t}^{L}). Since the flowing gas fraction curve is not influenced by spatial lamella distributions (Figure 4.7), viscosity contrast between lamella and gas (Figure 4.8), and the viscosity models over a wide range of overall lamella density (Figure 4.9), the gas relative permeability curves in Figure 4.4(b) are used to calculate effective gas viscosity at low pressure gradient (in the presence of trapped gas).

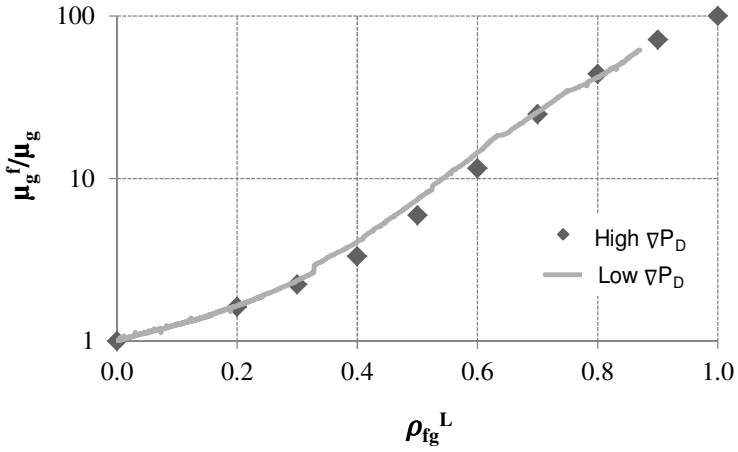

Figure 4.15 Comparison of normalized effective gas viscosity (μ_g^f/μ_g) vs. flowing lamella density (ρ_{fg}^L) at low and high dimensionless pressure gradients (∇P_D). Trapped gas is present at low dimensionless pressure gradient. The lamella flow equation with the constant viscosity model is used in these simulations with $\mu_{app}/\mu_g = 100$.

Even though the use of ρ_{fg}^L allows evaluating separately contribution of relative gas permeability and effective gas viscosity to foam mobility, this specific definition of flowing lamella density may not be convenient for scaling up these two rheological properties of foam flow. One reason is that it is difficult to define the number of pore throats in natural rocks. This may also account for the fact that the existing population balance based foam models (Kovscek et al. 1995, 1997; Kovscek and Bertin, 2003) use an alternate definition of flowing lamella density in terms of the number of flowing lamellas normalized to the flowing gas volume (n_{fg}^L in Table 4.3). Based on our simulations, it is found that these two definitions of flowing lamella density are actually related for the grain pack as shown in Eq.4.6, consistent with Kovscek and Bertin (2003).

$$\rho_{fg}^L \propto n_{fg}^L k^{3/2} \tag{4.6}$$

However, the use of n_{fg}^{L} may cause difficulties in obtaining a universal correlation for effective gas viscosity (Figure 4.15) regardless of gas trapping. This is due primarily to the fact that the number of flowing lamellas may vary proportionally with flowing gas saturation during the dynamic process of lamella trapping and remobilization. As a result, different effective gas viscosity may be observed at a constant n_{fg}^{L}. This could be verified by plotting normalized effective gas viscosity versus n_{fg}^{L} for different pressure gradients and overall lamella densities (n_t^{L}) as shown in Figure 4.16. It can be clearly observed from this figure that effective gas viscosity is a function of not only n_{fg}^{L} but also overall lamella density (n_t^{L} defined in Table 4.3).

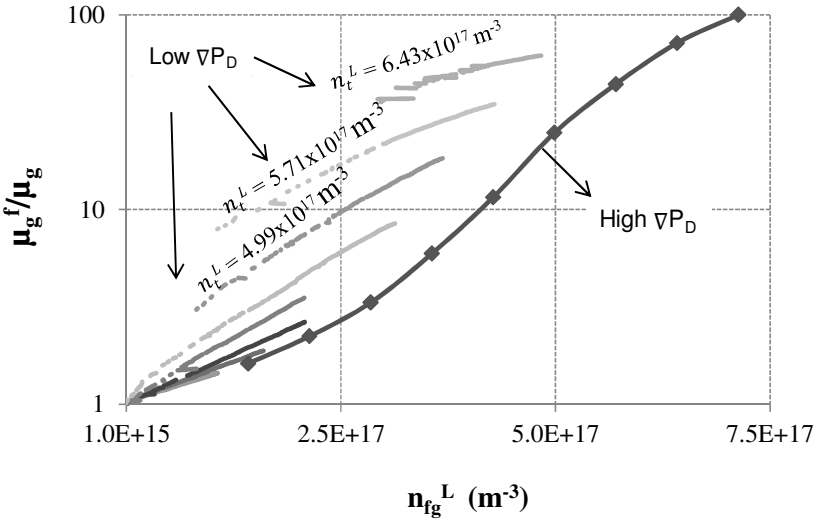

Figure 4.16 Normalized effective gas viscosity (μ_g^f/μ_g) as a function of flowing lamella density (n_{fg}^{L}) (Def. 2 in Table 4.3) at both high and low dimensionless pressure gradients (∇P_D).

4.3 CONCLUSIONS

A 3D pore-network model of computer-generated sphere packs coupled with fluid models that represent a lamella flow through a pore throat has been successfully used to

quantify two key rheological features of foam mobility (i.e. gas relative permeability and effective gas viscosity) and their influencing factors.

Flowing gas fraction increases as the overall lamella density in the pore network decreases at a constant pressure gradient. This results in a significant variation of the threshold pressure gradients at high overall lamella density. Relative gas permeability is a strong non-linear function of flowing gas fraction. This observation disagrees with most of the existing theoretical models for the effect of gas trapping on relative gas permeability in which a linear relationship is commonly assumed. Moreover, the shape of the relative gas permeability curve is poorly sensitive to overall lamella density.

The findings on the dynamics of foam trapping and remobilization indicate that both flowing and trapped lamella densities vary with pressure gradient, but are not necessarily the same. This preliminary result provides insight into the least explored aspect of population balance based modeling approaches, that is the kinetics of gas trapping. It is also relevant to understanding phase trapping during multi-phase flow.

Empirical and mechanistic pore-scale apparent gas viscosity models are evaluated and compared. It is found that all the models give almost the same functional relationship between flowing gas fraction and pressure gradient. This would facilitate scaling of flow rate with pressure gradient and testing a range of shear-thinning and yield-stress behavior in a simple format.

Effective gas viscosity is a strong function of flowing lamella density. The nonlinearity of this function is opposed to the existing foam viscosity models developed for foam flow in porous media and reported here for the first time. In addition, shear thinning foam flow is more obvious at high flowing lamella density while Newtonian flow becomes significant at relatively low flowing lamella density.

Scaling of effective gas viscosity with flowing lamella density depends on how the later quantity is defined. Effective gas viscosity is a unique function of the number of flowing lamellas normalized to the total number of pore throats open to flow. However, it also scales with overall lamella density if the number of flowing lamellas is normalized to the flowing gas volume. This issue has not been addressed in the literature of modeling of foam in porous media because the dynamics of gas trapping and remobilization and its effect on foam mobility has been neglected.

Chapter 5: Development of Analytical Correlations of Flowing Gas Fraction and Effective Gas Viscosity

In chapter 4, two key parameters controlling foam mobility in porous media, which are flowing gas fraction and effective gas viscosity, were quantified as functions of lamella density, pressure gradient and various influencing factors by using a 3D pore-network model of a computer-generated grain pack and representative equations for a lamella flow through a pore throat (Balan et al, 2012). In this chapter, however, the same relations are obtained by using a network model constructed from a real, naturally occurring sandstone (Figure 3.1b in Chapter 3). The aim of this chapter is to obtain dimensionless correlations of flowing gas fraction and effective gas viscosity that are independent of characteristic pore-network properties. These correlations will form the basis for the development of a one-dimensional foam flow model in the upcoming chapter.

5.1 GAS TRAPPING

In previous chapter, it was shown that the relationship between flowing gas fraction and dimensionless pressure gradient is not dependent on the viscosity contrast between lamella and gas, and the viscosity models over a wide range of overall lamella density (Balan et al, 2012). For numerical simplicity the lamella flow equation with the constant viscosity model (Table 4.2 in Chapter 4) is used in here and the apparent gas (lamella) viscosity is equal to regular gas viscosity.

Figure 5.1a shows the relationship between flowing gas fraction (X_{fg}) and dimensionless pressure gradient (∇P_D) for an overall lamella density (ρ_t^L) of 1.0 in the grain pack and the sandstone (Table 3.1 in Chapter 3). Recall that in Figure 3.7a in Chapter 3 the percent pore volume open for sandstone does not reach to 100% at very

high pressure gradients due to presence of the dead-end pores in the network where fluid flow does not occur. In fact, removing these dead-end pores from the network does not change the absolute permeability of sandstone. Therefore, the flowing gas fraction for sandstone in Figure 5.1a is a normalized version of the percent pore volume open in Figure 3.7a. Figure 5.1a shows that the dimensionless threshold pressure gradient, ∇P_T for the sandstone is smaller than that for the grain pack. Moreover, the sandstone requires more (∇P_D -∇P_T) to open all pores in the network than the grain pack does. The physical meaning of these results can only be understood if the pore-throat radius distributions of each pore-network having the same permeability are plotted (Figure 5.1b). Log-normal mean of the pore-throat radius distribution for the sandstone is greater than that for the grain pack. The larger the mean pore-throat radius, the easier the foam flow initiates and therefore, the smaller the ∇P_T. Furthermore, the variance of pore-throat radius for sandstone is greater than that for the grain pack. The higher the variance of pore-throat radius, the more pressure gradient above the threshold pressure gradient (∇P_D -∇P_T) is required to open all pores in the network.

Flowing gas fraction vs. dimensionless pressure gradient is plotted for different overall lamella densities for the grain pack and the sandstone in Figure 5.2. Although it seems that X_{fg} curves for the sandstone are different than those for the grain pack, there are some important similarities between them needed to be highlighted. For both networks X_{fg} increases with decreasing ρ_t^L at a fixed ∇P_D. Therefore, it is easier to open flow paths at lower ρ_t^L. Moreover, ∇P_T for both networks increases with ρ_t^L if ρ_t^L is above 0.65.

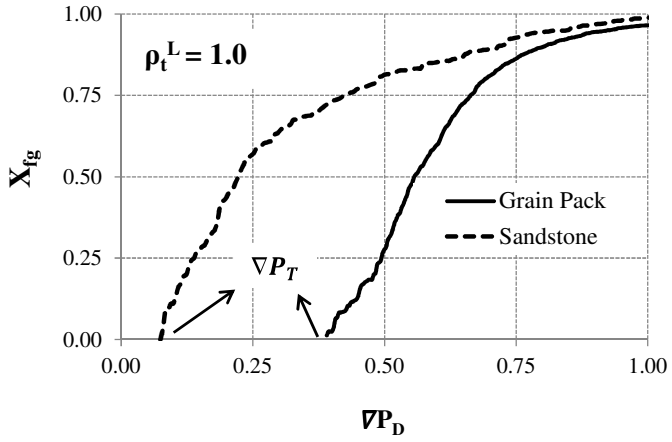

(a)

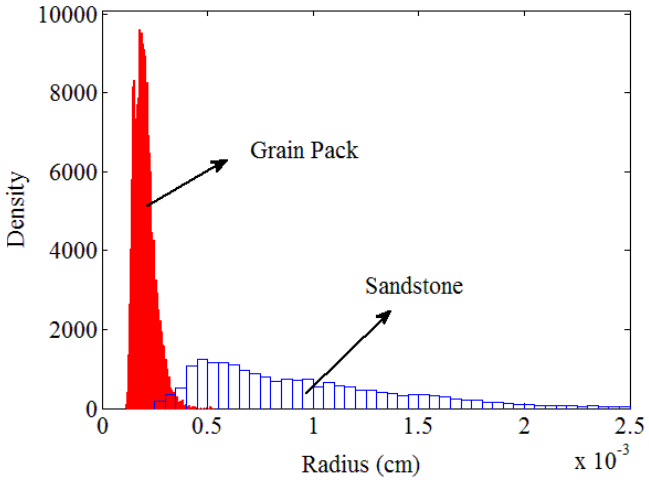

(b)

Figure 5.1 (a) Flowing gas fraction (X_{fg}) vs. dimensionless pressure gradient (∇P_D) for an overall lamella density (ρ_t^L) of 1.0 in the grain pack and the sandstone. (b) Pore-throat radius distribution for the grain pack and the sandstone having a permeability of 9.88×10^{-10} cm^2 (100mD).

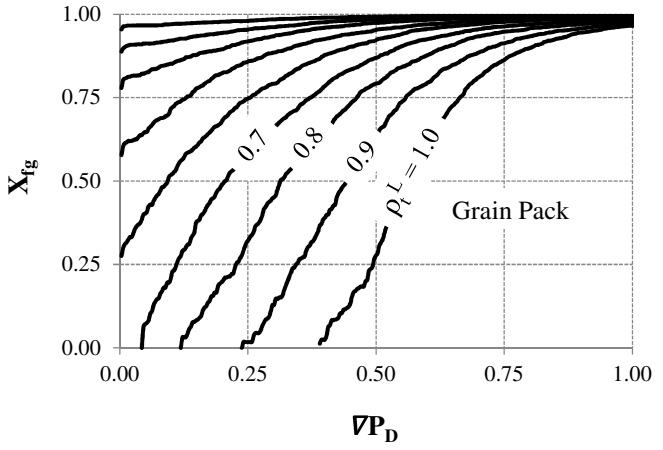

(a)

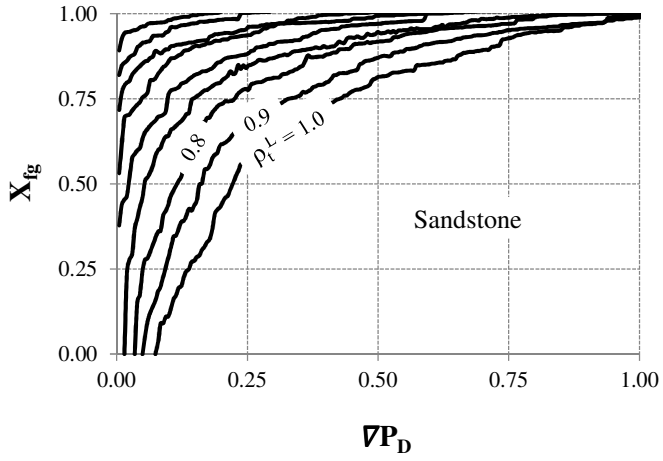

(b)

Figure 5.2 Flowing gas fraction (X_{fg}) vs. dimensionless pressure gradient (∇P_D) for different overall lamella densities (ρ_t^L) in (a) the grain pack and (b) the sandstone.

It is important to note that the definition of the ∇P_D (Eq. 5.1) does not include the log-normal mean and variance of the pore-throat radius distribution for each network. This explains why X_{fg} curves for sandstone and grain pack look different in Figure 5.2.

$$\nabla P_D = \frac{\nabla P}{(2\gamma / L_c)} \sqrt{\frac{2k}{\phi}} \tag{5.1}$$

Therefore, including the characteristic pore-network parameters into the definition of dimensionless pressure gradient would generate X_{fg} curves independent of the pore-network type. For this purpose the following dimensionless pressure gradient $(\nabla P_D)_A$ is proposed:

$$(\nabla P_D)_A = \frac{\nabla P}{(2\gamma / L_c)} \sqrt{\frac{2(\bar{R})^2}{\phi}} \frac{\bar{R}}{\sigma_R} \tag{5.2}$$

Where $\bar{R}$ and σ_R are log-normal mean and standard deviation of the pore-throat radius distribution for a pore-network. The permeability term in Eq. 5.1 is replaced by $\bar{R}^2$ in Eq. 5.2. Moreover, the ratio of $(\bar{R}/\sigma_R)$ is included as a multiplier (Eq. 5.2).

Plotting X_{fg} as a function of $(\nabla P_D)_A$ instead of ∇P_D overlaps the dimensionless threshold pressure gradients $(\nabla P_T)_A$ for the grain pack and the sandstone for the overall lamella densities, ρ_t^L above 0.65 (Figure 5.3). Moreover, there exists a linear relationship between $(\nabla P_T)_A$ and ρ_t^L, which is independent of the pore-network type (Figure 5.4).

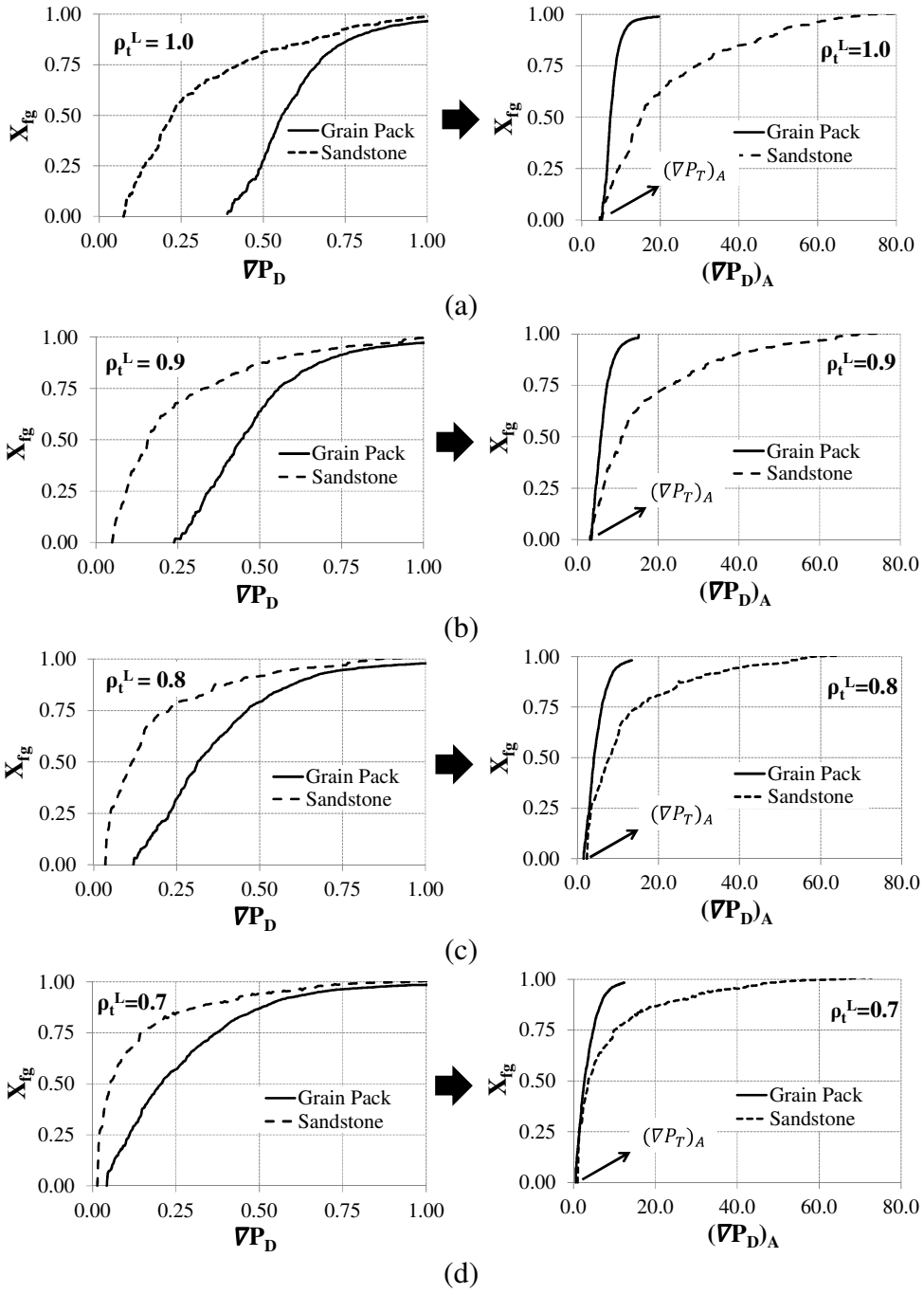

Figure 5.3 Plotting flowing gas fraction (X_{fg}) as a function of $(\nabla P_D)_A$ instead of (∇P_D) overlaps the dimensionless threshold pressure gradients $(\nabla P_T)_A$ for the grain pack and the sandstone for different overall lamella densities (ρ_t^L) in the discontinuous-gas foam flow regime: (a) ρ_t^L =1.0, (b) 0.9, (c) 0.8, and (d)0.7.

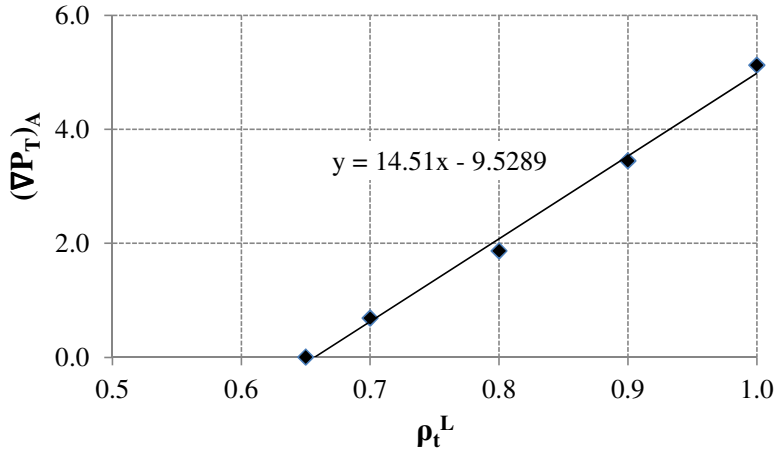

Figure 5.4 The linear relationship between the dimensionless threshold pressure gradient $(\nabla P_T)_A$ and overall lamella density (ρ_t^L),which is independent of pore-network type.

Figure 5.3 shows that the sandstone requires more $(\nabla P_D)_A$ to open all the pores than the grain pack does, which results from the differences in the variance of pore-throat radius distribution $(\sigma_R)^2$ for each pore-network. $(\nabla P_D)_A$ has already a multiplier, which is $(1/\sigma_R)$, to represent standard deviation of the pore-throat radius distribution (σ_R) (Eq. 5.2), so the following modification on $(\nabla P_D)_A$ is proposed :

$$\left(\nabla P_D\right)_B = \left[\left(\nabla P_D\right)_A - \left(\nabla P_T\right)_A\right]\left(\frac{\sqrt{k}}{\sigma_R}\right)^{f_1} \tag{5.3}$$

Where f_1 is a matching parameter, which is defined as a function of ρ_t^L in Figure 5.5, to overlap X_{fg} curves for the sandstone and the grain pack at different ρ_t^L (Figures 5.6 and 5.7). Moreover, the two distinct foam flow regimes, which are continuous-gas ($\rho_t^L <$ 0.65) and discontinuous-gas ($\rho_t^L >$ 0.65) foam, can easily be identified in Figure 5.5. f_1 has a constant value of 0.35, if ($\rho_t^L <$ 0.65) and it is an increasing linear function of ρ_t^L, if ($\rho_t^L >$ 0.65).

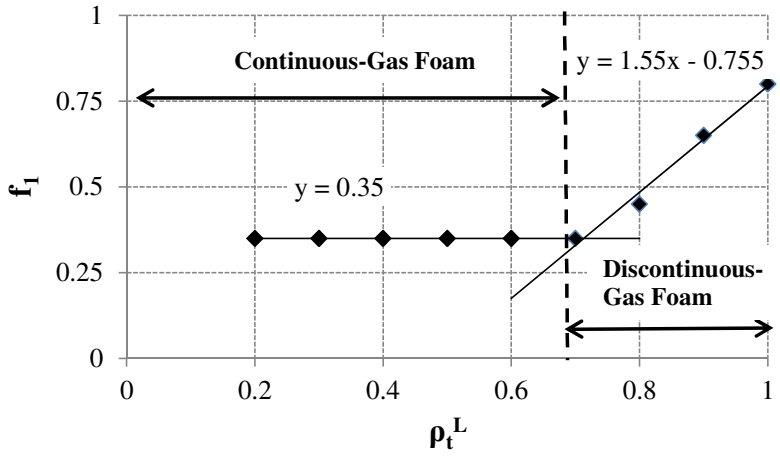

Figure 5.5 The matching parameter f_1 as a function of overall lamella density (ρ_t^L).

In Figures 5.6 and 5.7, the cumulative log-normal distribution function (Eq. .5.4) is successfully matched with the X_{fg} curves for different overall lamella densities. To improve these matches 0.35 is added to the values of the $(\nabla P_D)_B$ in Eq. 5.4a.

$$\left(\nabla P_D\right)_{B'} = \left(\nabla P_D\right)_B + 0.35 \tag{5.4a}$$

$$X_{fg} = \frac{1}{2}\left[erfc\left(\frac{x_1 - \ln\left[\left(\nabla P_D\right)_{B'}\right]}{x_2\sqrt{2}} \right) \right] \tag{5.4b}$$

The matching parameters x_1 and x_2 are defined as a function of overall lamella density, ρ_t^L in Figure 5.8.

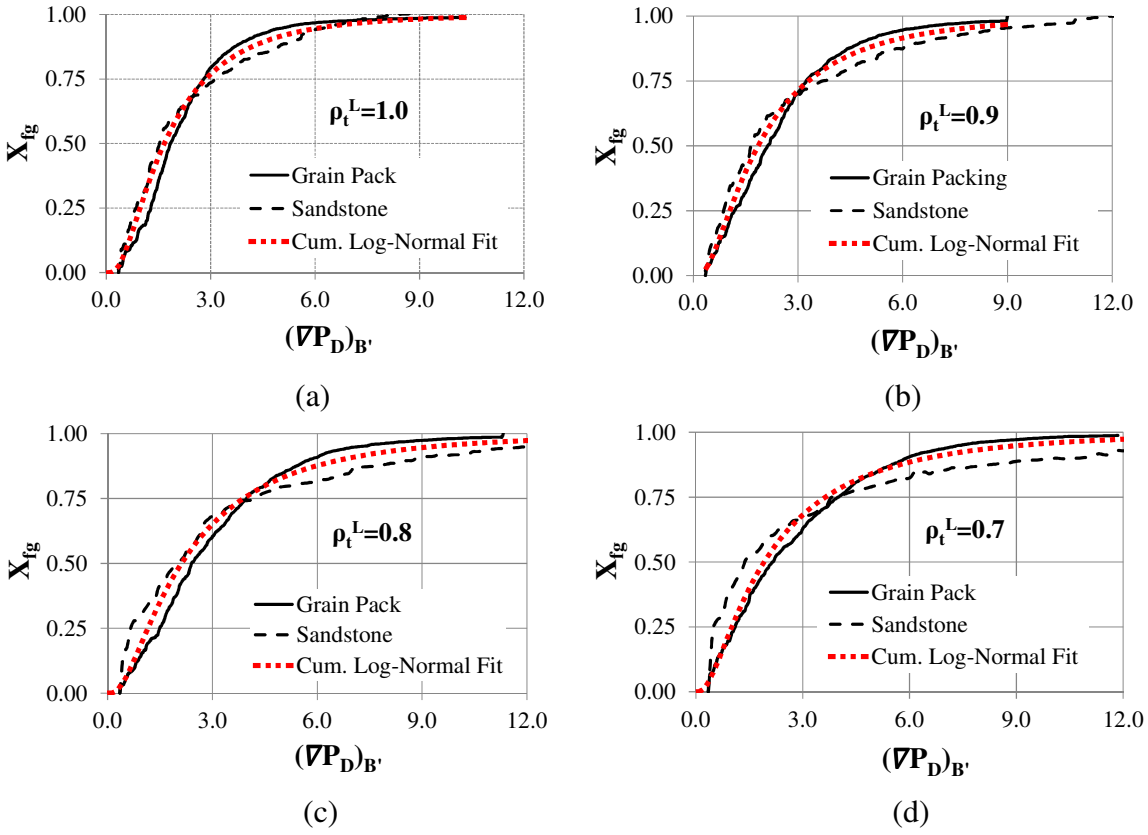

Figure 5.6 Plotting flowing gas fraction (X_{fg}) as a function of $(\nabla P_D)_{B'}$ overlaps X_{fg} curves for the grain pack and the sandstone for different overall lamella densities (ρ_t^L) in the discontinuous-gas foam flow regime: (a) ρ_t^L=1.0, (b) 0.9, (c) 0.8, and (d)0.7. Moreover, cumulative log-normal distribution functions are successfully fitted to these curves.

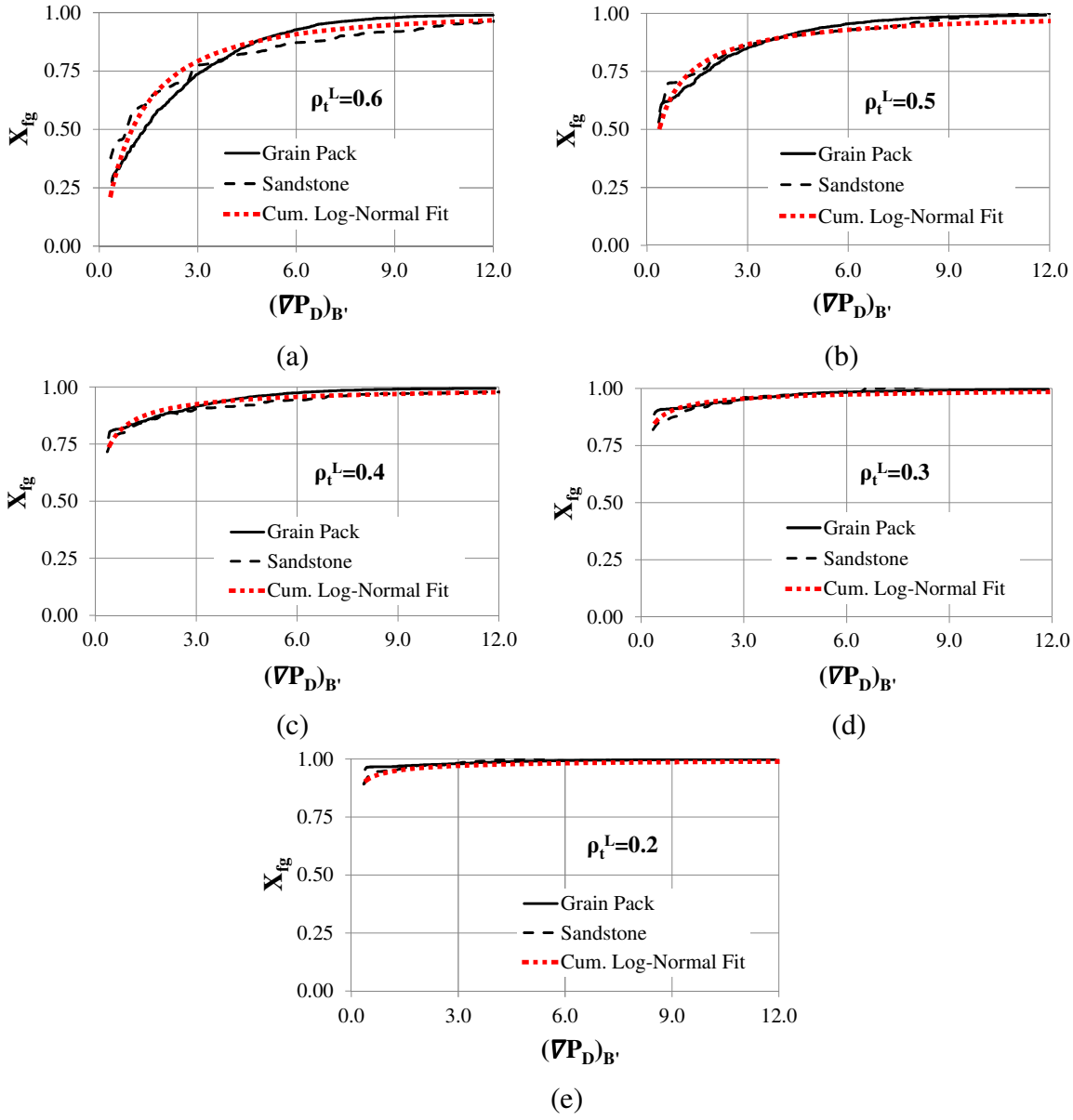

Figure 5.7 Plotting flowing gas fraction (X_{fg}) as a function of $(\nabla P_D)_{B'}$ overlaps X_{fg} curves for the grain pack and the sandstone for different overall lamella densities (ρ_t^L) in the continuous-gas foam flow regime(a) ρ_t^L=0.6, (b) 0.5, (c) 0.4, (d) 0.3, and e) 0.2. Moreover, cumulative log-normal distribution functions are successfully fitted to these curves.

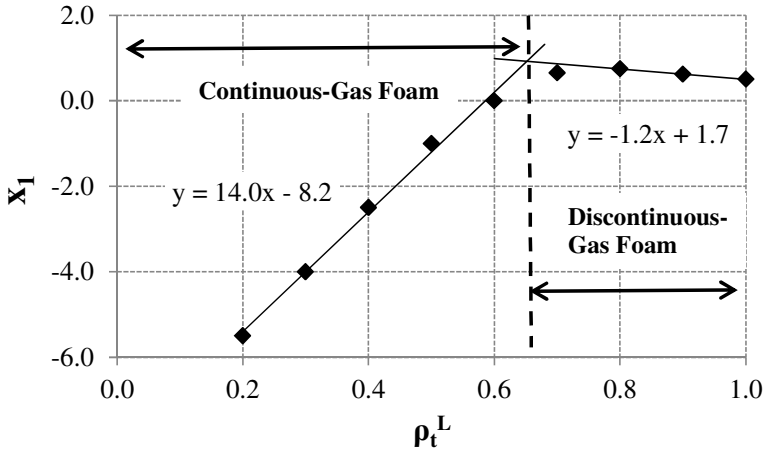

(a)

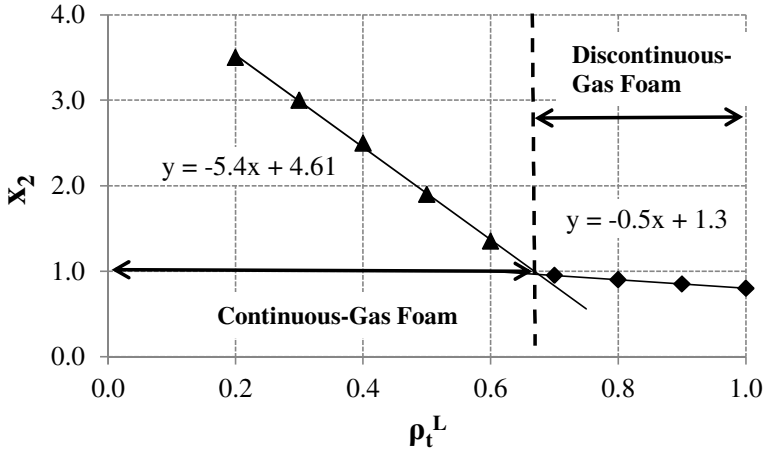

(b)

Figure 5.8 The matching parameters x_1 and x_2 as a function of overall lamella density (ρ_t^L).

5.2 FLOWING LAMELLA DENSITY

The flowing lamella density (ρ_{fg}^L) increases with overall lamella density (ρ_t^L) in the grain pack at a constant pressure gradient (Balan et al, 2012). In Figure 5.9, flowing lamella density is plotted as a function of dimensionless pressure gradient (∇P_D) for different overall lamella densities (ρ_t^L) in the grain pack and the sandstone. ρ_{fg}^L in both networks converges to ρ_t^L as the ∇P_D increases to open all pores. No data for ρ_{fg}^L is

plotted below threshold pressure gradients in Figure 5.9, since foamed-gas is not flowing (Figure 5.2).

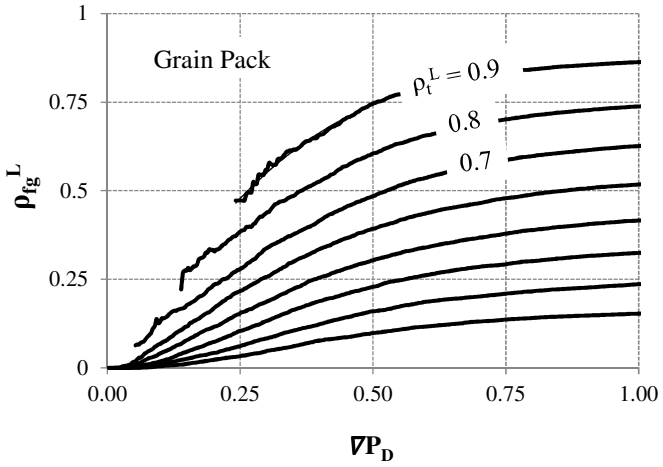

(a)

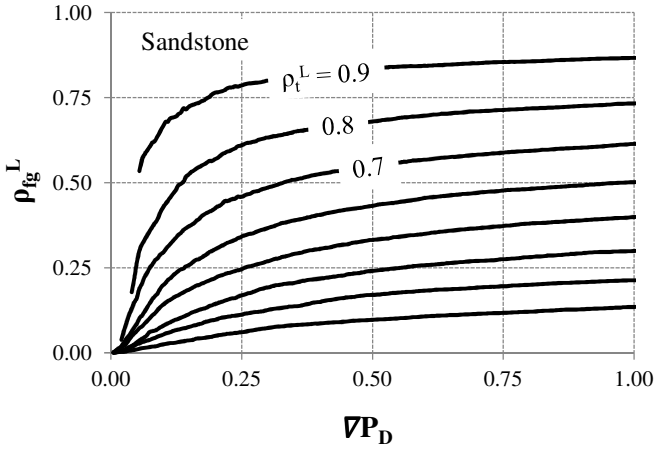

(b)

Figure 5.9 Flowing lamella density (ρ_{fg}^L) vs. dimensionless pressure gradient (∇P_D) for different overall lamella densities (ρ_t^L) in (a) the grain pack and (b) the sandstone.

A new dimensionless pressure gradient $(\nabla P_D)_C$ in Eq. 5.5, which is very similar to $(\nabla P_D)_B$ in Eq. 5.3, is used here to overlap ρ_{fg}^{L} curves for the sandstone and the grain pack as a function of ρ_t^{L} (Figures 5.10, 5.11 and 5.12)

$$\left(\nabla P_D\right)_C = \left[\left(\nabla P_D\right)_A - \left(\nabla P_T\right)_A\right]\left(\frac{\sqrt{k}}{\sigma_R}\right)^{f_2} \tag{5.5}$$

Finally, the cumulative log-normal distribution functions multiplied by overall lamella density (Eq. 5.6) are fitted to the overlapped flowing lamella density curves in Figures 5.11 and 5.12.

$$\left(\nabla P_D\right)_{C'} = \left(\nabla P_D\right)_C + 0.35 \tag{5.6a}$$

$$\rho_{fg}^{L} = \left(\rho_t^{L}\right)\frac{1}{2}\left[erfc\left(\frac{y_1 - \ln\left[\left(\nabla P_D\right)_{C'}\right]}{y_2\sqrt{2}}\right)\right] \tag{5.6b}$$

Where the matching parameters y_1 and y_2 are plotted as a function of overall lamella density, ρ_t^{L} in Figure 5.13.

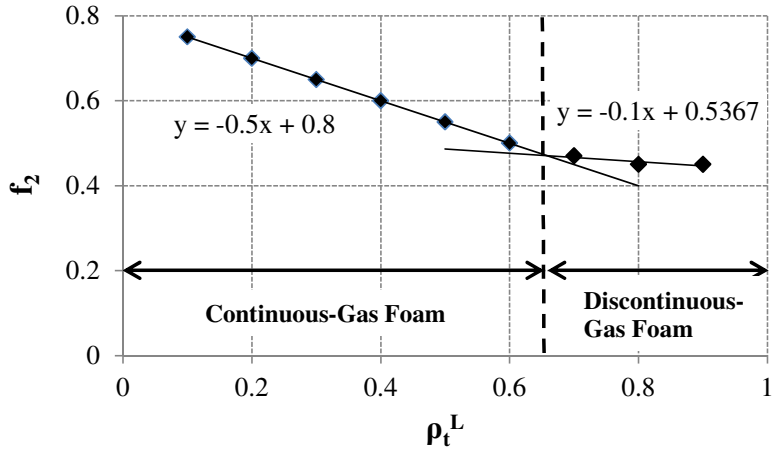

Figure 5.10 The matching parameter f_2 as a function of overall lamella density (ρ_t^{L}).

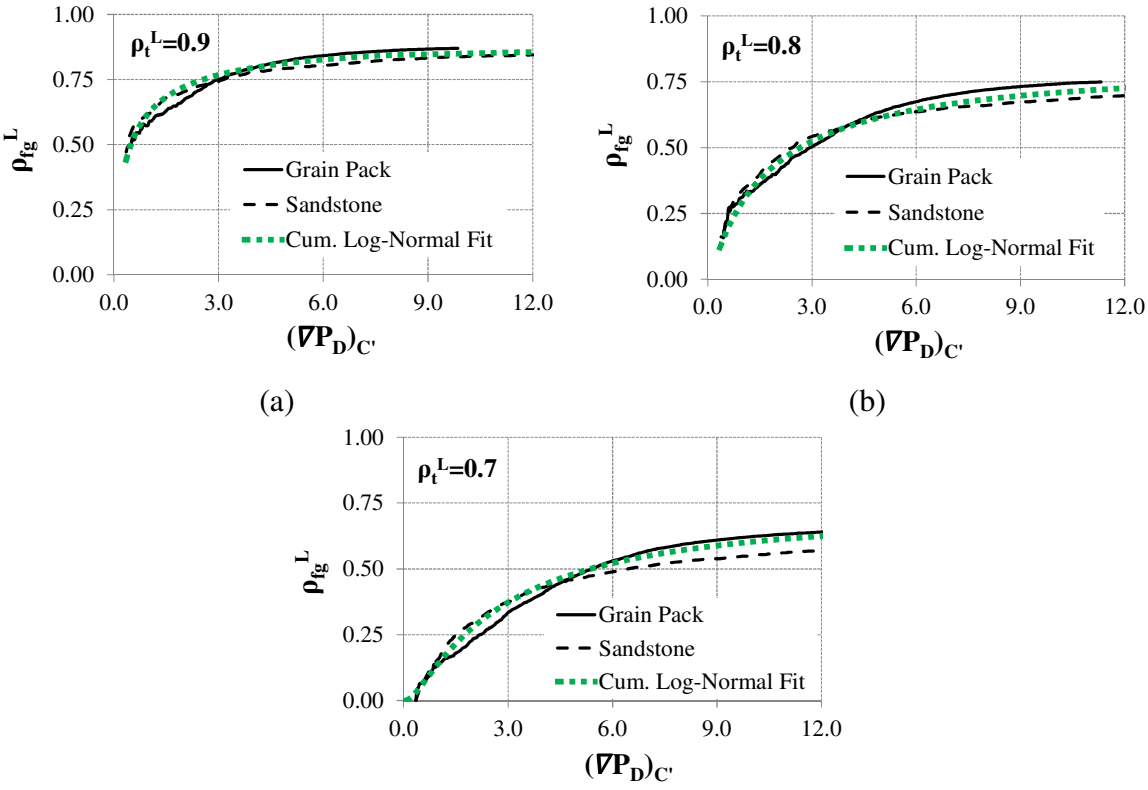

Figure 5.11 Plotting flowing lamella density (ρ_{fg}^{L}) as a function of $(\nabla P_D)_{C'}$ overlaps ρ_{fg}^{L} curves for the grain pack and the sandstone for different overall lamella densities (ρ_t^{L}) in the discontinuous-gas foam flow regime (a) ρ_t^{L}=0.9, (b) 0.8, and (c) 0.7. Moreover, modified cumulative log-normal distribution functions are successfully fitted to these curves.

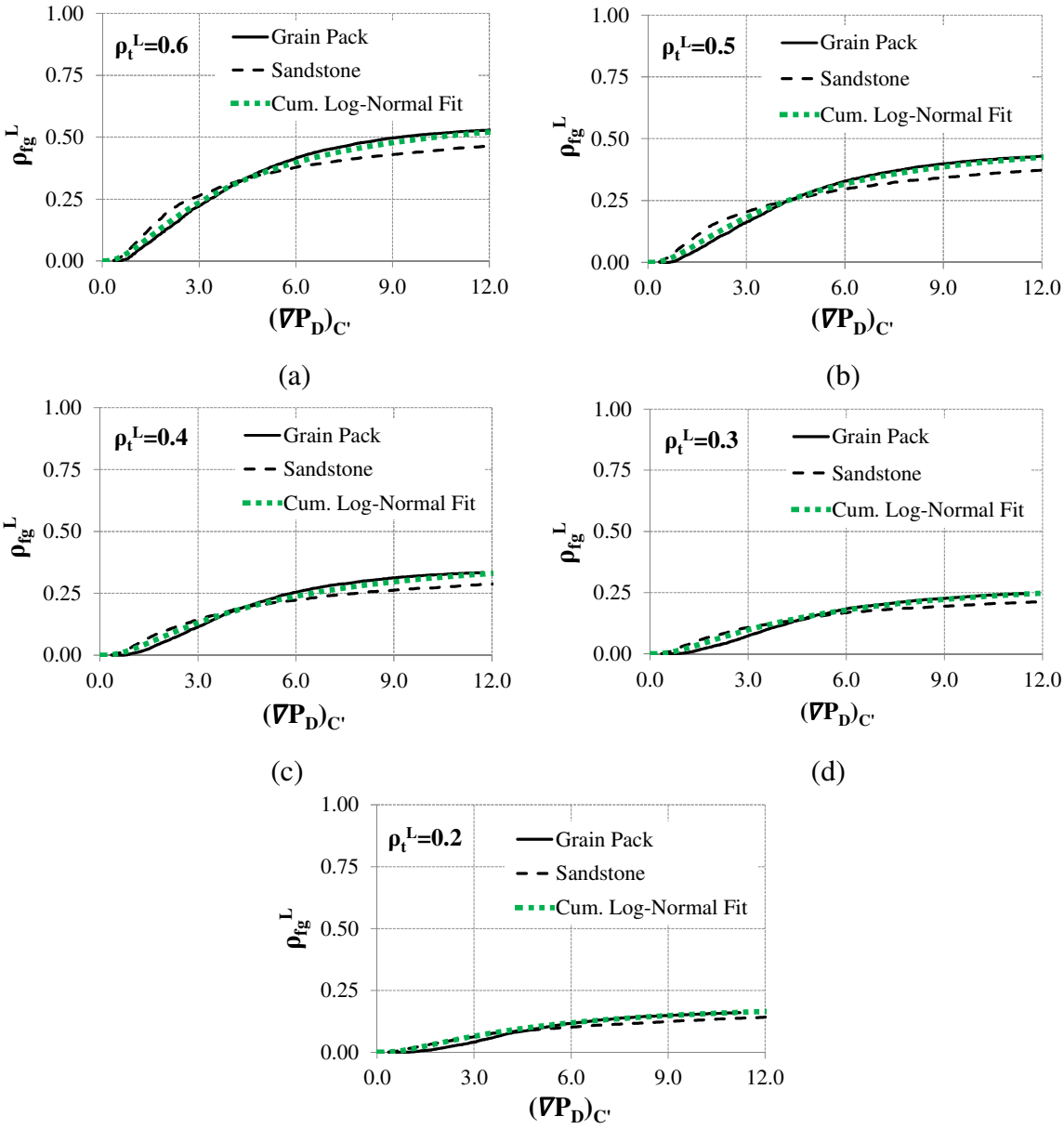

Figure 5.12 Plotting flowing lamella density ($\rho_{fg}{}^{L}$) as a function of $(\nabla P_D)_{C'}$ overlaps $\rho_{fg}{}^{L}$ curves for the grain pack and the sandstone for different overall lamella densities ($\rho_t{}^{L}$) in the continuous-gas foam flow regime (a) $\rho_t{}^{L}$=0.6, (b) 0.5, (c) 0.4, (d)0.3, and e) 0.2. Moreover, modified cumulative log-normal distribution functions are successfully fitted to these curves.

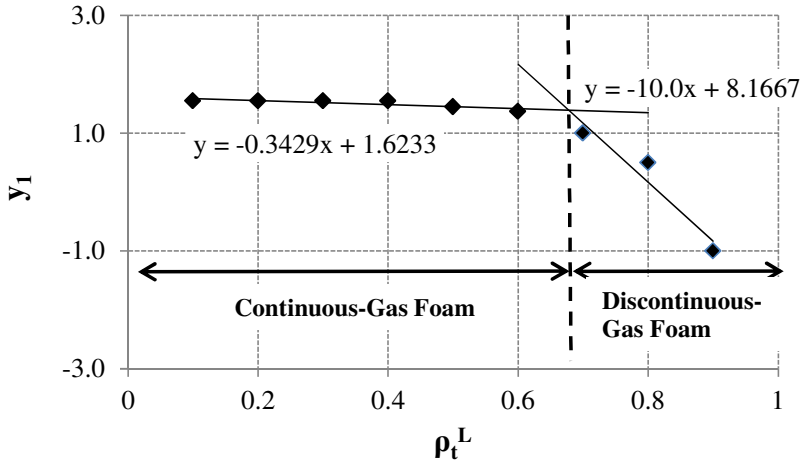

(a)

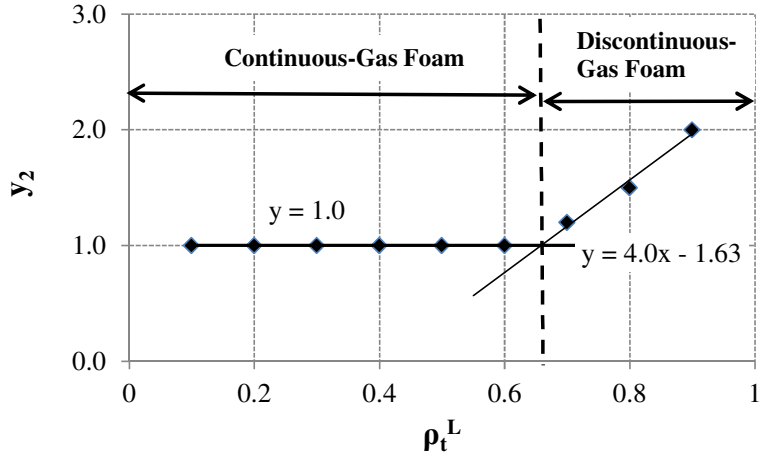

(b)

Figure 5.13 The matching parameters y_1 and y_2 as a function of overall lamella density (ρ_t^L).

5.3 EFFECTIVE GAS VISCOSITY

The effect of pore-scale shear thinning behavior of flowing lamellas on the effective gas viscosity (μ_g^f) could be quantified using the Hirasaki-Lawson apparent gas viscosity (μ_{app}) model (Hirasaki and Lawson, 1985):

$$\mu_{app} = 0.85 \frac{\mu_w (R/L)}{(r_c/R)} \left(\frac{\gamma}{3\mu_w v_g^f} \right)^{1/3} \left[\left(\frac{r_c}{R} \right)^2 + 1 \right] \tag{5.7}$$

If foamed-gas is strong enough to reduce gas mobility in porous media, the radius of curvature of a lamella (r_c) is much smaller than the characteristic pore-throat radius (R), therefore the ratio (r_c/R) is negligible:

$$\mu_{app} = 0.85 \frac{\mu_w (R/L)}{(r_c/R)} \left(\frac{3\mu_w v_g^f}{\gamma} \right)^{-1/3} \tag{5.8}$$

If the logarithm of the both sides of the Eq. 5.8 is taken:

$$\log_{10}(\mu_{app}) = -\frac{1}{3} \log_{10} \left(\frac{3\mu_w v_g^f}{\gamma} \right) + \log_{10} \left(0.85 \frac{\mu_w (R/L)}{(r_c/R)} \right) \tag{5.9}$$

The capillary number is defined as:

$$N_c = \frac{\mu_w v_g^{\ f}}{\gamma} \tag{5.10}$$

Based on pore-level Hirasaki-Lawson apparent gas viscosity model (Eq. 5.9), the following equation is proposed for effective gas viscosity:

$$\log_{10}(\mu_g^f) = \left(a \times \log_{10}(N_c) + b \right) \tag{5.11}$$

If the flowing lamella density (ρ_{fg}^{L}) is equal to 1.0, i.e. there is one lamella in every pore-throat in the flowing gas domain, then the parameter *a* in Eq. 5.11 should be equal to -1/3 (Eq. 5.9) and the parameter b scales by:

$$b \propto \log_{10}\left(\frac{\sqrt{k}P_c}{\gamma}\right) \tag{5.12}$$

Capillary pressure is defined as:

$$P_c = \frac{2\gamma}{r_c} \tag{5.13}$$

If ρ_{fg}^{L} is smaller than 1.0, i.e. some fraction of pore-throats in the flowing gas domain is not occupied by a lamella, then the parameters *a* and *b* in Eq. 5.11 are expected to be a function of flowing lamella density, ρ_{fg}^{L}.

In Figure 5.14, the results of the pore-network study clearly shows that the parameter *a* in Eq. 5.11, which is the power of capillary number (Eq. 5.8 and Eq. 5.10), decreases nonlinearly with increasing flowing lamella density and approaches a constant value of -1/3 for $\rho_{fg}^{L} > 0.8$ regardless of the pore-network type. The analytical correlation between parameter *a* and ρ_{fg}^{L} is given in Eq. 5.14. This result is consistent with the scaling of pore-scale apparent gas viscosity with capillary number. As it was stated in Chapter 4, gas flow through a pore throat without a lamella is represented by the Newtonian flow equation with an assumption that gas compressibility is negligible. When flowing lamella density is below 0.4, effective gas viscosity is a very weak function of capillary number for the grain pack and sandstone, so the Newtonian flow behavior becomes more obvious. However, at high flowing lamella densities shear thinning behavior of foam flow is observed for both networks (Figure 5.14).

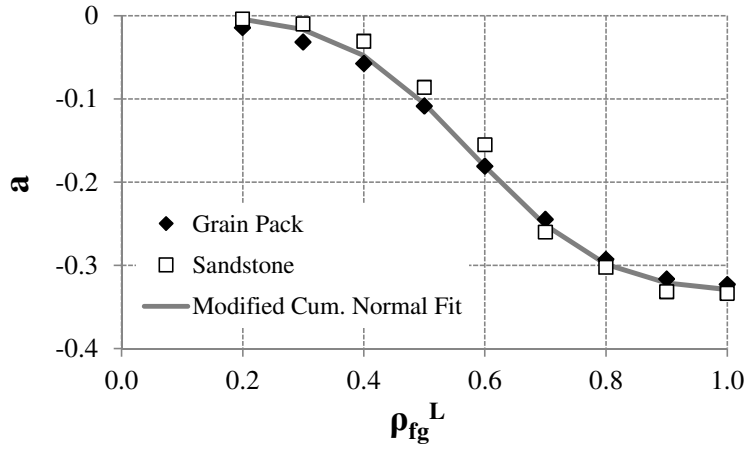

Figure 5.14 The parameter *a* in Eq. 5.11 as a function of flowing lamella density (ρ_{fg}^{L}) in the grain pack and the sandstone. A modified cumulative normal distribution (Eq. 5.14) is fitted to the data.

$$a = -(0.33)\frac{1}{2}\left[erfc\left(\frac{0.58 - \rho_{fg}^{L}}{0.17\sqrt{2}} \right) \right] \tag{5.14}$$

The proposed scaling relation between the parameter *b* and $\log_{10}(k^{0.5}P_c/\gamma)$ in Eq. 5.12 is justified by the pore-network simulation results for different pore-network types, capillary pressures and permeability in Figure 5.15, when the flowing lamella density, ρ_{fg}^{L} is equal to 1.0. The same linear relation is also valid for the flowing lamella densities below 1.0 (Figure 5.16). The linear relationship between the parameter b and $\log_{10}(k^{0.5}P_c/\gamma)$ can be parameterized as:

$$\mathrm{b} = p_1 \log_{10}\left(\frac{\sqrt{k}P_c}{\gamma} \right) + p_2 \tag{5.15}$$

Where the parameters p_1 and p_2 are defined as a function of ρ_{fg}^{L} in Figure 5.17.

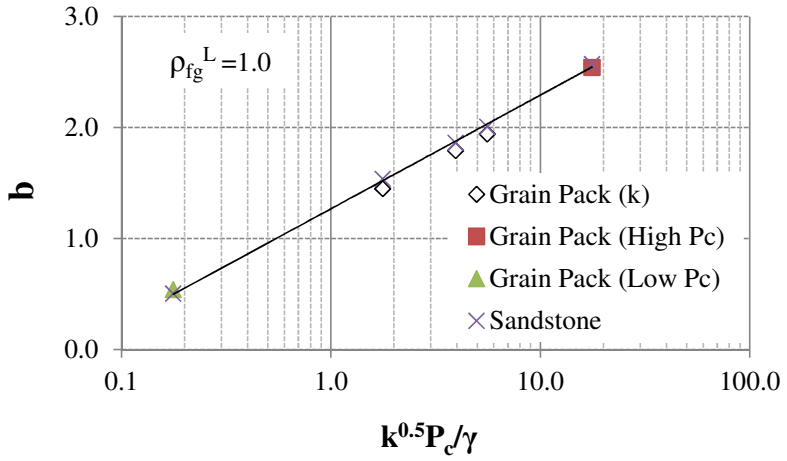

Figure 5.15 Semi-log plot of the parameter *b* vs. the ratio ($k^{0.5}P_c/\gamma$) for a flowing lamella density (ρ_{fg}^{L}) of 1.0 and for different pore-network types, capillary pressures and permeabilities.

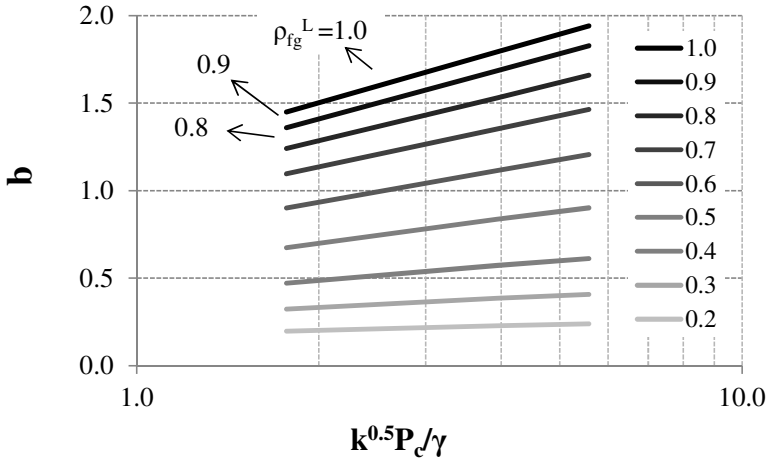

Figure 5.16 Semi-log plot of the parameter *b* vs. the ratio ($k^{0.5}P_c/\gamma$) for different flowing lamella densities (ρ_{fg}^{L}).

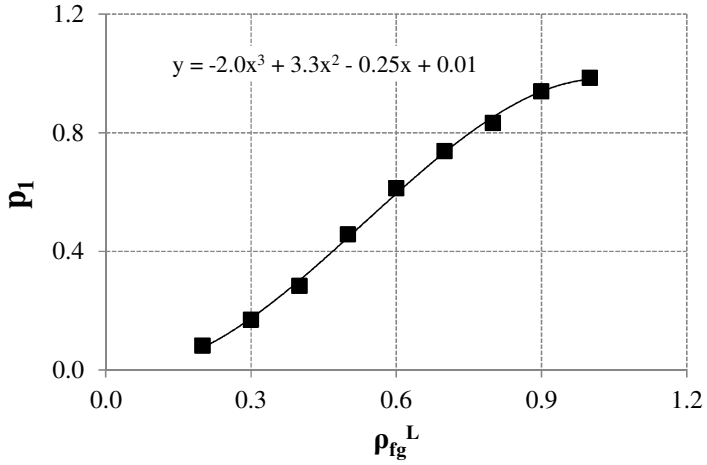

(a)

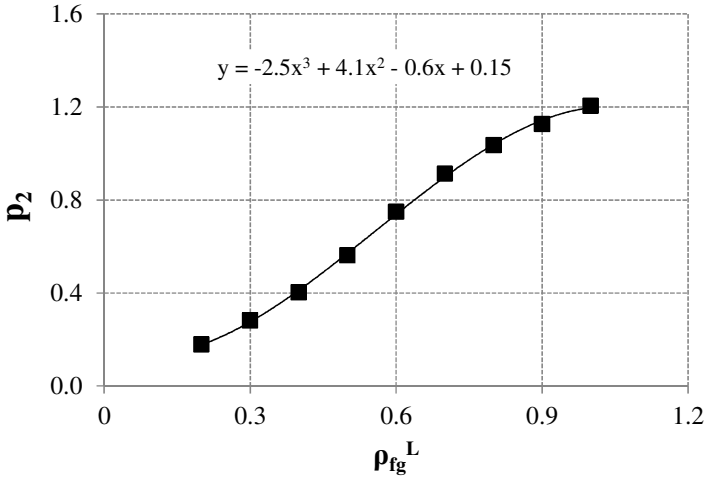

(b)

Figure 5.17 The parameters p_1 and p_2 as a function of flowing lamella density (ρ_{fg}^{L}).

5.4 CONCLUSIONS

In this chapter, characteristic pore-network properties are included into the definition of dimensionless pressure gradient used in previous chapters to obtain analytical correlations of flowing gas fraction and flowing lamella density. These correlations enable one to predict flowing gas fraction and flowing lamella density as functions of overall lamella density and dimensionless pressure gradient regardless of the

pore-network type. Furthermore, it is justified that pore-network type does not affect the scaling relations between the pore-scale Hirasaki-Lawson apparent gas viscosity and effective gas viscosity. In the upcoming chapter a mechanistic foam flow model based on the analytical correlations of flowing gas fraction and effective gas viscosity obtained here will be developed and tested.

Chapter 6: Development of a Mechanistic Foam Model Based on a Continuum Approach

In chapter 5, analytical correlations of flowing gas fraction and effective gas viscosity as functions of lamella density, dimensionless pressure gradient, capillary number, and various rock and fluid properties were obtained to predict foam mobility in porous media. In this chapter, these correlations are used together with a modified lamella population balance model to develop a mechanistic foam model. Furthermore, some synthetic simulation cases are run to discuss one-dimensional (1D) unsteady-state and steady-state flow of foam through porous media. Finally, the simulation results are history matched with core-flood data and discussed. In the following section, the development details of the foam model are provided.

6.1 Foam Model Development

6.1.1 Modified Population Balance Model

6.1.1.1 Calculation of Overall Lamella Density

In this study, local-equilibrium approximation to the full population balance model proposed by Kovscek and Bertin (2003), and Chen et al. (2010) is modified to calculate overall lamella density as a function of various flow parameters. The details of the population balance framework and local-equilibrium approximation were provided in Chapter 2. Based on snap-off mechanism, lamella generation rate (R_g) is defined as (Kovscek et al., 1994a, 1994b, 1995, 1997; Kovscek and Bertin, 2003; Chen et al., 2010):

$$R_g = c_1 v_w \left(v_g^f\right)^{1/3} \tag{6.1a}$$

$$c_1 = c_1^o \left[1 - \left(\frac{n_{fg}^L}{n_{fg}^{L*}}\right)^w\right] \tag{6.1b}$$

Lamella coalescence rate (R_c), which is controlled by capillary suction mechanism, is defined as a function of flowing lamella density (n_{fg}^{L}), interstitial gas velocity with foam (v_g^f) and capillary pressure (P_c) (Kovscek et al.,1993, 1994a, 1994b, 1995, 1997; Kovscek and Bertin, 2003) :

$$R_c = c_{-1} v_g^f n_{fg}^L \tag{6.2a}$$

$$c_{-1}(P_c) = c_{-1}^o \left(\frac{P_c}{P_c^* - P_c} \right)^2 \tag{6.2b}$$

Local-equilibrium approximation states that lamella generation and coalescence rates are in balance during foam flow through porous media. Therefore, flowing lamella density, n_{fg}^{L} can be calculated at a specific flow condition by equating Eq. 6.1a to Eq. 6.2a. In previous population balance based foam models (Kovscek et al., 1995, 1997) it is assumed that flowing lamella density is equal to overall lamella density. In chapter 4, however, it was shown that flowing lamella density changes as functions of overall lamella density and pressure gradient. Therefore, overall lamella density should be known before calculating flowing lamella density. In fact, lamella trapping/mobilization in porous media occurs after lamella generation. In Eq. 6.2b critical capillary pressure (P_c^*) is defined as a constant for a specific porous medium. However, Khatib et al. (1988) showed that P_c^* is a decreasing function of both gas flow rate and permeability of porous media. Based on these findings, the following modification on lamella coalescence rate is proposed:

$$R_c = c_{-1} n_t^L \tag{6.3a}$$

$$c_{-1}(P_c) = c_{-1}^o \left(\frac{P_c}{P_c^*(v_g^f, k) - P_c} \right)^2 \tag{6.3b}$$

The effect of interstitial gas velocity with foam on lamella coalescence rate in Eq. 6.2a is included in the definition of P_c^* in Eq. 6.3b considering the findings of Khatib et al. (1988). This enables one to relate the lamella coalescence rate to overall lamella density (n_t^L) instead of flowing lamella density, n_{fg}^L, because P_c^* is a parameter representing the average value of capillary pressure in porous media (not only in flowing gas domain but also in trapped gas domain) at which lamella coalescence mechanism dominates the flow.

Recall that in Chapter 4 flowing gas fraction and effective gas viscosity were defined as a function of the first definition of overall lamella density (ρ_t^L) and flowing lamella density (ρ_{fg}^L) in Table 4.3, respectively. Based on our calculations in Chapter 4, it was found that the two definitions of flowing lamella density, which are ρ_{fg}^L and n_{fg}^L, are actually related to each other for the grain pack (Eq. 4.6 in Chapter 4). Note that this relation is independent of the flow domain; therefore it can also be written for overall lamella density (ρ_t^L and n_t^L):

$$\rho_t^L \propto n_t^L k^{3/2} \tag{6.4}$$

Figure 6.1a shows plot of the logarithm of n_t^L vs. ρ_t^L for the grain pack (GP) and the sandstone (SS) and for different permeabilities. The relation in Eq. 6.4 can only be used for one pore-network type to collapse the curves in Figure 6.1a having different permeabilities onto each other. In order to make this relation independent of pore-network type, permeability term k in Eq 6.4 is replaced by the second power of log-normal mean of pore-throat radius $(\overline{R})^2$ (Eq. 6.5). Figure 6.1b clearly shows that all curves in Figure 6.1a collapse onto each other by using the relation in Eq. 6.5 regardless of the pore-network type and permeability.

$$\rho_t^L \propto \left(n_t^L\right)_D \tag{6.5a}$$

$$\left(n_t^L\right)_D = n_t^L \left(\overline{R}\right)^3 \tag{6.5b}$$

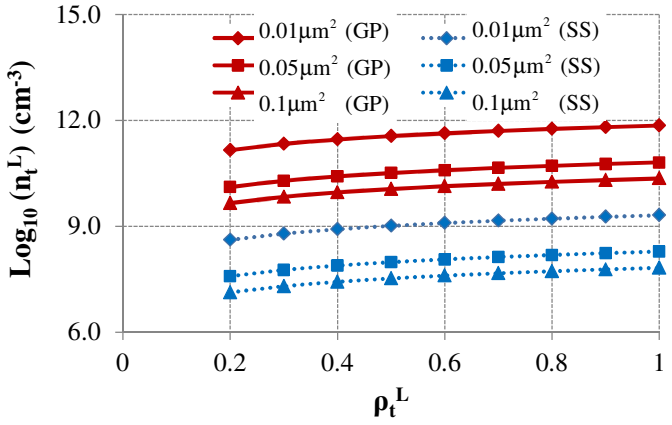

(a)

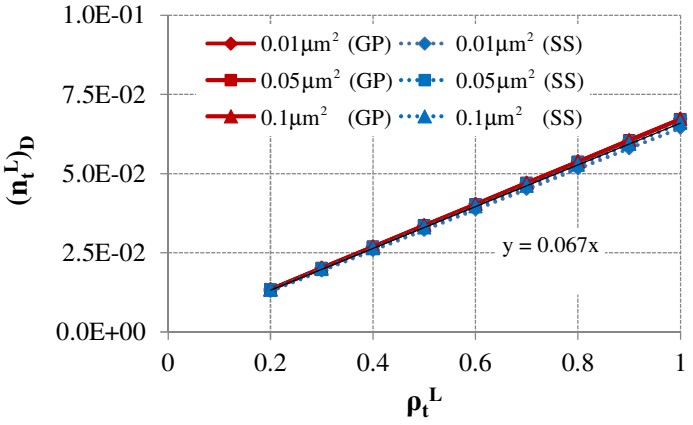

(b)

Figure 6.1 (a) Plot of the logarithm of n_t^L vs. ρ_t^L and (b) plot of $(n_t^L)_D$ vs. ρ_t^L for the grain pack (GP) and the sandstone (SS) and for different permeabilities.

The relationship between $(n_t^L)_D$ and ρ_t^L in Figure 6.1b is given below:

$$\left(n_t^L\right)_D = 0.067\rho_t^L \tag{6.6}$$

Therefore, Eq. 6.5b and Eq. 6.6 can be used to convert n_t^L, which is calculated by population balance model, to ρ_t^L so that flowing gas fraction (X_{fg}), flowing lamella density, ρ_{fg}^L and effective gas viscosity (μ_g^f) can be calculated through the analytical correlations obtained in Chapter 5.

6.1.1.2 The Effect of Surfactant Concentration and Adsorption on Lamella Density

Surfactant is not defined as a component in our model, so there is no surfactant dispersion or adsorption calculation. Local-equilibrium states that net lamella density is calculated as long as gas and liquid phases exist in porous media. In order words, net lamella density is a state function. In real physics, surfactant dispersion in aqueous phase and adsorption on rock surface controls the surfactant concentration, which may delay the lamella generation and therefore pressure buildup in porous media. In order to history match simulation results with real core-flood data an additional accumulation term has been added to the local-equilibrium approximation to the full population balance model:

$$\xi \frac{\partial}{\partial t}\left(S_g n_t^L\right) = S_g\left(c_1 v_w \left(v_g^f\right)^{1/3} - c_{-1} n_t^L\right) \tag{6.7}$$

Chen (2009) used the same kind of accumulation term to improve numerical stability of their foam model. In here, however, it is both used for numerical stability and delaying lamella generation due to surfactant adsorption and dispersion in porous media. ξ in Eq. 6.7 can be called as a retardation factor. If $\xi = 0$, then the Eq. 6.7 is equivalent to the regular local-equilibrium approximation.

6.1.2 The Simulation Algorithm

In this study, a one-dimensional black-oil model is modified to simulate incompressible two-phase flow of gas and water in porous media. Discretization of the material balance equations is given in the Appendix D. The simulator is coded in Matlab

environment and implicit pressure explicit saturation (IMPES) solution method is used. The detailed simulation algorithm of the developed mechanistic foam model is provided in Figure 6.2. In each time step, transmissibility of gas and water phases are calculated, and then pressure field is solved implicitly. Saturation of each phase, however, is calculated explicitly, which enables one to calculate interstitial gas and water velocities. These velocities are the inputs of the population balance model to calculate overall lamella density, ρ_t^L. The next step is to calculate flowing gas fraction, X_{fg} (Eqs. 5.2, 5.3, 5.4, Figures 5.4, 5.5, and 5.8 in Chapter 5) and flowing lamella density, ρ_{fg}^L (Eqs. 5.5, 5.6, Figures 5.10, and 5.13 in Chapter 5) by using pressure gradient and overall lamella density. The following step is to calculate effective gas viscosity, μ_g^f (Eqs. 5.11, 5.14, 5.15, and Figure 5.17 in Chapter 5) by using the calculated flowing lamella density and capillary number.

The final step before calculating the transmissibility of each phase for the next time step is to calculate gas relative permeability with foam (k_{rg}^f). For this purpose, the normalized gas saturation (S_{gn}) in Corey-type gas relative permeability is modified to include the effect of X_{fg} on k_{rg}^f as below:

$$S_{gn} = \frac{\left(S_g - S_{gr}\right) X_{fg}}{\left(1 - S_{wc} - S_{gr}\right)} \tag{6.8a}$$

$$k_{rg}^f = k_{rg}^o \left(S_{gn}\right)^{e_g} \tag{6.8b}$$

Where S_g, S_{gr}, S_{wc}, k_{rg}^o, and e_g are gas saturation, residual gas saturation, connate water saturation, end-point and exponent of gas relative permeability without foam, respectively. Water relative permeability is not affected by the presence of foam in porous media. Therefore, regular Corey-type water relative permeability is used:

$$S_{wn} = \frac{\left(S_w - S_{wc}\right)}{\left(1 - S_{wc} - S_{gr}\right)} \tag{6.9a}$$

$$k_{rw} = k_{rw}^{o}\left(S_{wn}\right)^{e_w} \tag{6.9b}$$

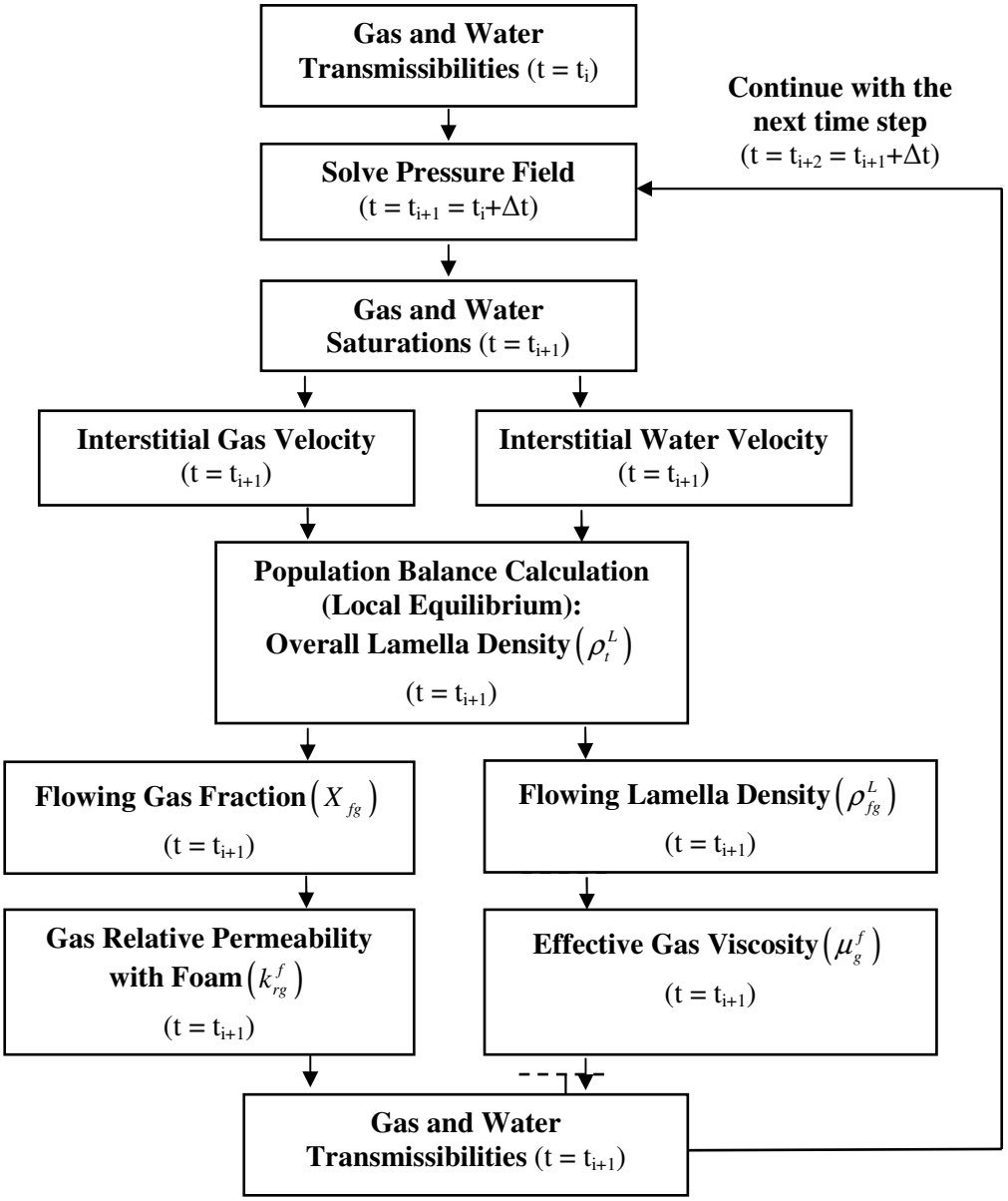

Figure 6.2 The simulation algorithm of the developed mechanistic foam model.

6.2 RESULTS AND DISCUSSION

This section is divided into two parts. In the first part, some synthetic simulation cases are run to demonstrate 1D unsteady-state and steady-state flow of foam through porous media. In all simulation cases, porous media is fully saturated with water initially. Moreover, water and gas are co-injected at constant rate at the injection boundary and produced at constant pressure at the production boundary. The 1D model is divided into 30 grids. The simulation model is valid for incompressible flow of gas and water. In the second part, simulation results are history matched with the core-flood data (Ren et al., 2011; Ren, 2012) obtained by co-injecting supercritical CO_2 and surfactant solution into sandstone and dolomite cores initially saturated with brine.

6.2.1 Synthetic Simulation Cases

6.2.1.1 Unsteady-State Foam Flow

In Figures 6.3 and 6.4 pressure difference (ΔP), pressure gradient (∇P), saturation, phase mobility, flowing gas fraction, X_{fg}, effective gas viscosity, μ_g^f, and lamella density profiles are plotted at three different pore-volume injected (0.1, 0.3, 0.45 PV) in the presence of foam and in the absence of foam, respectively. For both cases, fractional flow of gas in the injection stream (f_g) is 0.8 (u_g = 0.33 m/d and u_w = 0.08 m/d). Furthermore, the rock and fluid properties, and the model parameters are provided in Tables 6.1 and 6.2. M_{par} is a history matching parameter, which will be explained and discussed in the upcoming part. Its value is arbitrary here. The values of $\overline{R}$, σ_R, and L_c at the given permeability in Table 6.1 are calculated from their dimensionless values for the pore-network model of sandstone in Table 3.1 in Chapter 3. Moreover, the reference rate constant for lamella generation (c_1^o) in Table 6.2 is set to zero for the case without foam (Figure 6.4).

The simulation results show that gas mobility in porous media is significantly reduced by foam (Figure 6.3) when it is compared to the case without foam (Figures 6.4). A piston-like displacement, delayed gas breakthrough and pressure build-up before the foam front have been observed (Figure 6.3). Similar pressure and saturation profiles were also observed by Kovscek et al. (1995, 1997) and Chen et al. (2010) in their core-flood experiments. Pressure gradient, ∇P in the porous media is expected to be higher than threshold pressure gradient of foamed gas (∇P_{M}) to initiate gas flow. Figure 6.3 shows that ∇P is above ∇P_{M} towards the injection boundary; however it is below ∇P_{M} in the vicinity of foam front. Therefore, flowing gas fraction, X_{fg} is close to zero at the foam front. As the gas phase accumulates at the foam front, the pressure builds up and at some point ∇P exceeds ∇P_{M}, which moves the foam front one step forward.

At the front foamed gas flows very slowly due to low flowing gas fraction, which decreases capillary number and leads to more viscous foam at the front (Figure 6.3). Furthermore, as it is expected from the results of pore-network study in Chapter 4, flowing lamella density is not equal to overall lamella density during the unsteady-state flow of foam (Figure 6.3).

Table 6.1 Rock and fluid properties used in the synthetic simulation cases.

Rock and Fluid Properties			
k **[µm^2]**	9.88×10^{-2} (100 mD)	L_{c} **[µm]**	48.9
ϕ	0.17	L_{x} **[m]**	0.3048
$\bar{R}$ **[µm]**	9.88	c_A **[m^2]**	1.73×10^{-3}
σ_{R} **[µm]**	4.58	γ **[N/m]**	30×10^{-3}

Table 6.2 Model parameters used in the synthetic simulation cases.

Fluid Mobility Parameters			**Population Balance Parameters**	
k_{rw}^{o}	1.0		c_{1}^{o}	6×10^{21}
e_{w}	3.0		c_{-1}^{o}	30
k_{rg}^{o}	0.7		P_{c}^{*} [kPa]	50.0
e_{g}	3.0		ξ	0.1
S_{wc}	0.25			
S_{wi}	1.0		**Boundary Conditions**	
μ_{g} **[Pa-s]**	8.24×10^{-5}		P_{out} **[kPa]**	9.48×10^{3} (1375 psi)
μ_{w} **[Pa-s]**	1×10^{-3}		u_{w} **[m/d]**	0.08
M_{par}	0.03		u_{g} **[m/d]**	0.33

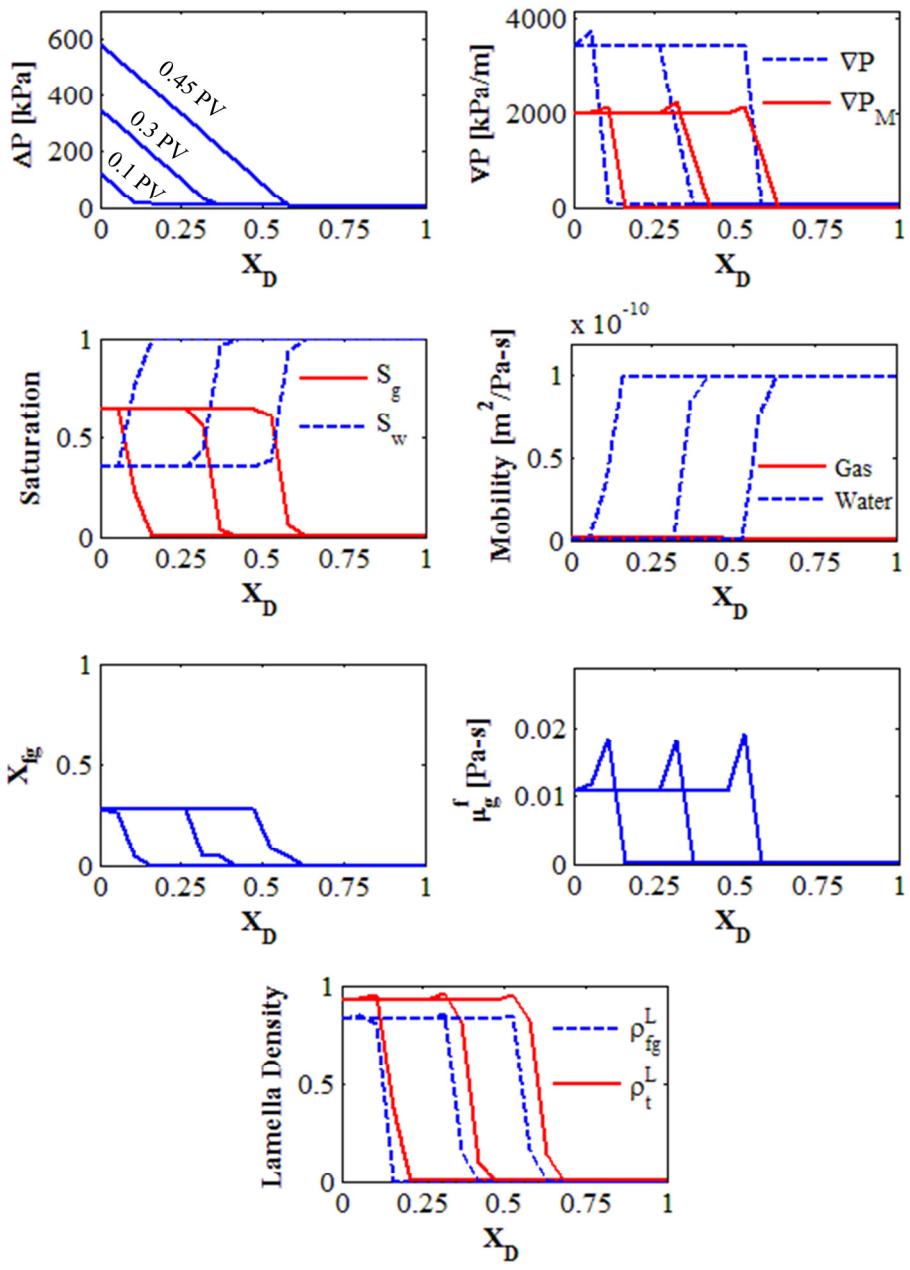

Figure 6.3 Pressure difference (ΔP), pressure gradient (∇P), saturation, phase mobility, flowing gas fraction (X_{fg}), effective gas viscosity (μ_g^f), and lamella density profiles at three different pore-volume injected (0.1, 0.3, 0.45 PV) in the presence of foam. Fractional flow of gas in the injection stream (f_g) is 0.8 (u_g = 0.33 m/d and u_w = 0.08 m/d).

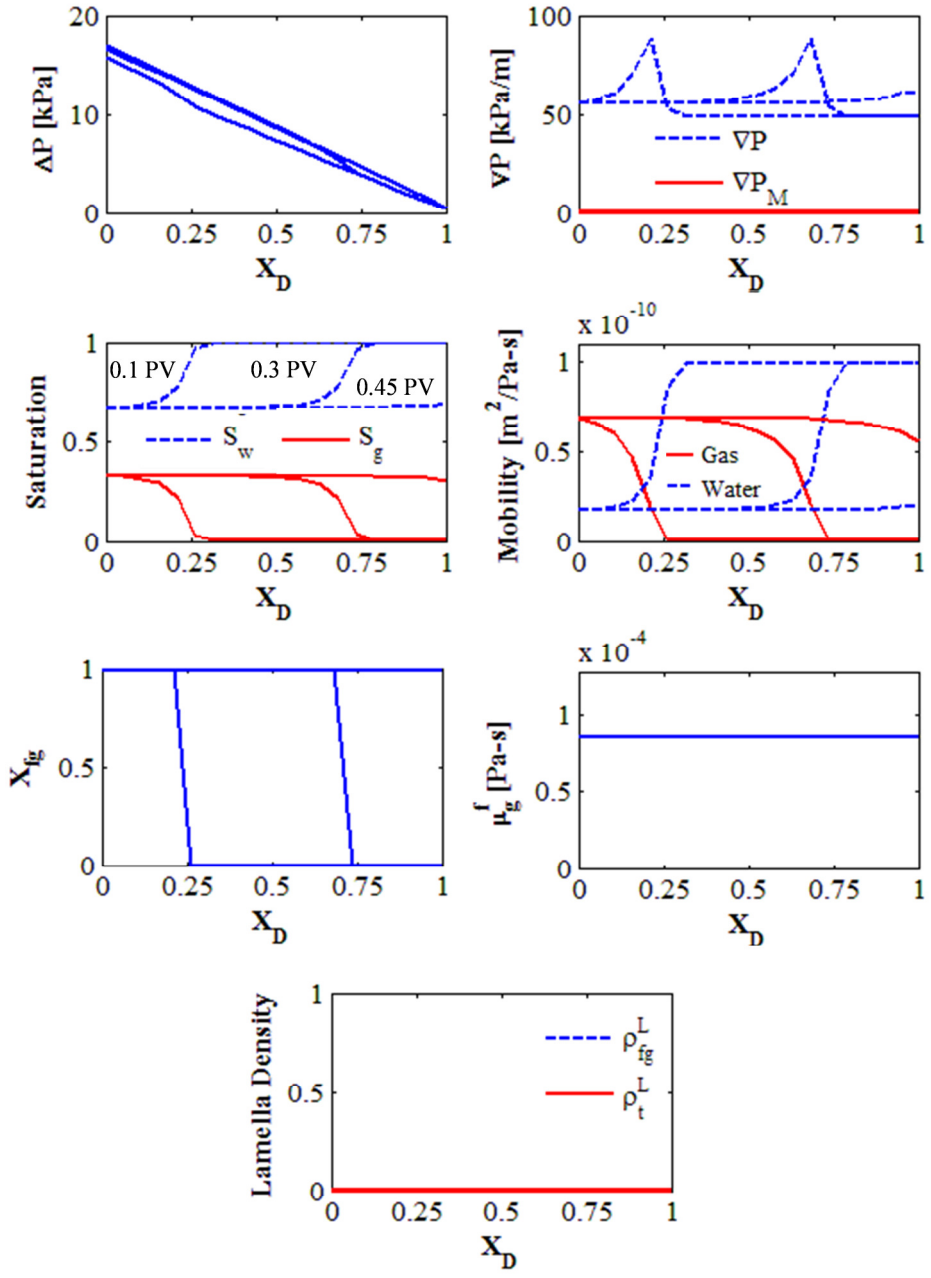

Figure 6.4 Pressure difference (ΔP), pressure gradient (∇P), saturation, phase mobility, flowing gas fraction (X_{fg}), effective gas viscosity (μ_g^f), and lamella density profiles at three different pore-volume injected (0.1, 0.3, 0.45 PV) in the absence of foam. Fractional flow of gas in the injection stream (f_g) is 0.8 (u_g = 0.33 m/d and u_w = 0.08 m/d).

6.2.1.2 Steady-State Foam Flow

In Figure 6.5, contours of pressure gradient, ∇P, flowing gas fraction, X_{fg}, and effective gas viscosity, μ_g^f of steady-state foam flow through porous media are provided. In these simulations, the rock and fluid properties, and the model parameters in Tables 6.1 and 6.2 are used except the reference rate constant for lamella generation, c_1^o, whose value is higher here (1×10^{23}). Contours of ∇P (Figure 6.5a) clearly shows the two distinct steady-state foam flow regimes (I_1: high-quality and I_2: low-quality) divided by the critical fractional flow of gas (f_g^*) of 0.75. The same steady-state flow regimes were also observed by many investigators in their experiments (Osterloh and Jante, 1992; Alvarez et al., 2001). As it is expected, steady-state pressure gradient in low-quality regime is a strong function of gas velocity. In high-quality regime, however, it is mostly dependent on water velocity (Figure 6.5a). Furthermore, gas trapping and effective gas viscosity are higher in the low-quality regime than those in the high-quality regime (Figures 6.5b, 6.5c).

Figure 6.6 shows contours of water saturation (S_w), overall lamella density, ρ_t^L, and flowing lamella density, ρ_{fg}^L of steady-state foam flow. S_w is not changing much when $f_g > f_g^*$ (Figure 6.6a), which is consistent with the definition of critical water saturation (S_w^*) by Khatib et al. (1988). Furthermore, overall and flowing lamella densities in the high-quality flow regime decrease sharply with water velocity (Figures 6.6b and 6.6c), which is the reason for sharp decrease in ∇P in the same flow regime (Figure 6.5a). This result also justifies that lamella coalescence is the dominant mechanism in the high-quality regime defining the foam flow behavior (Osterloh and Jante, 1992; Alvarez et al., 2001).

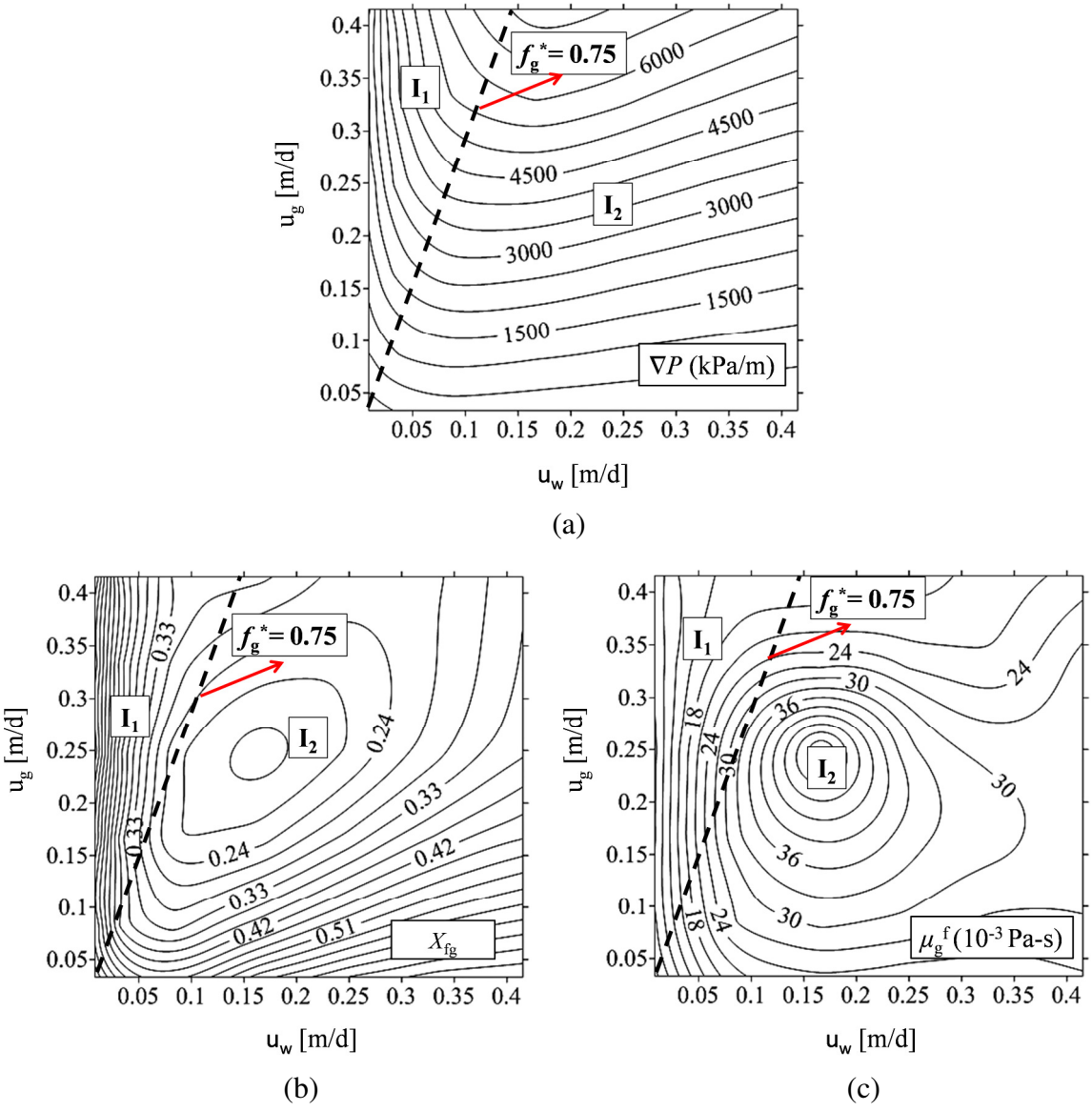

Figure 6.5 Contours of (a) pressure gradient (∇P), (b) flowing gas fraction (X_{fg}), and (c) effective gas viscosity (μ_g^f) of steady-state foam flow. The estimated critical fractional flow of gas (f_g^*) is 0.75. I_1 and I_2 denote the high-quality and low-quality foam flow regimes, respectively.

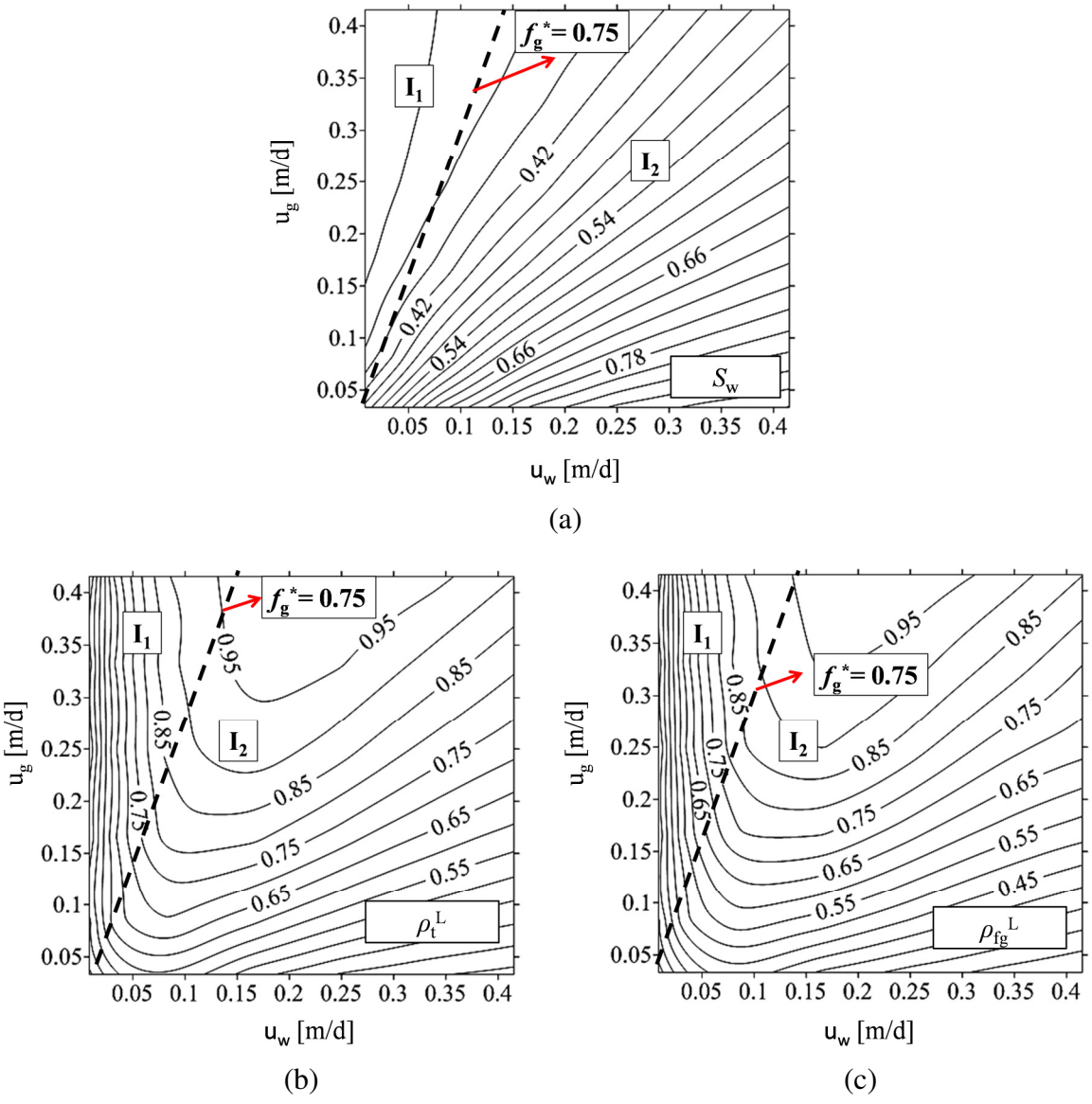

Figure 6.6 Contours of (a) water saturation (S_w), (b) overall lamella density (ρ_t^L), and (c) flowing lamella density (ρ_{fg}^L) of steady-state foam flow. The estimated critical fractional flow of gas (f_g^*) is 0.75. I_1 and I_2 denote the high-quality and low-quality foam flow regimes, respectively.

Contours of pressure gradient, ∇P for the base case ($c_1^{o} = 1\times10^{23}$, $P_c^{*} = 50$ kPa) in Figure 6.7a is the same with Figure 6.5a. Comparison of the base case with the other two cases in Figures 6.7b ($c_1^{o} = 1\times10^{22}$) and 6.7c ($P_c^{*} = 35$ kPa) show that critical fractional flow of gas, f_g^{*} decreases with reference rate constant for lamella generation, c_1^{o} and critical capillary pressure, P_c^{*}. Lower the f_g^{*}, weaker the foam and higher the gas mobility in porous media.

The magnitude of c_1^{o} depends on the type of porous media used, since snap-off is a mechanical process which does not require the presence of surfactant. However, P_c^{*} is a decreasing function of both gas flow rate and permeability of porous medium (Khatib et al., 1988). Furthermore, P_c^{*} increases with surfactant concentration (Alvarez et al., 2001). Unfortunately, there is no comprehensive model in the literature relating P_c^{*} to the aforementioned parameters. Therefore, the discussion here is limited to changing the value of P_c^{*} and showing its effect on contours of pressure gradient. However, the results in Figure 6.7 are consistent with the experimental results of Alvarez et al. (2001).

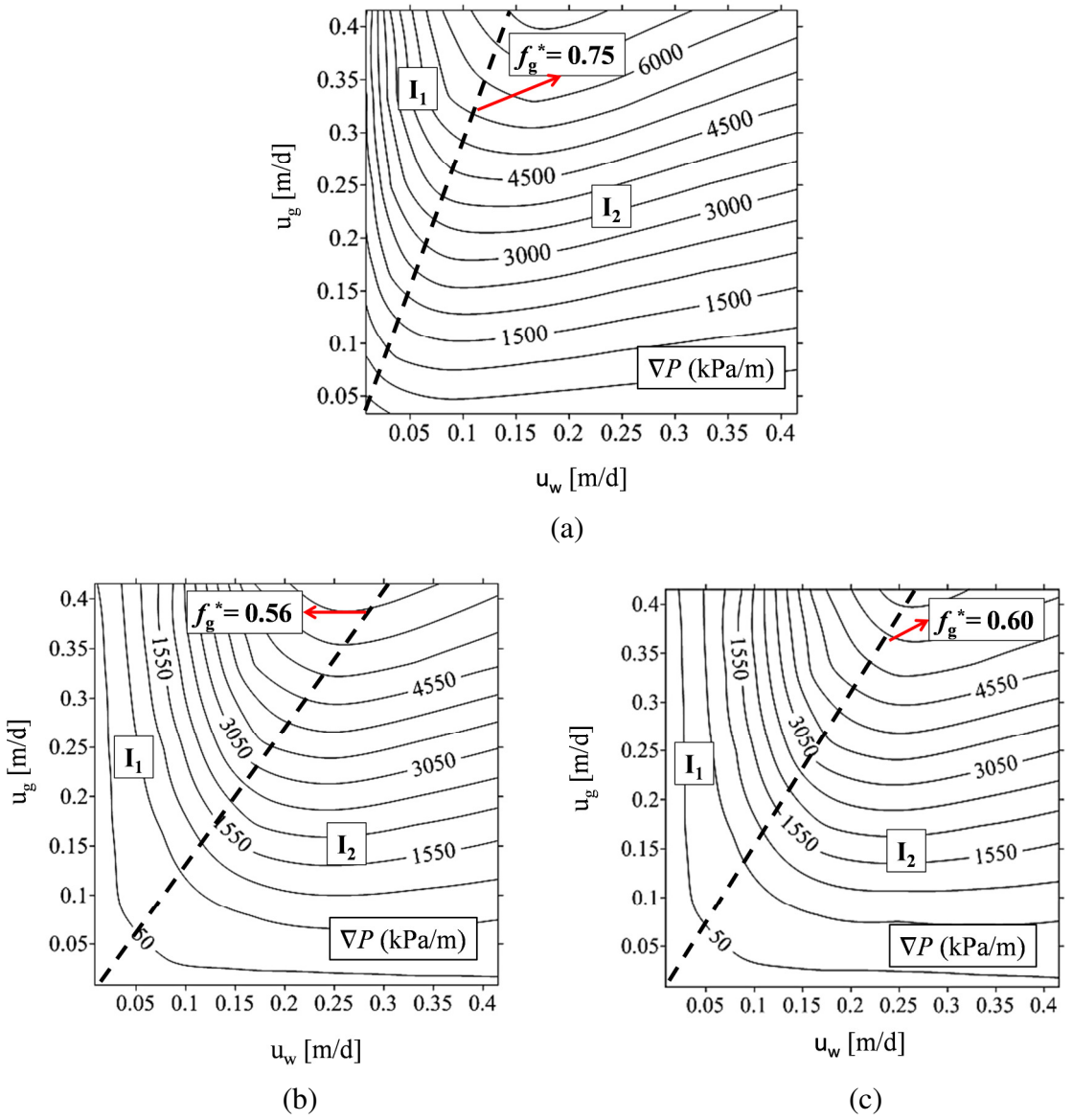

Figure 6.7 (a) Base case ($c_1^o = 1\times10^{23}$, $P_c^* = 50$ kPa), (b) the effect of a decrease in reference rate constant for lamella generation ($c_1^o = 1\times10^{22}$) and (c) the effect of a decrease in critical capillary pressure ($P_c^* = 35$ kPa) on critical fractional flow of gas (f_g^*). I_1 and I_2 denote the high-quality and low-quality foam flow regimes, respectively.

6.2.2 History Matching of Foam Core Floods

In this part, the simulation results are history matched with two different core-flood data obtained by co-injecting supercritical CO_2 (u_g = 0.28 m/d) and surfactant solution (u_w = 0.09 m/d) into sandstone and dolomite cores which are initially saturated with brine (Ren et al., 2011; Ren, 2012). The back-pressure and temperature in the system are 9.48×10^3 kPa (1375 psi) and 20 C^o, respectively. The measured parameters during the core-flood experiments are inlet-outlet pressure difference (P_{in}-P_{out}) and the weight of surfactant solution at the outlet. Average water saturation $(S_w)_{avg}$ is calculated as a function of total-pore volume injected by using the material balance equation. The details of the experimental setup and procedure can be found in Ren (2012).

Six different history matching parameters are used here: reference rate constant for lamella generation, c_1^o, reference rate constant for lamella coalescence, $c\text{-}_1^o$, critical capillary pressure, P_c^*, a matching parameter controlling the dimensionless pressure gradient, M_{par} and two retardation factors (ξ_1, ξ_2). c_1^o, $c\text{-}_1^o$, P_c^* and M_{par} are used to history match (P_{in}-P_{out}) during steady-state foam flow. The unsteady-state flow period is divided into two time intervals for history matching purposes. The first interval is between the start of experiment and the time at which (P_{in}-P_{out}) starts to buildup. The second interval starts with the end of first one and continues until steady-state is reached. Therefore, the retardation factors ξ_1 and ξ_2 are used to history match (P_{in}-P_{out}) and $(S_w)_{avg}$ in the first and second time intervals of the unsteady-state flow period, respectively.

Recall that the ($2\gamma/L_c$) term in the dimensionless pressure gradient (Eq. 5.1 and Eq. 5.2 in Chapter 5) is equivalent to yield stress (τ_o) (Eq.3.7 in Chapter 3) in the continuum fluid flow modeling. This relation is obtained by equating the mobilization pressure difference of a yield-stress fluid in a capillary tube ($\Delta P_m = 2L\tau_o/R$) to ΔP_m of a lamella in a pore throat, which scales by ($4\gamma/R$). Note that the scaling relationship for a

lamella is valid for static conditions and does not include the dynamic lamella flow effects on ΔP_m: surface elasticity, viscosity and dynamic lamella tension (Schramm, 1994; Schramm and Green, 1995; Xu and Rossen, 2000; Falls et al., 1989). Therefore, a matching parameter, M_{par}, which is multiplied by $(2\gamma/L_c)$ in the dimensionless pressure gradient, is introduced here. Using a multiplier M_{par} enables us to stretch/shrink flowing gas fraction (Figure 5.2 in Chapter 5) and flowing lamella density curves (Figure 5.9 in Chapter 5) along the pressure gradient axis for all overall lamella densities to history match the simulation results with the core-flood data.

6.2.2.1 Sandstone Case

Rock and fluid properties for the core-flood experiment using a sandstone core are provided in Table 6.3. The permeability (k) and the porosity (ϕ) of the sandstone are measured values. Since there is no information about the pore-throat size distribution of the sandstone core, the values of $\overline{R}$, σ_R, and L_c are calculated at the measured permeability by using their dimensionless values from the pore-network model of a sandstone in Table 3.1 in Chapter 3.

Table 6.3 Rock and fluid properties for the core-flood experiment using a sandstone core.

Rock and Fluid Properties			
k **[µm^2]**	2.33×10^{-1} (236 mD)	L_c **[µm]**	74.9
ϕ	0.236	L_x **[m]**	0.2921
$\overline{R}$ **[µm]**	15.1	c_A **[m^2]**	1.55×10^{-3}
σ_R **[µm]**	7.01	γ **[N/m]**	30×10^{-3}

Figure 6.8a shows that the simulated (P_{in}-P_{out}) is successfully history matched with the measured one during the unsteady-state and steady-state flow periods by using the fluid mobility parameters and boundary conditions in Table 6.4 and the history matching parameters in Table 6.5. It is important to note that the parameters in Table 6.4 are measurable. However, the parameters in Table 6.5 (c_1^o, $c\text{-}_1^o$, P_c^*, M_{par}) are theoretical. Therefore, the values of c_1^o, $c\text{-}_1^o$, P_c^* are changed based on their reference values from Chen et al. (2010) at a specific M_{par} until the simulated (P_{in}-P_{out}) at the steady-state is matched with the experimental data. If the match is not satisfactory, then a different M_{par} is tried. After matching the level of pressure drop across the core during steady state flow, the best values of the retardation factors ξ_1 and ξ_2 are found to match the increasing trend in pressure drop during unsteady-state flow. It is remarkable that the pressure fluctuations observed in the experimental data during the steady-state foam flow has been captured by the model (Figure 6.8a). Furthermore, the simulation results show the general decreasing trend of average water saturation (Figure 6.8b): (1) gas breakthroughs, (2) foam gets stronger and displaces more water and (3) $(S_w)_{avg}$ levels off at the steady-state. The simulated $(S_w)_{avg}$ during the steady-state flow of foam is a bit higher than the measured one. This problem can be solved by decreasing the connate water saturation (S_{wc}) in the input file. However, lowering the S_{wc} further leads to some numerical issues, so we could not test the lower connate water saturations. A better numerical control tool is required. Besides, the measured $(S_w)_{avg}$ is calculated from material balance equation, which makes its accuracy questionable.

The simulation results indicate that a significant pressure build-up can only occur if overall lamella density, ρ_t^L is greater than 0.65, which corresponds to the discontinuous-gas foam flow regime in which a threshold pressure gradient exist. Recall that ρ_t^L lower than 0.65 enables gas to flow through lamella unoccupied paths, which

does not reduce the gas mobility much. Therefore, the retardation factors ξ_1 and ξ_2 in Table 6.5 actually correspond to continuous-gas and discontinuous-gas foam flow regimes, respectively.

Table 6.4 Fluid mobility parameters and boundary conditions for the sandstone core flood case.

Fluid Mobility Parameters				
k_{rw}^{o}	0.7		S_{wc}	0.25
e_w	4.0		S_{wi}	1.0
k_{rg}^{o}	0.7		μ_g **[Pa-s]**	8.24×10^{-5}
e_g	3.0		μ_w **[Pa-s]**	1×10^{-3}
Boundary Conditions				
u_w **[m/d]**	0.09		P_{out} **[kPa]**	9.48×10^{3} (1375 psi)
u_g **[m/d]**	0.28			

Table 6.5 History matching parameters for the sandstone core flood case.

Steady-State Flow			**Unsteady-State Flow**	
c_1^o	11×10^{21}		ξ_1 *if* $\left(\rho_t^L \le 0.65\right)$	5×10^{6}
c_{-1}^o	50.0			
P_c^* [kPa]	50.0		ξ_2 *if* $\left(\rho_t^L > 0.65\right)$	3×10^{7}
M_{par}	0.19			

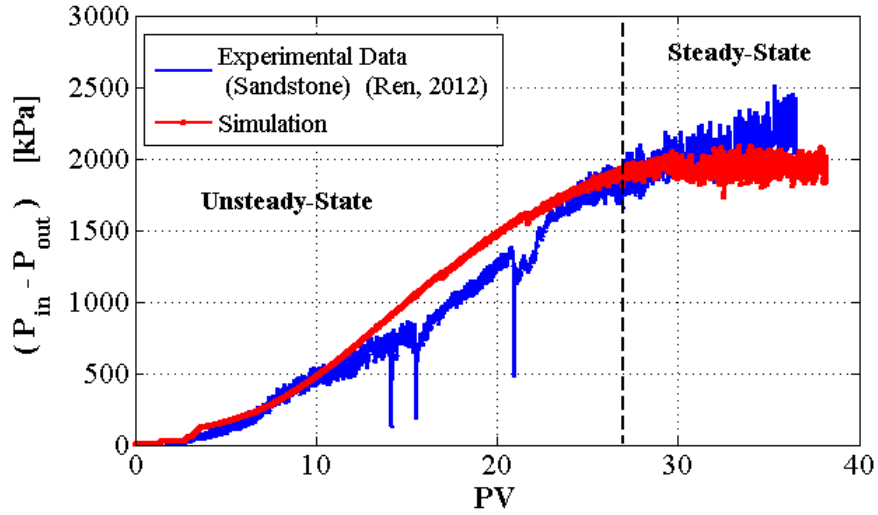

(a)

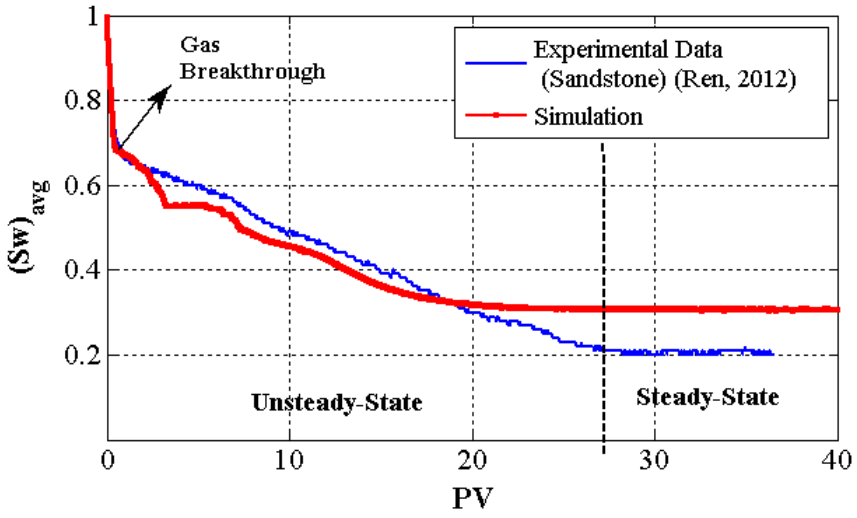

(b)

Figure 6.8 History matching the simulated (a) inlet-outlet pressure difference (P_{in}-P_{out}) and (b) average water saturation $(S_w)_{avg}$ with the experimental data (Ren, 2012) obtained by co-injecting supercritical CO_2 (u_g = 0.28 m/d) and surfactant solution (u_w = 0.09 m/d) into a sandstone core initially saturated with brine.

6.2.2.2 Dolomite Case

Rock and fluid properties for the core-flood experiment using a dolomite core are provided in Table 6.6. The permeability, k and the porosity, ϕ of the dolomite core are measured values. $\bar{R}$, σ_R, and L_c, however, are calculated at the measured permeability by using the method described in the sandstone case.

Both the simulated (P_{in}-P_{out}) and $(S_w)_{avg}$ are successfully history matched with the experimental data (Figures 6.9a and 6.9b) during the unsteady-state and steady-state foam flow by using the fluid mobility parameters and boundary conditions in Table 6.7 and the history matching parameters in Table 6.8. The pressure fluctuations during steady-state flow are again captured by the model (Figures 6.9a). Especially, the decreasing trend in average water saturation after gas breakthrough has been matched successfully (Figures 6.9b).

It is important to note that the retardation factor, ξ_1 used for the dolomite case (Table 6.8) is smaller than the ξ_1 used for the sandstone case (Table 6.5). This could be an indication of different level of surfactant adsorption in different porous medium, which controls the start of the lamella generation and pressure buildup.

Table 6.6 Rock and fluid properties for the core-flood experiment using a dolomite core.

Rock and Fluid Properties				
k **[µm²]**	4.32×10^{-1} (437 mD)		L_c **[µm]**	102.0
ϕ	0.1974		L_x **[m]**	0.2921
$\bar{R}$ **[µm]**	20.6		c_A **[m²]**	1.55×10^{-3}
σ_R **[µm]**	9.55		γ **[N/m]**	30×10^{-3}

Table 6.7 Fluid mobility parameters and boundary conditions for the dolomite core flood case.

Fluid Mobility Parameters				
k_{rw}^{o}	1.0		S_{wc}	0.15
e_{w}	3.0		S_{wi}	1.0
k_{rg}^{o}	0.7		μ_g **[Pa-s]**	8.24×10^{-5}
e_{g}	3.0		μ_w **[Pa-s]**	1×10^{-3}
Boundary Conditions				
u_w **[m/d]**	0.09		P_{out} **[kPa]**	9.48×10^{3} (1375 psi)
u_g **[m/d]**	0.28			

Table 6.8 History matching parameters for the dolomite core flood case.

Steady-State Flow			**Unsteady-State Flow**	
c_{1}^{o}	7.7×10^{21}		$\xi_1 \;\; if \left(\rho_t^L \le 0.65\right)$	5×10^{5}
c_{-1}^{o}	50.0			
P_c^* [kPa]	50.0		$\xi_2 \;\; if \left(\rho_t^L > 0.65\right)$	3.5×10^{7}
M_{par}	0.03			

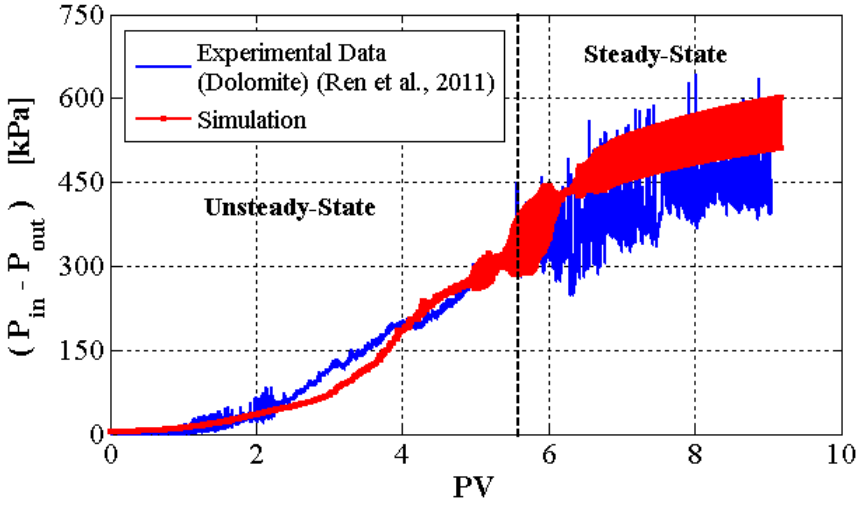

(a)

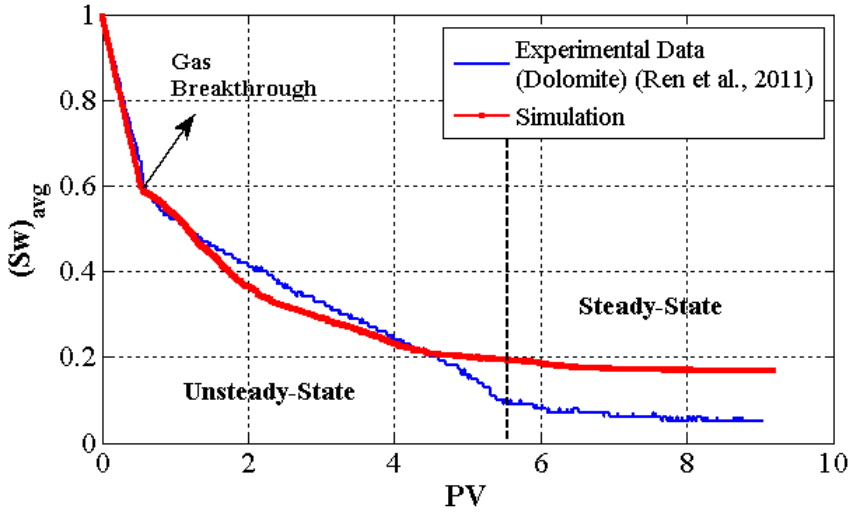

(b)

Figure 6.9 History matching the simulated (a) inlet-outlet pressure difference (P_{in}-P_{out}) and (b) average water saturation $(S_w)_{avg}$ with the experimental data (Ren et al., 2011) obtained by co-injecting supercritical CO_2 (u_g = 0.28 m/d) and surfactant solution (u_w = 0.09 m/d) into a dolomite core initially saturated with brine.

6.3 CONCLUSIONS

In conclusion, analytical correlations of flowing gas fraction and effective gas viscosity obtained from the pore-network study in the previous chapters and a modified lamella population balance model are used to develop a mechanistic foam model based on a continuum approach. The developed model includes the effects of pressure gradient, foam texture, rock and fluid properties on the dynamics of gas trapping, therefore gas relative permeability, and effective gas viscosity. Furthermore, addition of the modified population balance model to the developed foam mobility model enable us to relate foam texture to the dynamics of lamella generation and coalescence mechanisms, which completes the big picture for the dynamics of foam mobility in porous media.

The results of the synthetic simulation cases show that both unsteady-state and steady-state flow of foam through porous media have been successfully simulated qualitatively when they are compared to the experimental results in the literature. High-quality and low-quality flow regimes have been identified on contour maps of pressure gradient. For the first time in the foam literature, contours of flowing gas fraction and effective gas viscosity has been obtained. While steady-state pressure gradient is a strong function of gas velocity in the low-quality flow regime, it is mostly dependent on liquid velocity in the high-quality regime. Furthermore, gas trapping and effective gas viscosity are higher in the low-quality regime than those in the high-quality regime. In the high-quality flow regime, average water saturation has almost a constant value, which is consistent with the definition of critical water saturation in the foam literature. Moreover, lamella coalescence is the dominant mechanism in the high-quality regime defining the foam flow behavior. In addition, critical fractional flow of gas decreases with reference rate constant for lamella generation and critical capillary pressure. All these

aforementioned results are consistent with the findings of experimental studies in the foam literature.

The simulated pressure difference across the core and average water saturation during the unsteady-state and steady-state flow periods have been successfully history matched with the data obtained from core-flood experiments (Ren et al., 2011; Ren, 2012) by co-injecting supercritical CO_2 and surfactant solution into sandstone and dolomite cores initially saturated with brine. Since surfactant dispersion and adsorption mechanisms are not defined in the simulation model, retardation factors have been introduced into the local equilibrium approximation of the full population balance model to history match the core-flood data during the unsteady-state foam flow.

Chapter 7: Conclusions and Suggestions for Future Work

7.1 SUMMARY OF THE DISSERTATION

In the presence of foam, gas mobility in porous media is reduced by gas trapping and viscous resistance of flowing lamellas to gas flow. In mechanistic modeling of foam, gas trapping modifies the gas relative permeability, while the resistance of flowing lamellas is represented by an effective gas viscosity. To have a complete understanding of foam mobility in porous media, the effects of pressure gradient, foam texture, rock and fluid properties on gas trapping, and therefore gas relative permeability, and effective gas viscosity should be known. A literature review in Chapter 2 reveals that there has been no comprehensive foam modeling study exploring the dynamics of gas trapping and its interaction with flowing lamella density, and therefore effective gas viscosity.

In this dissertation, dynamics of foam mobility in porous media has been studied with a special attention to gas trapping and its effects on gas relative permeability and effective gas viscosity by using 3D pore-network models coupled with fluid models representing a lamella flow through a pore throat. Based on the research objectives stated in Chapter 1, the following work has been completed:

- The first objective was to improve our understanding of the dynamics of gas trapping and remobilization mechanism by investigating possible models for the relationships between pressure gradient and gas trapping and between gas trapping and gas mobility. In Chapter 3, network models mapped from two different types of porous media (computer-generated sphere packs and sandstones digitized from real media) are used to simulate foam flow through porous medium. Due to the similarities between the flow of Non-Newtonian fluids that exhibit a yield stress and the flow of a foam lamella through a pore throat,

Bingham, Herschel-Bulkley and two additional models that we call constant viscosity foam and power-law viscosity foam are used. Furthermore, the network models are used to predict flow paths, the threshold pressure gradient, and Darcy velocity of foam. Finally, a new macroscopic model including pressure gradient-dependent macroscopic properties are presented.

- The second objective was to obtain correlations of flowing gas fraction as functions of pressure gradient, lamella density, rock and fluid properties and to quantify the relationship between flowing gas fraction and gas relative permeability. Our model in Chapter 3 is expanded in Chapter 4 to describe the effects of foam texture (lamella density) on flowing gas fraction, and therefore gas relative permeability in the grain pack. In Chapter 5, characteristic pore-network properties are included into the definition of dimensionless pressure gradient to obtain analytical correlations of flowing gas fraction independent of pore-network type.
- The third objective was to generate analytical correlations of effective gas viscosity as functions of capillary number, lamella density and rock properties. In Chapters 4 and 5, a commonly used pore-level apparent gas (lamella) viscosity model is up-scaled to effective gas viscosity in the grain pack and in the sandstone. The dependency of effective gas viscosity on capillary number and flowing lamella density are quantified. In Chapter 5, the effect of different pore-network types on effective gas viscosity is investigated. By including the characteristic pore-network properties into the definition of dimensionless pressure gradient, correlations of flowing lamella density, which is an input parameter for

effective gas viscosity, as functions of pressure gradient, overall lamella density, rock and fluid properties are obtained.

- The fourth objective was to quantify the individual contributions of gas relative permeability with trapped gas and effective gas viscosity to total foam mobility and to understand the flow dynamics between the flowing and trapped gas. In Chapter 4, dimensional analysis in scaling of these two rheological quantities with pressure gradient and lamella density is discussed. The dynamics of foam mobility in a pore network where the respective effects of lamella density and rheological behavior of flowing foam on gas trapping and relative gas permeability are quantified for the first time. Furthermore, the functional relationship between effective gas viscosity and flowing lamella density in the presence of dynamic trapped gas is verified.
- The last objective was to develop a mechanistic foam flow model and to history match the simulation results with real core-flood data. In Chapter 6, the analytical correlations of flowing gas fraction and effective gas viscosity developed in Chapters 4 and 5 are used with a modified population balance model to develop a mechanistic foam flow model. Unsteady-state and steady-state flow behavior of foam through porous media have been successfully demonstrated with synthetic simulation cases. Finally, the simulation results have been successfully history matched with the data obtained from core-flood experiments which were conducted by Ren (2012) and Ren et al. (2011) by co-injecting supercritical CO_2 and surfactant solution into a sandstone and a dolomite core initially saturated with brine.

7.2 KEY CONCLUSIONS

The major conclusions drawn from this study are provided below:

- For strong foam (one lamella per pore throat), the threshold path is independent of the fluid model used in this study (Bingham, Herschel-Bulkley, constant viscosity foam, and power-law viscosity foam) or fluid properties (consistency and shear thinning indexes). Moreover, the flow is dominated by yield-stress effects in the initial path, which is completely different from either the percolation cluster or backbone cluster from classical percolation theory. Above the threshold gradient, however, pore pressures reflect both yield-stress and viscous effects, and therefore are fluid-dependent. Although pores/throats open in different sequences for the different fluid models, pore volume open to flow is a weak function of the fluid model and fluid rheological properties.
- Threshold pressure gradient in a network model of a sandstone sample is smaller than that in a network model of computer generated grain packs having the same permeability. Log-normal mean of the pore-throat radius distribution for the sandstone is greater than that for the grain pack. The larger the mean pore-throat radius, the easier the foam flow initiates. Furthermore, the sandstone requires more pressure gradient above threshold pressure gradient to open all pores than the grain pack does. This is partially due to the wider throat-size distribution in the sandstone; it may also represent autocorrelation in pore-throat radii or layering in the sandstone.

- The scaling of flowing fraction with pressure gradient and the dependence of superficial velocity on pressure gradient above the threshold pressure gradient are distinctly different for the sandstone and the grain pack.
- A new dimensionless macroscopic model for the flow of strong foam (one lamella per pore throat) through porous media is introduced by using empirical lamella flow equations (constant viscosity and power-law viscosity foam) and the grain pack. As flowing fraction increases with pressure gradient, the macroscopic properties of the model depend on the pressure gradient. These pressure-dependent macroscopic properties are only valid for the grain pack, since pore-scale heterogeneities in different porous media may change these curves. Furthermore, the model requires calibration with a constant viscosity foam model, which may make application to real foams difficult.
- Two key rheological features of foam mobility (i.e. gas relative permeability with trapped gas and effective gas viscosity) are quantified as functions of foam texture (lamella density), pressure gradient, capillary number, and rock and fluid properties. Flowing gas fraction increases with decreasing overall lamella density at a constant pressure gradient. Furthermore, there exists a threshold pressure gradient in the discontinuous-gas foam flow regime, which increases with overall lamella density.
- Gas relative permeability is a strong non-linear function of flowing gas fraction, opposing most of the existing theoretical models describing the effect of gas trapping on relative gas permeability. The shape of the relative gas permeability curve is poorly sensitive to overall lamella

density, which mainly controls the flowing gas fraction. This is consistently observed for all the pore-scale apparent gas viscosity models.

- Flowing and trapped lamella densities change with pressure gradient, but are not necessarily the same. This finding provides insight into the kinetics of gas trapping and does not validate one of the main assumptions underlying the population balance based foam modeling approaches that is flowing lamella density is equal to trapped lamella density.
- The functional relationship between flowing gas fraction and pressure gradient is independent of empirical and mechanistic pore-scale apparent gas (lamella) viscosity models used in this study over a wide range of overall lamella density.
- Effective gas viscosity increases nonlinearly with flowing lamella density, which opposes to the existing foam viscosity models in the literature showing a linear relationship. Moreover, shear thinning foam flow is more obvious at high flowing lamella density while Newtonian flow becomes significant at relatively low flowing lamella density.
- Effective gas viscosity is a unique function of the number of flowing lamellas normalized to the total number of pore throats open to flow. However, it also scales with overall lamella density if the number of flowing lamellas is normalized to the flowing gas volume. Therefore, scaling of effective gas viscosity with flowing lamella density depends on how the later quantity is defined. In the literature, this issue has not been reported before since the dynamics of gas trapping and remobilization and its effect on foam mobility has been neglected.

- By including the characteristic pore-network properties into the definition of dimensionless pressure gradient, analytical correlations of flowing gas fraction and flowing lamella density are obtained, which enables us to predict these parameters as a function of overall lamella density and dimensionless pressure gradient regardless of the pore-network type. Furthermore, the scaling relation between the pore-scale Hirasaki-Lawson apparent gas (lamella) viscosity and effective gas viscosity are not affected by the pore-network type.
- A mechanistic foam model has been developed by using the analytical correlations of flowing gas fraction and effective gas viscosity generated from the pore-network study. Furthermore, foam texture has been related to the dynamics of lamella generation and coalescence mechanisms through a modified population balance model.
- Unsteady-state and steady-state flow of foam through porous media has been successfully simulated. Contour maps of flowing gas fraction and effective gas viscosity are obtained for the first time in the foam literature. High-quality and low-quality flow regimes are identified on contours of pressure gradient. Moreover, the foam flow behavior in these regimes has been verified by the experimental studies in the literature.
- The simulated parameters (pressure difference across the core and average water saturation) have been successfully history matched with the data obtained from core-flood experiments (Ren, 2012; Ren et al., 2011) by co-injecting supercritical CO_2 and surfactant solution into a sandstone and a dolomite core initially saturated with brine.

7.3 RECOMMENDATIONS FOR FUTURE WORK

Based on the conclusions drawn from this study and the limitations of the developed foam model, the following future work is recommended:

- In our mechanistic foam model, surfactant is not defined as a component, therefore its dispersion in aqueous phase and adsorption on rock surface are not modeled. However, these mechanisms may affect the surfactant concentration in aqueous phase significantly and therefore lamella stability, which may delay the lamella generation and pressure build-up in porous media. In this study, a retardation factor is used in the population balance model to represent this delay and to history match the core-flood results. Therefore, it is recommended to incorporate surfactant as a component into the model to describe the effects of surfactant dispersion and adsorption on lamella generation.
- This study focuses only on the flow of foam in porous media in the absence of oleic phase. Oil has a detrimental effect on the lamella density, which reduces the effectiveness of foam to reduce gas mobility in porous media. This effect can be introduced into the population balance model so that displacement of oil by foam can be simulated.
- It is well known that measuring the flowing gas fraction in CT core-flood studies is very challenging due to the transfer of gas tracer from flowing gas to the trapped gas, which makes the accuracy of the measurements questionable. Therefore, development of a reliable procedure or an innovation in the area of the gas tracer technology is a requirement to measure flowing gas fraction correctly. This will enable us to history

match not only the pressure difference but also the flowing gas fraction, which will improve the calibration and the predictability of our model.

- Critical capillary pressure plays a very important role in controlling net lamella generation. Khatib et al (1988) experimentally showed that critical capillary pressure is a decreasing function of both gas flow rate and permeability of porous medium, however there is no comprehensive model in the literature relating these parameters. Therefore, critical capillary pressure is a matching parameter in this study. Development of a predictive and reliable model for critical capillary pressure will play a crucial role in up-scaling foam flow from core-level to field-level.
- After making necessary improvements that has been mentioned on our foam model, the one-dimensional foam flow can be extended to three-dimensional flow. This will enable one to history match the simulation results with field data. The foam model developed in this study can be implemented in a compositional reservoir simulator to model miscible foam flooding or in an advanced process and thermal reservoir simulator to model low-tension and steam foam flooding.

Appendix A: Determination of Network Pore Throat Size Distributions

The network models used in this work are created using the methods described by Al-Raoush et al. (2003). A modified Delaunay tessellation is used to extract pores and throats from the domain of grain particles. Pore locations correspond to the locations of maximum inscribed sphere in the original medium and the tessellation is used to determine the throats that connect adjacent pores. With the use of the methods described in Al-Raoush et al. (2003), several geometric properties are extracted in the network including throat hydraulic conductivity, throat surface area, pore-to-pore distance, pore volume, and aspect ratio (ratio of maximum and minimum throat radius).

Throat radii are not explicitly extracted in the generation of the network model, because the throats are not straight capillary tubes. Rather, they are converging/diverging, and possess a complex 3D geometry. Traditionally, network models have always assumed straight capillary tubes because of their simplicity; equations analogous to Eq. 3.1 and Eq. 3.2 in Chapter 3 could then be used directly. A straightforward approach would involve assigning a radius and length to each throat in the network. For example, assigning the pore-to-pore distance as the length and back-calculating a radius that gives the actual hydraulic conductivity makes sense. For simple Newtonian flows, this conversion to a network of capillary tubes is inconsequential because all that is needed to model flow is the conductivity. However, it was shown by Balhoff and Thompson (2004, 2006) that any simple conversion to a capillary-tube network will give faulty results for non-Newtonian flow. Particularly for fluids requiring a mobilization pressure drop, it was shown with finite element (FEM) simulations (Balhoff and Thompson, 2004) that the mobilization pressure drop would be incorrect because the shear stresses at the wall are not uniform in the true converging/diverging throat. Therefore, correlations based on

FEM simulations to determine a more accurate throat radius and length was developed that resulted in the correct conductivity and mobilization pressure drop.

This work uses throat geometric parameters based on the Balhoff and Thompson (2004) correlations and throat radius used in the simulations refers to the converted radius. For completeness we have included the throat radius distributions of both the sphere pack (Figure A.1) and the sandstone (Figure A.2). The permeability of both medium is set to 9.88×10^{-10} cm^2 (100mD). In Figure A.1a the distribution is shown if we had used a radius based on the hydraulic conductivity and pore-to-pore distance (i.e. the "wrong" radius). This distribution has a mean of 1.44×10^{-4} cm and a standard deviation of 4.94×10^{-5} cm based on a log normal distribution. The "correct" distribution shown in Figure A.1b has a mean of 3.38×10^{-4} cm and a standard deviation of 1.22×10^{-4} cm. At the threshold pressure gradient, the open throats have an average radius of 5.46×10^{-4} cm which is (as expected) larger than the average radius of the network, but some throats on the threshold path are smaller than the average.

The distributions for the sandstone show a log-normal mean of 9.55×10^{-4} cm and a standard deviation of 5.04×10^{-4} cm in Figure A.2a, but a correct, converted mean radius of 2.44×10^{-3} cm and standard deviation of 2.51×10^{-3} cm. At the threshold pressure gradient, the open throats have an average radius of 8.55×10^{-3} cm which is again larger than the average radius of the network.

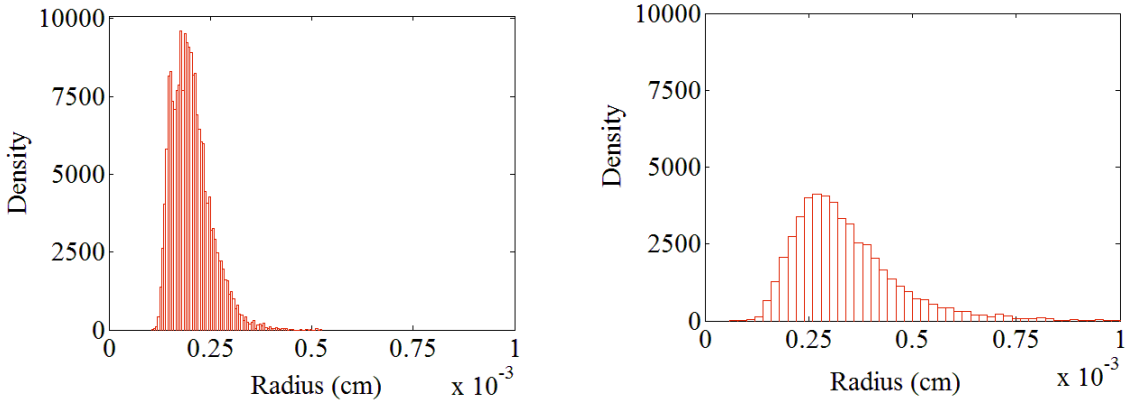

(a) (b)

Figure A.1 Throat radius distributions in the sphere pack using (a) a simple method of radii that give correct hydraulic conductivity and pore-to-pore distance and (b) a method used here based on FEM correlations in Balhoff and Thompson (2004). Permeability of both medium is equal to 9.88×10^{-10} cm^2 (100mD).

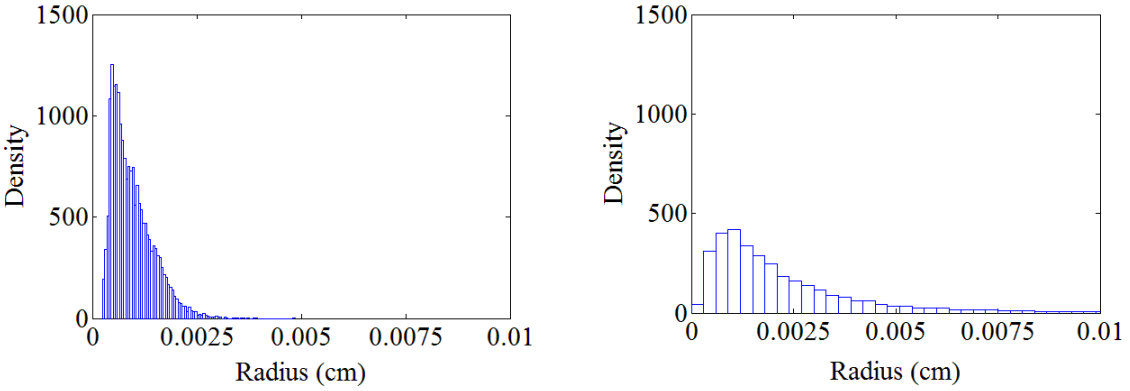

(a) (b)

Figure A.2 Throat radius distributions in the sandstone using (a) a simple method of radii that give correct hydraulic conductivity and pore-to-pore distance and (b) a method used here based on FEM correlations in Balhoff and Thompson (2004). Permeability of both medium is equal to 9.88×10^{-10} cm^2 (100mD).

Appendix B: The Matrix Equation of the Pore-Network Model

Lamella flow through a pore throat is represented by the lamella flow equation (Eq. B.1) with one of the apparent gas (lamella) viscosity models in Table 4.1 in Chapter 4.

$$if\ (\Delta P)_{i,j} > (\Delta P_m)_{i,j}\ \ ;\ \ q_{i,j} = \frac{g_{i,j}}{(\mu_{app})_{i,j}}\left[(\Delta P)_{i,j} - (\Delta P_m)_{i,j}\right] \tag{B.1a}$$

$$if\ (\Delta P)_{i,j} \le (\Delta P_m)_{i,j}\ \ ;\ \ q_{i,j} = 0 \tag{B.1b}$$

where q is flow rate in a pore throat, g is hydraulic conductivity of a pore throat, μ_{app} is apparent gas (lamella) viscosity, ΔP is pressure difference across a pore throat, ΔP_m is mobilization pressure difference across a pore throat. The subscript i,j corresponds to the pore throat connecting pore i to pore j.

If there is no lamella in a pore throat, then the gas flow is represented by the Newtonian flow equation with an assumption that gas compressibility is negligible (Eq. B.2). This assumption is valid for small pressure gradient as compared to the system pressure

$$q_{i,j} = \frac{g_{i,j}}{\mu_g}\left[(\Delta P)_{i,j}\right] \tag{B.2}$$

Modeling flow in the network requires ensuring mass balance at every pore i (Eq. B.3); this leads to a system of N equations (N being the number of pores), where pore pressures are the unknowns.

$$\sum_j q_{i,j} = 0 \tag{B.3}$$

The local pressure field in a pore network with N pores could be obtained from the solution of Eq B.4. The general form of the matrix equation is composed of Newtonian gas and Non-Newtonian lamella flow equations at a specific overall lamella density. The resulting system of equations can be solved to determine the pore pressures in the network and the total flow rate (or velocity) for an applied pressure gradient in one direction. The fluid flow equations representing a lamella flow through a capillary tube in Table 4.2 in Chapter 4 are nonlinear, so the elements in the matrix equation may not be constants. Therefore, a multidimensional Newton-Raphson scheme is used to solve the system of equations.

$$\underbrace{\begin{bmatrix} \left(-\sum_j \frac{g_{1,j}}{\mu_{1,j}}\right) & A_{1,2} & \cdots & A_{1,N} \\ A_{2,1} & \left(-\sum_j \frac{g_{2,j}}{\mu_{2,j}}\right) & & \vdots \\ \vdots & & \ddots & A_{(N-1),N} \\ A_{N,1} & \cdots & A_{N,(N-1)} & \left(-\sum_j \frac{g_{N,j}}{\mu_{N,j}}\right) \end{bmatrix}}_{\text{Matrix A}_{N\times N}} \times \begin{bmatrix} P_1 \\ P_2 \\ \vdots \\ P_N \end{bmatrix}_{N\times 1} = \underbrace{\begin{bmatrix} \left(\sum_j B_{1,j}\right) - C_1 \\ \left(\sum_j^{T2} B_{2,j}\right) - C_2 \\ \vdots \\ \left(\sum_j B_{N,j}\right) - C_N \end{bmatrix}}_{\text{Vector B}_{N\times 1}} \tag{B.4a}$$

$$\mu_{i,j} = \begin{cases} \left(\mu_{app}\right)_{i,j} & \text{, with lamella} \\ \mu_g & \text{, no lamella} \end{cases} \qquad \left(\mu_{app}\right)_{i,j} = \begin{cases} \text{Constant} \\ \text{Power-law} \\ \text{Hirasaki-Lawson (1985)} \end{cases} \tag{B.4b}$$

$$B_{i,j} = \begin{cases} \dfrac{g_{i,j}\left(\Delta P_m\right)_{i,j}}{\left(\mu_{app}\right)_{i,j}} & \text{, with lamella} \\ 0 & \text{, no lamella} \end{cases} \tag{B.4c}$$

$$C_i = \begin{cases} \left(\dfrac{g_{i,in}}{\mu_{i,in}}\right) P_{in} & \text{, inlet constant pressure boundary} \\ \left(\dfrac{g_{i,out}}{\mu_{i,out}}\right) P_{out} & \text{, outlet constant pressure boundary} \\ 0 & \text{, no boundary} \end{cases} \tag{B.4d}$$

where, P_{in} and P_{out} are inlet and outlet boundary pressures of the pore-network, respectively. The off-diagonal terms in Matrix A are:

$$A_{i,j} = \begin{cases} \dfrac{g_{i,j}}{\mu_{i,j}} & \text{, with pore throat} \\ 0 & \text{, no pore throat} \end{cases} \tag{B.4e}$$

Appendix C: Heterogeneous Distribution of Lamellas in the Network

In addition to the homogeneous distribution of lamellas in the pore network, five different heterogeneous distributions of lamellas are tested in the flow simulations in Chapter 4 (Figure 4.7) for overall lamella densities of 0.4 (Figure C.1) and 0.8 (Figure C.2). Pore network is divided by 3×3×3 grids. In Figure C.1, the pore throats located in white grids are occupied by one lamella; however the pore throats in the transparent grids have no lamella. In Figure C.2, however, the pore throats located in transparent grids are occupied by one lamella.

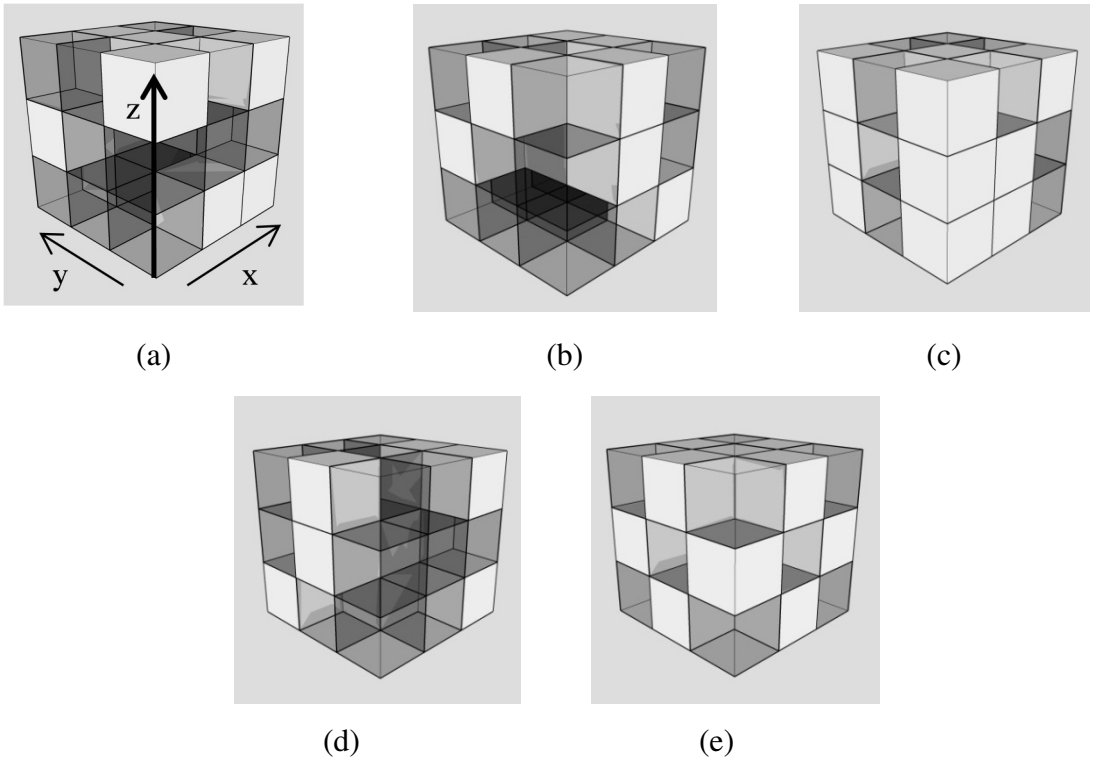

Figure C.1 Schematic showing the five different heterogeneous distributions of lamellas in Figure 4.7a in Chapter 4. The pore-network is divided by 3×3×3 grids and the overall lamella density, ρ_t^L is equal to 0.4. All pore throats located in white grids are occupied by a lamella; the pore throats in the transparent grids have no lamella. Fluid flow is in the z-direction.

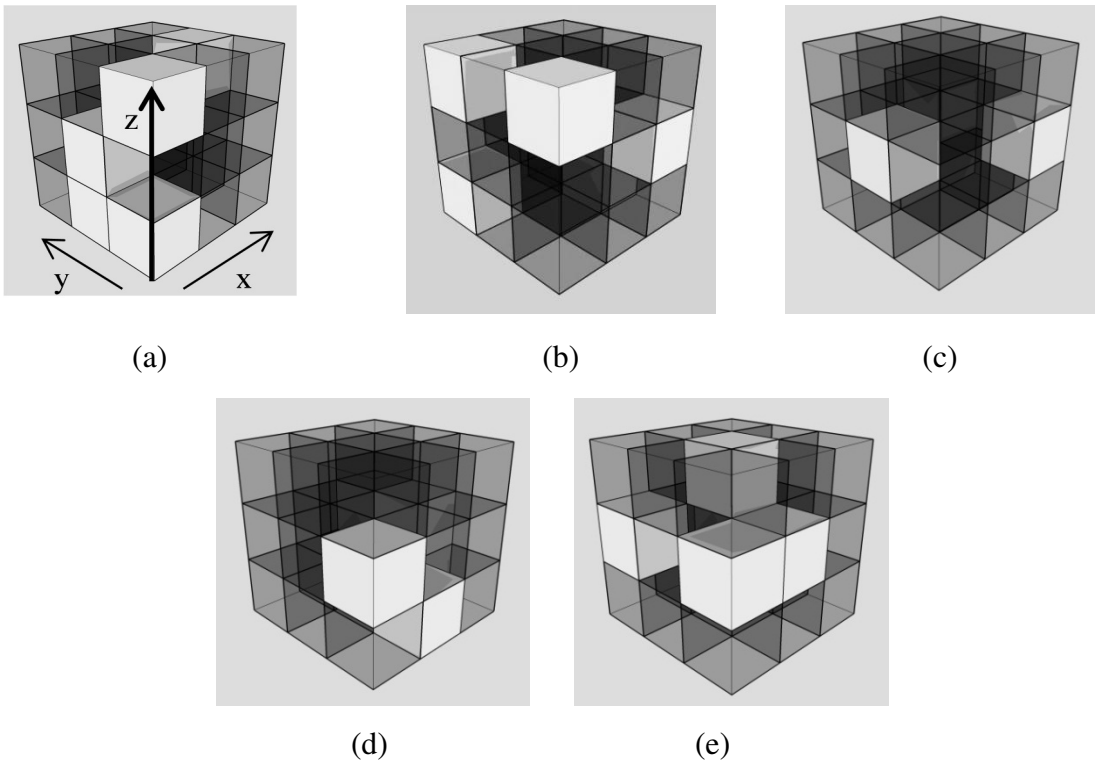

Figure C.2 Schematic showing the five different heterogeneous distributions of lamellas in Figure 4.7b in Chapter 4. The pore-network is divided by 3×3×3 grids and the overall lamella density, ρ_t^L is equal to 0.8. All pore throats located in transparent grids are occupied by a lamella; the pore throats in the white grids have no lamella. Fluid flow is in the z-direction.

Appendix D: Discretization of the Material Balance Equations

Material balance equations for water and gas phases:

$$\frac{\partial}{\partial t}\left(\frac{\phi S_w}{B_w}\right)+\frac{\partial}{\partial x}\left(\frac{u_w}{B_w}\right)=Q_w \tag{D.1a}$$

$$\frac{\partial}{\partial t}\left(\frac{\phi S_g}{B_g}\right)+\frac{\partial}{\partial x}\left(\frac{u_g}{B_g}\right)=Q_g \tag{D.1b}$$

1D Darcy flow equations for water and gas phases:

$$u_w=-\frac{kk_{rw}}{\mu_w}\frac{\partial P_w}{\partial x} \tag{D.2a}$$

$$u_g=-\frac{kk_{rg}}{\mu_g}\frac{\partial P_g}{\partial x} \tag{D.2b}$$

Since both water and gas phases exist in the porous media:

$$S_w+S_g=1.0 \tag{D.3}$$

After substituting Darcy flow equations into material balance equations:

$$\frac{\partial}{\partial x}\left[\frac{kk_{rw}}{\mu_w B_w}\frac{\partial P_w}{\partial x}\right]=\frac{\partial}{\partial t}\left(\phi\frac{S_w}{B_w}\right)-Q_w \tag{D.4a}$$

$$\frac{\partial}{\partial x}\left[\frac{kk_{rg}}{\mu_g B_g}\frac{\partial P_g}{\partial x}\right]=\frac{\partial}{\partial t}\left(\phi\frac{S_g}{B_g}\right)-Q_g \tag{D.4b}$$

After summation of D.4a and D.4b without source/sink term (Q_w=0; Q_g=0):

$$\begin{aligned}&B_g\frac{\partial}{\partial x}\left(\frac{kk_{rg}}{\mu_g B_g}\frac{\partial P_g}{\partial x}\right)+B_w\frac{\partial}{\partial x}\left(\frac{kk_{rw}}{\mu_w B_w}\frac{\partial P_g}{\partial x}\right)\\&-B_w\frac{\partial}{\partial x}\left(\frac{kk_{rw}}{\mu_w B_w}\frac{\partial P_c}{\partial x}\right)=\phi\left(S_g c_g+S_w c_w\right)\frac{\partial P_g}{\partial t}\end{aligned} \tag{D.5}$$

Transmissibility of phase θ in grid i and at time step d is defined as:

$$T_{\theta,i}^{d} = \left(\frac{kk_{r\theta}}{\mu_{\theta} B_{\theta}} \right)_{i}^{d} \tag{D.6}$$

Using the IMPES scheme with upstream mobility weighting:

$$T_{\theta,i+1/2}^{d} = T_{\theta,i}^{d} \tag{D.7a}$$

$$T_{\theta,i-1/2}^{d} = T_{\theta,i-1}^{d} \tag{D.7b}$$

After discretizing the terms in Eq. D.5:

$$B_{g,i}^{d} \frac{\partial}{\partial x} \left(T_{g,i}^{d} \frac{\partial P_{g}^{d+1}}{\partial x} \right) \approx B_{g,i}^{d} \left(\frac{T_{g,i}^{d} \left(\frac{P_{g,i+1}^{d+1} - P_{g,i}^{d+1}}{\Delta x} \right) - T_{g,i-1}^{d} \left(\frac{P_{g,i}^{d+1} - P_{g,i-1}^{d+1}}{\Delta x} \right)}{\Delta x} \right) \tag{D.8a}$$

$$B_{w,i}^{d} \frac{\partial}{\partial x} \left(T_{w,i}^{d} \frac{\partial P_{g}^{d+1}}{\partial x} \right) \approx B_{w,i}^{d} \left(\frac{T_{w,i}^{d} \left(\frac{P_{g,i+1}^{d+1} - P_{g,i}^{d+1}}{\Delta x} \right) - T_{w,i-1}^{d} \left(\frac{P_{g,i}^{d+1} - P_{g,i-1}^{d+1}}{\Delta x} \right)}{\Delta x} \right) \tag{D.8b}$$

$$B_{w,i}^{d} \frac{\partial}{\partial x} \left(T_{w,i}^{d} \frac{\partial P_{c}^{d+1}}{\partial x} \right) \approx B_{w,i}^{d} \left(\frac{T_{w,i}^{d} \left(\frac{P_{c,i+1}^{d+1} - P_{c,i}^{d+1}}{\Delta x} \right) - T_{w,i-1}^{d} \left(\frac{P_{c,i}^{d+1} - P_{c,i-1}^{d+1}}{\Delta x} \right)}{\Delta x} \right) \tag{D.8c}$$

$$\frac{\partial P_{g,i}}{\partial t} \approx \frac{P_{g,i}^{d+1} - P_{g,i}^{d}}{\Delta t} \tag{D.8d}$$

Therefore, the discretized Eq. D.5 becomes:

$$
\begin{aligned}
&B_{g,i}^{d}\left(\frac{T_{g,i}^{d}\left(P_{g,i+1}^{d+1}-P_{g,i}^{d+1}\right)-T_{g,i-1}^{d}\left(P_{g,i}^{d+1}-P_{g,i-1}^{d+1}\right)}{\Delta x^{2}}\right)\\
&+B_{w,i}^{d}\left(\frac{T_{w,i}^{d}\left(P_{g,i+1}^{d+1}-P_{g,i}^{d+1}\right)-T_{w,i-1}^{d}\left(P_{g,i}^{d+1}-P_{g,i-1}^{d+1}\right)}{\Delta x^{2}}\right)\\
&-B_{w,i}^{d}\left(\frac{T_{w,i}^{d}\left(P_{c,i+1}^{d}-P_{c,i}^{d}\right)-T_{w,i-1}^{d}\left(P_{c,i}^{d}-P_{c,i-1}^{d}\right)}{\Delta x^{2}}\right)=\phi\left(S_{g}c_{g}+S_{w}c_{w}\right)_{i}^{d}\frac{P_{g,i}^{d+1}-P_{g,i}^{d}}{\Delta t}
\end{aligned}
\tag{D.9}
$$

After rearranging Eq. D.9:

$$
\begin{aligned}
&P_{g,i-1}^{d+1}\left(B_{g,i}^{d}T_{g,i-1}^{d}+B_{w,i}^{d}T_{w,i-1}^{d}\right)\\
&-P_{g,i}^{d+1}\left(B_{g,i}^{d}\left[T_{g,i}^{d}+T_{g,i-1}^{d}\right]+B_{w,i}^{d}\left[T_{w,i}^{d}+T_{w,i-1}^{d}\right]+\phi\left(S_{g}c_{g}+S_{w}c_{w}\right)_{i}^{d}\frac{\Delta x^{2}}{\Delta t}\right)\\
&+P_{g,i+1}^{d+1}\left(B_{g,i}^{d}T_{g,i}^{d}+B_{w,i}^{d}T_{w,i}^{d}\right)=\\
&B_{w,i}^{d}\left(T_{w,i}^{d}\left[P_{c,i+1}^{d}-P_{c,i}^{d}\right]-T_{w,i-1}^{d}\left[P_{c,i}^{d}-P_{c,i-1}^{d}\right]\right)-\phi\frac{\Delta x^{2}}{\Delta t}\left(S_{g}c_{g}+S_{w}c_{w}\right)_{i}^{d}P_{g,i}^{d}
\end{aligned}
\tag{D.10}
$$

Constant-rate water ($\theta = w$) and gas ($\theta = g$) injection boundary:

$$
T_{\theta}\frac{\partial P_{\theta}}{\partial x}=-Q_{\theta}\rightarrow P_{\theta,1}-P_{\theta,0}\approx-\frac{Q_{\theta}}{T_{\theta,1}}\Delta x \tag{D.11a}
$$

$$
\begin{aligned}
P_{c,1}^{d}-P_{c,0}^{d}&=\left(P_{g,1}^{d}-P_{g,0}^{d}\right)-\left(P_{w,1}^{d}-P_{w,0}^{d}\right)\\
&=-\frac{Q_{g}}{T_{g,1}^{d}}\Delta x+\frac{Q_{w}}{T_{w,1}^{d}}\Delta x\quad\text{with}\quad T_{\theta,0}^{d}=T_{\theta,1}^{d}
\end{aligned}
\tag{D.11b}
$$

Constant-pressure production boundary:

$$
P_{\theta,N_{x}+1}-P_{\theta,N_{x}}\approx 2\left(P_{out}-P_{\theta,N_{x}}\right) \tag{D.12a}
$$

$$
P_{c,N_{x}+1}^{d}=0 \tag{D.12b}
$$

After substituting the boundary conditions to Eq. D.10, the injection sided equation ($i = 1$) becomes:

$$\begin{aligned}
&-P_{g,1}^{d+1}\left(B_{g,1}^{d}T_{g,1}^{d}+B_{w,1}^{d}T_{w,1}^{d}+\phi\left(S_g c_g+S_w c_w\right)_1^d\frac{\Delta x^2}{\Delta t}\right)\\
&+P_{g,2}^{d+1}\left(B_{g,1}^{d}T_{g,1}^{d}+B_{w,1}^{d}T_{w,1}^{d}\right)=\\
&B_{w,1}^{d}T_{w,1}^{d}\left(P_{c,2}^{d}-P_{c,1}^{d}\right)-B_{g,1}^{d}Q_g\Delta x-B_{w,1}^{d}Q_w\Delta x-\phi\frac{\Delta x^2}{\Delta t}\left(S_g c_g+S_w c_w\right)_1^d P_{g,1}^{d}
\end{aligned} \tag{D.13}$$

And the production sided equation becomes ($i = N_x$):

$$\begin{aligned}
&P_{g,N_x-1}^{d+1}\left(B_{g,N_x}^{d}T_{g,N_x-1}^{d}+B_{w,N_x}^{d}T_{w,N_x-1}^{d}\right)\\
&-P_{g,N_x}^{d+1}\left(B_{g,N_x}^{d}\left[2T_{g,N_x}^{d}+T_{g,N_x-1}^{d}\right]+B_{w,N_x}^{d}\left[2T_{w,N_x}^{d}+T_{w,N_x-1}^{d}\right]+\phi\left(S_g c_g+S_w c_w\right)_{N_x}^d\frac{\Delta x^2}{\Delta t}\right)\\
&=B_{w,N_x}^{d}\left(-T_{w,N_x}^{d}P_{c,N_x}^{d}-T_{w,N_x-1}^{d}\left[P_{c,N_x}^{d}-P_{c,N_x-1}^{d}\right]\right)-\phi\frac{\Delta x^2}{\Delta t}\left(S_g c_g+S_w c_w\right)_{N_x}^d P_{g,N_x}^{d}\\
&-2P_{out}\left(B_{g,N_x}^{d}T_{g,N_x}^{d}+B_{w,N_x}^{d}T_{w,N_x}^{d}\right)
\end{aligned} \tag{D.14}$$

Updating Saturations:

$$S_{g,i}^{d+1}=B_{g,i}^{d+1}\left(\frac{\Delta t}{\phi\Delta x^2}\left(T_{g,i}^{d}\left[P_{g,i+1}^{d+1}-P_{g,i}^{d+1}\right]-T_{g,i-1}^{d}\left[P_{g,i}^{d+1}-P_{g,i-1}^{d+1}\right]\right)+\frac{S_{g,i}^{d}}{B_{g,i}^{d}}\right) \tag{D.15}$$

Injection Sided Grid Block:

$$S_{g,1}^{d+1}=\frac{\Delta t}{\phi\Delta x^2}B_{g,1}^{d+1}T_{g,1}^{d}\left(P_{g,2}^{d+1}-P_{g,1}^{d+1}\right)+\frac{\Delta t}{\phi\Delta x}B_{g,1}^{d+1}Q_g+B_{g,1}^{d+1}\frac{S_{g,1}^{d}}{B_{g,1}^{d}} \tag{D.16}$$

Production Sided Grid Block:

$$S_{g,N_x}^{d+1}=\frac{2\Delta t}{\phi\Delta x^2}B_{g,N_x}^{d+1}T_{g,N_x}^{d}\left(P_{out}-P_{g,N_x}^{d+1}\right)-\frac{\Delta t}{\phi\Delta x^2}B_{g,N_x}^{d+1}T_{g,N_x-1}^{d}\left(P_{g,N_x}^{d+1}-P_{g,N_x-1}^{d+1}\right)+B_{g,N_x}^{d+1}\frac{S_{g,N_x}^{d}}{B_{g,N_x}^{d}} \tag{D.17}$$

Nomenclature

a = model parameter in Eq. 5.11

A = empirical exponent in Eq. 2.10

b = model parameter in Eq. 5.11

B = empirical exponent in Eq. 2.11

B_w = water formation volume factor

B_g = gas formation volume factor

c_A = cross-sectional area, L^2

c_w = coefficient of isothermal compressibility of water, $m^{-1}L^1t^2$

c_g = coefficient of isothermal compressibility of gas, $m^{-1}L^1t^2$

c_1 = rate constant for lamella generation, $t^{1/3}L^{-13/3}$

c_1^o = reference rate constant for lamella generation, $t^{1/3}L^{-13/3}$

c_{-1} = rate constant for lamella coalescence, L^{-1}

c_{-1}^o = reference rate constant for lamella coalescence, L^{-1}

e_g = exponent of gas relative permeability without foam

e_w = exponent of water relative permeability

f_1 = model parameter in Eq. 5.3

f_2 = model parameter in Eq. 5.5

f_g = fractional flow of gas

f_g^* = critical fractional flow of gas

g = hydraulic conductivity of a pore throat, L^3

G_L = net lamella generation term, $L^{-3}t^{-1}$

h = film thickness, L

H = parameter in Eq.2.12

k = permeability, L^2

k_r = pressure-gradient dependent relative permeability

k_{rg}^{f} = gas relative permeability with foam

k_{rg}^{*} = gas relative permeability without foam

k_{rg}^{o} = end-point of gas relative permeability without foam

k_{rw} = water relative permeability

k_{rw}^{o} = end-point of water relative permeability

k_D = dimensionless permeability

L = length of a pore throat, L

L_c = characteristic pore-throat length of the pore network, L

L_x = core length, L

$(L_c)_D$ = dimensionless characteristic pore-throat length of the pore network

L_{pn} = length of the pore-network model, L

M_{par} = history matching parameter

n = shear-thinning index

n_{fg}^{L} = number of flowing lamella per unit volume of flowing gas, L^{-3}

$(n_{fg}^{L})^{eq}$ = number of flowing lamella per unit volume of flowing gas at local equilibrium, L^{-3}

n_{fg}^{L*} = maximum number of flowing lamella per unit volume of flowing gas, L^{-3}

n_{tg}^{L} = number of trapped lamella per unit volume of trapped gas, L^{-3}

n_t^{L} = number of lamellas per unit gas volume, L^{-3}

$(n_t^{L})_D$ = dimensionless n_t^{L}

N = number of pores in the pore-network

N_c = capillary number

N^L = total number of lamellas in the pore network

N^T = total number of pore throats in the pore network

N_{fg}^{L} = the number of flowing lamellas

N_{tg}^{L} = the number of trapped lamellas

N_{fg}^{T} = the number of pore throats in flowing gas domain

N_{tg}^{T} = the number of pore throats in trapped gas domain

N_x = number of grids in the x-direction

p_1 = model parameter in Eq. 5.15

p_2 = model parameter in Eq. 5.15

P = pressure, $mL^{-1}t^{-2}$

P_w = pressure of water phase, $mL^{-1}t^{-2}$

P_g = pressure of gas phase, $mL^{-1}t^{-2}$

P_c = capillary pressure, $mL^{-1}t^{-2}$

P_c^* = critical capillary pressure, $mL^{-1}t^{-2}$

P_{in} = inlet boundary pressure, $mL^{-1}t^{-2}$

P_{out} = outlet boundary pressure, $mL^{-1}t^{-2}$

ΔP = pressure difference in a pore throat, $mL^{-1}t^{-2}$

ΔP_m = mobilization pressure difference across a pore throat, $mL^{-1}t^{-2}$

∇P = pressure gradient, $mL^{-2}t^{-2}$

∇P_M = threshold pressure gradient, $mL^{-2}t^{-2}$

∇P_D = dimensionless pressure gradient

∇P_T = dimensionless threshold pressure gradient

∇P_T^* = dimensionless pressure gradient intercept in macroscopic model

q = flow rate in a pore throat, L^3t^{-1}

Q_g = gas injection rate, L^3t^{-1}

Q_w = water injection rate, L^3t^{-1}

Q_L = lamella source/sink term, $L^{-3}t^{-1}$

r_c = radius of curvature of a lamella, L

$\overline{r_g}$ = mean of grain radius, L

R = pore-throat radius, L

$\overline{R}$ = log-normal mean of pore-throat radius, L

R_c = coalescence rate per unit gas volume, $L^{-3}t^{-1}$

R_g = lamella generation rate per unit gas volume, $L^{-3}t^{-1}$

$\overline{R}_D$ = dimensionless log-normal mean of pore-throat radius, L

S_g = gas saturation

S_{gn} = normalized gas saturation

S_{gr} = residual gas saturation

S_w = water saturation

S_w^* = critical water saturation

$(S_w)_{avg}$= average water saturation

S_{wc} = connate water saturation

S_{wi} = initial water saturation

S_{wn} = normalized water saturation

S_{fg} = flowing gas saturation

S_{tg} = trapped gas saturation

t = time, t

T_w = water transmissibility, $m^{-1}L^3t$

T_g = gas transmissibility, $m^{-1}L^3t$

u = superficial (Darcy) velocity, Lt^{-1}

u_g = superficial (Darcy) gas velocity, Lt^{-1}

u_w = superficial (Darcy) water velocity, Lt^{-1}

u_g^f = Superficial (Darcy) gas velocity with foam, Lt^{-1}

u_D = dimensionless superficial (Darcy) velocity

v_g^f = interstitial gas velocity with foam , Lt^{-1}

v_w = interstitial water velocity , Lt^{-1}

V_g = total gas volume, L^3

V_{fg} = flowing gas volume, L^3

V_{tg} = trapped gas volume, L^3

w = model parameter in Eq. 2.5

x = distance in the x-direction, L

x_D = dimensionless distance in the x-direction

x_1 = model parameter in Eq. 5.4

x_2 = model parameter in Eq. 5.4

X_{fg} = flowing gas fraction

y_1 = model parameter in Eq. 5.6

y_2 = model parameter in Eq. 5.6

ϕ = porosity

δ = wetting layer thickness, L

λ_g^f = foamed gas mobility, $m^{-1}L^3t$

α = model parameter in Eq. 2.9

ξ = retardation factor

γ = gas-water interfacial tension, mt^{-2}

β = constant for shear-thinning flow in porous media

β_r = pressure-gradient dependent variable in macroscopic model

σ_R = log-normal standard deviation of pore-throat radius, L

$(\sigma_R)_D$ = dimensionless log-normal standard deviation of pore-throat radius

τ_o = yield stress, or apparent yield stress for foam, $mL^{-1}t^{-2}$

τ_w = shear stress at throat wall, $mL^{-1}t^{-2}$

ρ_t^L = total number of lamellas normalized to the number of pore throats in the pore network

ρ_{fg}^L = the number of flowing lamellas normalized to the number of pore throats in flowing gas domain

ρ_{tg}^L = the number of trapped lamellas normalized to the number of pore throats in trapped gas domain

μ_g^f = effective gas viscosity, $mL^{-1}t^{-1}$

μ_g = gas viscosity, $mL^{-1}t^{-1}$

μ_{app} = pore-scale apparent gas (lamella) viscosity, $mL^{-1}t^{-1}$

μ = viscosity, $mL^{-1}t^{-1}$

μ_o = consistency index, $mL^{-1}t^{n-2}$

μ_w = viscosity of water, $mL^{-1}t^{-1}$

Π = disjoining pressure, $mL^{-1}t^{-2}$

Π_{EL} = repulsive electrostatic pressure, $mL^{-1}t^{-2}$

Π_{VW} = attractive Van der Waals pressure, $mL^{-1}t^{-2}$

References

Alvarez, J.M., Rivas, H., and Rossen, W.R. 2001. A Unified Model for Steady-State Foam Behavior at High and Low Foam Qualities. *SPE J.* **6**: 325-333.

Al-Fariss, T., and Pinder, K.L. 1987. Flow through Porous Media of a Shear-Thinning Liquid with a Yield Stress. *Can. J. Chem. Eng.* **69**(3): 391-405.

Al-Raoush, R., Thompson, K.E., and Willson, C.S. 2003. Comparison of Network Generation Techniques for Unconsolidated Porous Media. *Soil Sci. Soc. Am. J.* **67**(6): 1687-1700.

Andrianov, A., Farajzadeh, R., Nick, M.M., et al. 2011. Immiscible Foam for Enhancing Oil Recovery: Bulk and Porous Media Experiments. Paper SPE 143578 presented at Enhanced Oil Recovery Conference, Kuala Lumpur, Malaysia, 19-21 July.

Aronson, A.S., Bergeron, V., Fagan, M., et al. 1994. The Influence of Disjoining Pressure on Foam Stability and Flow in Porous Media. *Coll. Surf. A.: Physicochem. Eng. Aspects* **83**: 109-120.

Ashoori, E., Marchesin, D., and Rossen, W.R. 2011. Roles of Transient and Local Equilibrium Foam Behavior in Porous Media: Travelling Wave. *Colloids Surf. A* **377**: 228-242.

Balan, H.O., Balhoff, M.T., Nguyen, Q.P., et al. 2011a. Network Modeling of Gas Trapping and Mobility in Foam Enhanced Oil Recovery. *Energy&Fuels* **25**: 3974-3987.

Balan, H.O., Balhoff, M.T., Nguyen, Q.P., et al. 2011b. Modeling Gas Trapping and Mobility in Foam EOR. Presented at the 16th European Symposium on Improved Oil Recovery in Cambridge, UK, 12-14 April.

Balan, H.O., Balhoff, M.T., Nguyen, Q.P., 2012. Modeling of Foamed Gas Mobility in Porous Media. Presented at the 18th SPE Improved Oil Recovery Symposium in Tulsa, OK, 14-18 April.

Balhoff, M.T., and Thompson, K.A. 2004. Modeling the Steady Flow of Yield-Stress Fluids in Packed Beds. *AIChE J.* **50**(12): 3034-3048.

Balhoff, M.T., and Thompson, K.A. 2006. Macroscopic Model for Shear-Thinning Flow in Packed Beds Based on Network Modeling. *Chem. Eng. Sci.* **61**(2): 698-719.

Balhoff, M.T., Sanchez-Rivera, D., Kwok, A., et al. 2012. Numerical Algorithms for Network Modeling of Yield Stress and other Non-Newtonian Fluids in Porous Media. *Transport in Porous Media* **93**(3): 363-379.

Bernard, G.G., and Holm, L.W. 1964. Effect of Foam on Permeability of Porous Media to Gas. *SPE J.* **4**(3): 267-274.

Bernard, G.G., Holm, L.W., and Jacobs, W.L. 1965. Effect of Foam on Trapped Gas Saturation and on Permeability of Porous Media to Water. *SPE J.* **5**(4): 295-300.

Bertin, H.J., Apaydin, O.G., Castanier, L.M., et al. 1999. Foam Flow in Heterogeneous Porous Media: Effect of Cross Flow. *SPE J.* **4**(2): 75-82.

Bertin, H.J. 2000. Foam Diversion Modeling Using a Bubble-Population Correlation. Paper SPE 59366 presented at the SPE/DOE Symposium on Improved Oil Recovery, Tulsa, OK, 3-5 April.

Bird, R.B., Stewart, W.E., and Lightfoot, E.N. 2007. *Transport Phenomena*, revised, 2nd ed. New York: John Wiley & Sons Inc.

Bretherton, F.P. 1961. The Motion of Long Bubbles in Tubes. *J. Fluid Mech*. **10**: 166-188.

Chase, G., and Dachavijit, P. 2003. Incompressible Cake Filtration of a Yield Stress Fluid. *Sep. Sci. Technol.* **38**(4): 745-766.

Chen, Q. 2009. Assessing and Improving Steam-Assisted Gravity Drainage: Reservoir Heterogeneities, Hydraulic Fractures, and Mobility Control Foams. PhD. Dissertation, Stanford University, 197 pages.

Chen, Q., Gerritsen, M.G., and Kovscek, A.R. 2010. Modeling Foam Displacement with the Local-Equilibrium Approximation: Theory and Experimental Verification. *SPE J.* **15**(1): 171-183.

Chen, M., Rossen, W.R., and Yortsos, Y.C. 2005a. The Flow and Displacement in Porous Media of Fluids with Yield Stress. *Chem. Eng. Sci.* **60**(15), 4183-4202.

Chen, M., Yortsos, Y.C., and Rossen, W.R. 2005b. Insights of Foam Generation in Porous Media from Pore-network Studies. *Colloids and Surfaces A: Physicochem Eng. Aspects* **256:** 181-189.

Cheng, L., Reme, A.B., Shan, D., et al. 2000. Simulating Foam Processes at High and Low Foam Qualities. Paper SPE 59287 presented at the SPE/DOE Symposium on Improved Oil Recovery, Tulsa, OK, 3-5 April.

Cheng, L., Kam, S.I., Delshad, M., et al. 2002. Simulation of Dynamic Foam-Acid Diversion Processes. *SPE J.* **7**: 316-324.

Chou, S.I., 1990. Percolation Theory of Foam in Porous Media. Paper SPE 20239 presented at SPE/DOE Seventh Symposium on Enhanced Oil Recovery, Tulsa, OK, 22-25 April.

Christopher, R.H., and Middleman, S. 1965. Power-law flow through a packed tube. *Ind. Eng. Chem. Fundam.* **4**: 422-426.

Cohen, D., Patzek, T.W., and Radke, C.J. 1997. Onset of Mobilization and the Fraction of Trapped Foam in Porous Media. *Transport in Porous Media* **28**: 253-284.

Cox, S.J., Neethling, S., Rossen, W.R., et al. 2004. A Theory of the Effective Yield Stress of Foam in Porous Media: The Motion of a Soap Film Traversing a Three-Dimensional Pore. *Colloids Surf., A: Physicochem Eng. Aspects* **245**: 143-151.

Derjaguin, B.V., and Landau, L. 1941. Theory of the Stability of Strongly Charged Lyophobic Sols and of the Adhesion of Strongly Charged Particles in Solutions of Electrolytes. *Acta Physicochim. U.S.S.R.* **14**: 633-662.

Ettinger, R.A., and Radke, C.J. 1992. Influence of Texture on Steady Foam Flow in Berea Sandstone. *SPE Reservoir Engineering* **7**(1):83-90.

Exerowa, D., and Kruglyakov, P.M. 1998. *Foam and Foam Films: Theory, Experiment , Application*, eds. Mobius, D., and Miller, R.S., Amsterdam, the Netherlands: Elsevier Science.

Falls, A.H., Hirasaki, G.J., Patzek, T.W., et al. 1988. Development of a Mechanistic Foam Simulator: The Population Balance and Generation by Snap-Off. *SPE Reservoir Eval. Eng.* **3**(3): 884-892.

Falls, A.H., Musters, J.J., Ratulowski, J. 1989. The Apparent Viscosity of Foams in Homogeneous Bead Packs. *SPE Reservoir Eval. Eng.* **4**(2), 155-264.

Farajzadeh, R., Krastev, Y., and Zitha, P.L.J. 2008. Foam Film Permeability: Theory and Experiment. *Adv. in Colloid and Interface Sci.* **137**: 27-44.

Fisher, A.W., Foulser, R.W.S., and Goodyear, S.G. 1990. Mathematical Modeling of Foam Flooding. Paper SPE 20195 presented at the SPE/DOE Symposium on Enhanced Oil Recovery, Tulsa, OK, 22-25 April.

Friedmann, F., Chen, W.H., and Gauglitz, P.A. 1991. Experimental and Simulation Study of High-Temperature Foam Displacement in Porous Media. *SPE Reservoir Eval. Eng.* **6**(1): 37-45.

Gani, M.R., and Bhattacharya, J.P. 2003. Bed-Scale Facies Architecture of an Ancient Delta Lobe Deposit of the Wall Creek Member, Central Wyoming, U.S.A. Presented at the AAPG Annual Convention & Exhibition, Salt Lake City, UT,11-14 May.

Gdanski, R.D. 1993. Experience and Research Show Best Designs for Foam-Diverted Acidizing. *Oil Gas J.* **91**(36): 85-89.

Green, D.W., and Willhite, G.P. 1998. *Enhanced Oil Recovery*, Richardson, Texas: Society of Petroleum Engineers.

Heller, J.P., and Kuntamukkula, M.S. 1987. Critical Review of the Foam Rheology Literature. *Ind. Eng. Chem. Res.* **26**: 318-325.

Hirasaki, G.J., and Lawson, J.B. 1985. Mechanisms of Foam Flow in Porous Media: Apparent Viscosity in Smooth Capillaries. *SPE J.* **25**(2): 176-190.

Hirasaki, G.J., Jackson, R.E., Jin, C., et al. 2000. Field Demonstration of the Surfactant/Foam Process for Remediation of a Heterogeneous Aquifer Contaminated with DNAPL. In *NAPL Removal: Surfactants, Foams, and Microemulsions*, eds. Fiorenza, S., Miller, C.A., Oubre, C.L., et al., Boca Raton, FL: Lewis Publishers.

Holm, L.W., 1968. The Mechanism of Gas and Liquid Flow through Porous Media in the Presence of Foam. *SPE J.* **8**(4): 359-369.

Huh, D.G., and Handy, L.L. 1989. Comparison of Steady State and Unsteady-State Flow of Gas and Foaming Solution in Porous Media. *SPE Reservoir Engineering* **4**(1): 77-84.

Jodrey, W.S., and Tory, E.M. 1985. Computer Simulation of Close Random Packing of Equal Spheres. *Phys. Rev. A.* **32**(4): 2347-2351.

Kam, S.I., and Rossen, W.R. 2003. A Model for Foam Generation in Homogeneous Media. *SPE J.* **8**(4): 417-425.

Kam, S.I., Nguyen, Q.P., Rossen, W.R., et al. 2007. Dynamic Simulations with an Improved Model for Foam Generation. *SPE J.* **12**(1): 35-48.

Kam, S.I., 2008. Improved Mechanistic Foam Simulation with Foam Catastrophe Theory. *Colloids Surf. A* **318**(1-3): 62-77.

Kharabaf, H., and Yortsos, Y. 1997. Invasion Percolation with Memory. *Phys. Rev. E.* **55**(6): 7,177-7,191.

Kharabaf, H., and Yortsos, Y.C. 1998. Pore Network Model for Foam Formation and Propagation in Porous Media. *SPE J.* **3**(1): 42-53.

Khatib, Z.I., Hirasaki, G.J., and Falls, A.H. 1988. Effects of Capillary Pressure on Coalescence and Phase Mobilities in Foams Flowing Through Porous Media. *SPE Reservoir Eng.* **3**(3): 919-926.

Kil, R.A., Nguyen, Q.P., and Rossen, W.R. 2011. Determining Trapped Gas in Foam from CT Images. *SPE J.* **16**: 24-34.

Kornev, K.G., Neimark, A.V., and Rozhkov, A.N. 1999. Foam in Porous Media: Thermodynamic and Hydrodynamic Peculiarities. *Adv. in Colloid and Interface Sci.* **82**: 127-187.

Kovscek, A.R., Patzek, T.W., and Radke, C.J. 1993. Simulation of Foam Transport in Porous Media. Paper SPE 26402 presented at 68th Annual Technical Conference and Exhibition of the Society of Petroleum Engineers, Houston, TX, 3-6 October.

Kovscek, A.R., and Radke, C.J. 1994. Fundamentals of Foam Transport in Porous Media. In *Foams: Fundamentals and Applications in the Petroleum Industry*, ed. L.L. Schramm, Washington, DC: ACS Advances in Chemistry Series; American Chemical Society.

Kovscek, A.R., Patzek, T.W., and Radke, C.J. 1994a. Mechanistic Prediction of Foam Displacement in Multidimensions: A Population Balance Approach. SPE Paper 27789 presented at 9th SPE/DOE Symposium on Improved Oil Recovery, Tulsa, OK, 17-20 April.

Kovscek, A.R., Patzek, T.W., and Radke, C.J. 1994b. A Mechanistic Population Balance Model for Transient and Steady-State Foam Flow in Boise Sandstone. *Chemical Eng. Sci.* **50**(23): 3,783-3,799.

Kovscek, A.R., Patzek, T.W., and Radke, C.J. 1995. A Mechanistic Population Balance Model for Transient and Steady-State Foam Flow in Boise Sandstone. *Chem. Eng. Sci.* **50**(23): 3783-3799.

Kovscek, A.R., and Radke, C.J. 1996. Gas Bubble Snap-off under Pressure Driven Flow in Constricted Noncircular Capillaries. *Colloids and Surfaces A: Physicochem Eng. Aspect* **117**(1-2): 55-76.

Kovscek, A.R., Patzek, T.W., and Radke, C.J. 1997. Mechanistic Foam Flow Simulation in Heterogeneous and Multidimensional Porous Media. *SPE J.* **2**: 511-526.

Kovscek, A.R., and Bertin, H.J. 2003. Foam Mobility in Heterogeneous Porous Media. I: Scaling Concepts. *Transport in Porous Media* **52**: 17-35.

Kuhlman, M.I. 1990. Visualizing the Effect of Light Oil on CO_2 Foam. *SPE Journal of Petroleum Technology* **42**(7): 902-908.

Lee, H.O., and Heller, J.P. 1990. Laboratory Measurements of CO_2-Foam Mobility. *SPE Reservoir Engineering* **5**(2): 193-197.

Lee, H.O., Heller, J.P., and Hoefer, A.M.W. 1991. Change in Apparent Viscosity of CO_2 Foam with Rock Permeability. *SPE Reservoir Engineering* **6**(4): 421-428.

Li, R.F., Yan, W., Liu, S., et al. 2008. Foam Mobility Control for Surfactant EOR. Paper SPE 113910 presented at SPE/DOE Improved Oil Recovery Symposium, Tulsa, OK, 19-23 April.

Liang, Z., Ioannidis, A., and Chatzis, I. 2000. Permeability and Electrical Conductivity of Porous Media from 3D Replicas of the Microstructure. *Chem. Eng. Sci.* **55**: 5,247-5,262.

Lindquist, W.B., Venkatarangan, A., Dunsmuir, J., et al. 2000. Pore and Throat Size Distributions Measured from Synchrotron X-ray Tomographic Images of Fontainebleau Sandstones. *J. Geophys. Res.* **105**(B9): 21,509–21,528.

Marsden, S.S., and Khan, S.A. 1966. The Flow of Foam through Short Porous Media and Apparent Viscosity Measurements. *SPE J.* **6**(1): 17-25.

Martinsen, H.A., and Vassenden, F. 1999. Foam Assisted Water Alternating Gas (FAWAG) Process on Snorre. Presented at the European Symposium on Improved Oil Recovery, Brighton, U.K., 18-20 August.

Mast, R.F. 1972. Microscopic Behavior of Foam in Porous Media. SPE Paper 3997 presented at the 47th Annual Fall Meeting of the Society of Petroleum Engineers, San Antonio, Texas, 8-11 October.

Maniowe, D.J., and Radke, C.J. 1990. A Pore-level Investigation of Foam/Oil Interactions in Porous Media. *SPE Reservoir Engineering* **5**(4): 495-502.

Nilsson, G. 1957. The Adsorption of Tritiated Sodium Dodecyl Sulfate at the Solution Surface Measured with a Windowless, High Humidity Gas, Flow Proportional Counter. *J. Phys. Chem.* **61**: 1135-1142.

Nguyen, Q.P., Currie, P.K., and Zitha, L.J. 2004. Motion of Foam Film in Diverging-Converging Channel. *J. Colloid and Interface Sci.* **271**(2): 473-484.

Nguyen, Q.P., Rossen, W.R., Zitha, P.L.J., et al. 2009. Determination of Gas Trapping with Foam Using X-Ray CT and Effluent Analysis. *SPE J.* **14**: 222-236.

Osterloh, W.T., and Jante, M.J. 1992. Effects of Gas and Liquid Velocity on Steady State Foam Flow at High Temperature. SPE Paper 24179 presented at the SPE/DOE Eight Symposium on Enhanced Oil Recovery, Tulsa, OK, 22-24 April.

Owete, O.S., and Brigham, W.E. 1987. Flow Behavior of Foam: A Porous Micromodel Study. *SPE Reservoir Engineering* **2**(3): 315-323.

Park, H.C. 1972. The Flow of Non-Newtonian Fluids Through Porous Media. Ph.D. Thesis, Michigan State University, East Lansing, MI.

Pascal, H. 1981. Non-Steady Flow through Porous Media in the Presence of a Threshold Gradient. *Acta Mech.* **39**(3-4): 207-224.

Patzek, T.W. 1996. Field Applications of Steam Foam for Mobility Improvement and Profile Control. *SPE Res. Eng*. **11**(2): 79-86.

Persoff, P., Pruess, K., Benson, S.M., et al. 1990. Aqueous Foams for Control of Gas Migration and Water Coning in Aquifer Gas Storage. *Energy Sources* **12**: 479-497.

Princen, H.M. 1983. Rheology of Foams and Highly Concentrated Emulsions: I. Elastic Properties and Yield Stress of a Cylindrical Model System. *J. Colloid Interface Sci.* **91**(1): 160-175.

Prud'homme, R.K. 1981. Paper E-7. Presented at Annual Meeting of the Society of Rheology, Louisville, 11-15 October.

Radke, C.J., and Gillis, J.V. 1990. A Dual Tracer Technique for Determining Trapped Gas Saturation during Steady Foam Flow in Porous Media. Paper SPE 20519 presented at the SPE Annual Technical Conference and Exhibition, New Orleans, LA, 23-26 September.

Ransohoff, T.C., Gauglitz, P. and Radke, C.J. 1987. Snap-off of Gas Bubbles in Smoothly Constricted Noncircular Capillaries. *AlChe J.* **33**(5): 753-765.

Ransohoff, T.C., and Radke, C.J. 1988. Mechanisms of Foam Generation in Glass-Bead Packs. *SPE Reservoir Engineering* **3**(2): 573-585.

Ren, G., Zhang, H., and Nguyen, Q.P. 2011. Effect of Surfactant Partitioning between CO_2 and Water on CO_2 Mobility Control in Hydrocarbon Reservoirs. Paper SPE 145102 presented at SPE Enhanced Oil Recovery Conference, Kuala Lumpur, Malaysia, 19-21 July.

Ren, G., 2012. Dynamics of Supercritical CO_2 Foam in Porous Media with CO_2 Soluble Surfactants. PhD. Dissertation, The University of Texas at Austin.

Roof, J.G. 1970. Snap-off of Oil Droplets in Water-Wet Pores. *SPE J.* **10**(1): 85-90.

Rossen, W.R. 1990a. Minimum Pressure Gradient for Foam Flow in Porous Media: Effect of Interactions with Stationary Lamellae. *J. Colloid Interface Sci.* **139**: 457-468.

Rossen, W.R. 1990b. Theory of Mobilization Pressure Gradient of Flowing Foams in Porous Media. I. Incompressible Foam. *J. Colloid Interface Sci.* **136**: 1-16.

Rossen, W.R. 1990c. Theory of Mobilization Pressure Gradient of Flowing Foams in Porous Media. II. Effect of Compressibility. *J. Colloid Interface Sci.* **136**: 17-37.

Rossen, W.R. 1990d. Theory of Mobilization Pressure Gradient of Flowing Foams in Porous Media. III. Asymmetric Lamella Shapes *J. Colloid Interface Sci.* **136**: 38-53.

Rossen, W.R., and Gauglitz, P.A. 1990. Percolation Theory of Creation and Mobilization of Foams in Porous Media. *AIChE J.* **36**: 1,176-1,188.

Rossen, W.R. 1992. Rheology of Foam in Porous Media at the 'Limiting Capillary Pressure'. *Rev. Inst. Fr. Pet.* **47**: 68-80.

Rossen, W.R., and Mamun, C.K. 1993. Minimal Path for Transport in Networks. *Phys. Rev. B.* **47**: 11,815-11,825.

Rossen, W.R., and Zhou, Z.H. 1995. Modeling Foam Mobility at the Limiting Capillary Pressure. *SPE Adv. Technol.* **3**: 146-152.

Rossen, W.R. 1996. Foams in Enhanced Oil Recovery. In *Foams: Theory, Measurement, and Applications*, ed. R.K. Prud'homme and S. Khan, New York: Surfactant Science Series, Marcel Dekker.

Rossen, W.R., and Wang, M.W. 1999. Modeling Foams for Acid Diversion. *SPE J.* **4**, 92-100.

Rossen, W.R. 2003. A Critical Review of Roof Snap-Off as a Mechanism of Steady-State Foam Generation in Homogeneous Porous Media. *Colloids Surf., A:Physicochem. Eng. Aspects* **225**(1-3): 1-24.

Sanchez, J.M., and Hazlett, R.D. 1992. Foam Flow through an Oil-Wet Porous Medium: A Laboratory Study. *SPE Reservoir Engineering* **7**(1): 91-97.

Shah, C.B., Kharabaf, H., Yortsos, Y.C. 1995. In Flow and Displacement of Bingham Plastics in Porous Media. Presented at the UNITAR Conference On Heavy Oils and Tar Sands, Houston, TX, 16 February.

Skelland, A.H.P. 1967. Non-Newtonian Flow and Heat Transfer. Wiley: New York.

Sochi, T., and Blunt, M. 2008. Pore-scale Network Modeling of Ellis and Herschel-Bulkley Fluids. *J. Pet. Sci. Eng.* **60**(2), 105-124.

Sahimi, M. 1993. Flow Phenomena in Rocks: From Continuum Models to Fractals, Percolation, Cellular Automata, and Simulated Annealing. *Rev. Mod. Phys.* **65**: 1,393-1,534.

Schramm, L.L., Turta, A.T. and Novosad, J.J. 1993. Microvisual and Coreflood Studies of Foam Interactions with a Light Crude Oil. *SPE Reservoir Engineering* **8**(3): 201-206.

Schramm, L.L. 1994. Foams: Basic Principles. In *Foams: Fundamentals and Applications in the Petroleum Industry*, ed. L.L. Schramm, Washington, DC: ACS Advances in Chemistry Series, American Chemical Society.

Schramm, L.L. and Green, W.H.F. 1995. The Influence of Marangoni Surface Elasticity on the Stability of Foams in Porous Media. *Colloids & Surfaces* **94**: 13-28.

Simjoo, M., Dong, Y., Andrianov, A., et al. 2012. A CT Scan Study of Immiscible Foam Flow in Porous Media for EOR. Paper SPE 155633 presented at SPE Enhanced Oil Recovery Conference, Muscat, Oman, 16-18 April.

Srivastava, M., and Nguyen, Q.P. 2010. Application of Gas for Mobility Control in Chemical EOR in Problematic Carbonate Reservoirs. Paper SPE 129840 presented at the SPE Improved Oil Recovery Symposium, Tulsa, OK, 24-28 April.

Srivastava, M., Zhang, J., Nguyen, Q.P., et al. 2010. Systematic Study of Alkaline-Surfactant-Gas Injection for EOR. *J. Pet. Technol.* **62**:1.

Tang, G.Q., and Kovscek, A.R. 2006. Trapped Gas Fraction During Steady-State Foam Flow. *Transp. Porous Media* **65**: 287-307.

Tanzil D., Hirasaki, G.J. and Miller, C.A. 2002. Mobility of Foam in Heterogeneous Media: Flow Parallel and Perpendicular to Stratification. *SPE J.* **7**(2): 203-212.

Teeuw, D., and Hesselink, F.T. 1980. Power-law Flow and Hydrodynamic Behavior of Biopolymer Solutions in Porous media. Presented at the Fifth International Symposium on Oilfield and Geothermal Chemistry, Stanford, CA, 28-30 May.

Thompson, K.E., Willson, C.S., White, C. D., et al. 2008. Application of a New Grain-Based Reconstruction Algorithm to Microtomography Images for Quantitative Characterization and Flow Modeling. *SPE J.* **13**(2): 164-176.

Turta, A.T., and Singhal, A.K. 1998. Field Foam Applications in Enhanced Oil Recovery Projects: Screening and Design Aspects. Paper SPE 48895 presented at the SPE International Conference and Exhibition, Beijing, China, 2-6 November.

Vassenden, F., and Holt, T. 2000. Experimental Foundation for Relative Permeability Modeling of Foam. *SPE Reservoir Eval. Eng.* **3**: 179-185.

Verwey, E.J.W., and Overbeek, J.T.G. 1948. *Theory of the Stability of Lyophobic Colloids*. Amsterdam: Elsevier Science Publishers.

Vradis, G., and Protopapas, A. 1993. Macroscopic Conductivities for Flow of Bingham Plastics in Porous Media. *J. Hydraulic Eng.* **119**(1), 95-108.

Xu, Q., and Rossen, W.R. 2000. Dynamic Viscosity of Foam in Porous Media. Paper presented at 3rd Euroconference on Foams, Emulsions, and Applications, Delft, the Netherlands, 5-8 June.

Xu, Q., and Rossen, W.R. 2003. Effective Viscosity of Foam in Periodically Constricted Tubes. *Colloids Surf., A:Physicochem. Eng. Aspects* **216**(1-3): 175-194.

Zhou, Z.H., and Rossen, W.R. 1994. Applying Fractional-Flow Theory to Foams for Diversion in Matrix Acidization. *SPE Prod. Facil.* **9**: 29-35.

Zhou, Z.H., and Rossen, W.R. 1995. Applying Fractional-Flow Theory to Foam Processes at the Limiting Capillary Pressure. *SPE Adv. Tech. Series* **3**(1): 154-162.

Vita

Huseyin Onur Balan holds BS and MS degrees in Petroleum and Natural Gas Engineering, and a minor degree in Remote Sensing and Geographical Information Systems from Middle East Technical University (METU) in Ankara, Turkey. Upon completion of his MS education, he enrolled in PhD program in Petroleum and Geosystems Engineering at the University of Texas at Austin.

Email: onurbalan@gmail.com

This dissertation was typed by Huseyin Onur Balan.